Naval Research Laboratory

Washington, DC 20375-5000

NRL/FR/6383--92-9369

Experimental Determination of Dissipated Energy Density as a Measure of Strain-Induced Damage in Composites

PHILLIP W. MAST, GERALD E. NASH, JOHN MICHOPOULOS,
RAY W. THOMAS, ROBERT BADALIANCE, AND IRVIN WOLOCK

Mechanics of Materials Branch
Materials Science and Technology Division

April 17, 1992

REPORT DOCUMENTATION PAGE

Form Approved
OMB No. 0704-0188

1. AGENCY USE ONLY (Leave blank)	2. REPORT DATE	3. REPORT TYPE AND DATES COVERED
	April 17, 1992	

4. TITLE AND SUBTITLE

Experimental Determination of Dissipated Energy Density as a Measure of Strain-Induced Damage in Composites

5. FUNDING NUMBERS

PE - 62234N
TA - RS34-S91-0S0
WU - 63-1005-02 DN

6. AUTHOR(S)

P.W. Mast, G.E. Nash, J.G. Michopoulos,
R.W. Thomas, R. Badaliance, and I. Wolock

7. PERFORMING ORGANIZATION NAME(S) AND ADDRESS(ES)

Naval Research Laboratory
Washington, DC 20375-5000

8. PERFORMING ORGANIZATION REPORT NUMBER

NRL/FR/6383--92-9369

9. SPONSORING/MONITORING AGENCY NAME(S) AND ADDRESS(ES)

David Taylor Research and Development Center
Bethesda, MD 20034

10. SPONSORING/MONITORING AGENCY REPORT NUMBER

11. SUPPLEMENTARY NOTES

12a. DISTRIBUTION/AVAILABILITY STATEMENT

Approved for public release; distribution unlimited.

12b. DISTRIBUTION CODE

13. ABSTRACT *(Maximum 200 words)*

An approach to characterizing failure behavior and degree of load induced internal damage in composite materials and structures is formulated. This approach is based on a systematic experimental procedure to observe response of composite materials subjected to multiaxial load environment. The energy dissipated by internal failure mechanisms is employed as a measure of internal damage and is characterized by an energy dissipation function, which is identified by means of a deconvolution procedure data provided by NRL's automated in-plane loader. Use of this information as a failure analysis and prediction tool is demonstrated by simulating the structural response of some naval structural components made from several different composite materials.

In addition, a general theory for the derivation of the constitutive behavior of the damaged composites is presented.

14. SUBJECT TERMS

Composites Dissipated energy
Failure Multiaxial loading

15. NUMBER OF PAGES

77

16. PRICE CODE

17. SECURITY CLASSIFICATION OF REPORT	18. SECURITY CLASSIFICATION OF THIS PAGE	19. SECURITY CLASSIFICATION OF ABSTRACT	20. LIMITATION OF ABSTRACT
UNCLASSIFIED	UNCLASSIFIED	UNCLASSIFIED	UL

NSN 7540-01-280-5500

Standard Form 298 (Rev. 2-89)
Prescribed by ANSI Std. Z39-18
298-102

CONTENTS

EXPERIMENTAL DETERMINATION OF DISSIPATED ENERGY DENSITY AS A MEASURE OF STRAIN-INDUCED DAMAGE IN COMPOSITES

Executive Summary

The use of composite materials in structural components has increased dramatically in recent years as their cost of production continues to decline and advances in composite design methodology become increasingly wide spread. As applications become more demanding, the need for reliable prediction of their mechanical properties and behavior is becoming ever more important.

The basic obstacle to a comprehensive understanding of failure behavior in composites is the complexity of their observed mechanical behavior. Composites are generally anisotropic, markedly nonlinear, and, unlike metals, usually fail in an extremely complicated, spatially diffuse, noncatastrophic manner. The nonlinear mechanical behavior of composites is known to be associated with damage accumulation that causes a local decrease in stiffness of the material in areas where damage is pronounced. Moreover, the complicated manufacturing process results in many imperfections that take on a variety of forms including fiber imperfections, fiber misalignment, and geometrical irregularities in the distribution of fibers, voids or microcracks in the matrix material, and the presence of debonded areas. These defects, combined with high-stress fields near material or geometric discontinuities, induce matrix cracking, fiber breakage, fiber-matrix debonding, and delamination, all of which influence the overall mechanical properties of these materials.

Extensive efforts to identify the various modes of damage in composite materials have been undertaken in recent years. The primary finding of most of these investigations was that macroscopic fracture was usually preceded by an accumulation of the different types of microscopic damage and occurred by the coalescence of this small-scale damage into macroscopic cracks. Additionally, it was generally found that analyses based on classical fracture mechanics did not adequately model the damage effects and did not provide a satisfactory degree of predictive capability.

A more practical approach to modeling failure behavior in composites is to quantify the damage development on a continuum basis and relate it to the material constitutive behavior. The goal of such an approach is to permit accurate modeling of the progressive loss of stiffness and concomitant inelastic behavior caused by the underlying micromechanisms of damage. Such a model for composite failure behavior requires a large parameter space for its description if it is to represent physical fact in a high-fidelity, objective manner. The model must be generic and phenomenological in nature and must rely on extensive sets of experimental data to identify the model parameters. Only after these parameters are determined can the model be related to particular failure mechanisms.

The purpose of this report is to describe the initial stages of an approach to modeling the mechanical behavior of composite materials consistent with the aforementioned standards. This approach, which in the spirit of the prior discussion is largely based on systematic experimentation, provides a methodology for quantifying the failure behavior of a broad class of composite materials and for characterizing the degree of internal damage the material undergoes when it is part of a structural component subjected to general loadings. This approach also provides a factual base against which any other continuum damage approach can be measured.

The procedure involves the determination of an *energy density dissipation function* which has the dimensions of energy per unit volume and is postulated to be a property of the material. Its volume integral

equals the energy dissipated during loading because of the various internal failure events, and its value at any point in the material is regarded as a measure of load-induced internal damage. The energy dissipation function thus captures the collective behavior of these failure mechanisms without requiring an explicit knowledge of these mechanisms, and, moreover, can also be related to local stiffness changes that, as will be demonstrated subsequently, lead to a form of nonlinear structural behavior. Section 5 presents a detailed description of the material model. In our approach, the energy density dissipation function is determined from data obtained by means of an extensive series of tests performed with NRL's In-Plane Loader, which is a computer-controlled testing machine capable of producing multiple combinations of opening/closing, sliding, and rotating boundary displacements. A brief explanation of the methodology for determining (identifying) the dissipation function follows.

A representation of the energy dissipation function as a function of strain is chosen in terms of a set of known basis functions and a set of undetermined coefficients. The task is then to estimate these coefficients. To accomplish this, a number of test specimens are first subjected to a range of prescribed combinations of in-plane loads using the In-Plane Loader. These loads induce a wide range of internal strain states in the specimens. These states approximately encompass those expected in typical structural components under service loading conditions. The boundary displacements and boundary loads are measured for each load combination, and are used to compute the energy dissipated internally in the specimens caused by strain-induced damage for each test. The strain fields associated with each of the load combinations are also determined by means of a linear finite element analysis using the constitutive properties of the undamaged (virgin) material. The computation, therefore, neglects the effects of stiffness changes induced by the internal damage, but should be sufficiently accurate provided that no large-scale stress redistribution occurs during the tests. Analytic estimates of the dissipated energy are then computed in terms of the unknown coefficients for each test using the representation of the dissipation function, the computed strain fields , and the fact that the volume integral of the dissipation function equals the dissipated energy. Finally, the undetermined coefficients in the dissipation function representation are determined by minimizing the difference between the experimentally measured and the analytic estimates of the dissipated energy for all the tests. Sections 2 and 3 detail this procedure.

The aforementioned procedure is a *deconvolution* procedure in the sense that the goal is to extract a material property (the dissipated energy density function) from information obtained from the material in a particular physical configuration, namely the specimen, and, thus, it is necessary to factor out specimen geometry effects. By taking this approach, the resulting dissipated energy density function can be applied to any structural configuration, and used to develop material softening (stiffness reduction) maps for any structure (again, assuming a negligible amount of stress redistribution caused by internal damage). Indeed, in Section 4, we demonstrate the applicability of the model by describing a computational approach packaged as a material response simulator and its use in simulating the structural response of several structures of interest. These are a ship's mast, the test specimen itself, and a cylindrical shell representing an idealized section of a submarine hull. A number of different composite material systems are considered and spatial maps of the dissipation function (softening maps) are produced for various loading magnitudes. These softening maps illustrate how the energy consumed by the various internal failure events is dissipated within the structure.

While the energy dissipation function can be approximately determined without explicit knowledge of the damage-induced constitutive nonlinearities as discussed above, a more refined approximation requires a representation of the full-scale nonlinear behavior. This information is also of much interest in its own right since it is needed for stress analysis when analyzing the behavior of structural components loaded well into the nonlinear response range where substantial load redistribution is expected. These issues are addressed in Section 5, where a representation of the constitutive behavior in terms of the energy dissipation function is developed along with a refined scheme for identifying the dissipation function itself.

In summary, an approach is formulated to characterize failure behavior and degree of load induced internal damage in composite materials and structures . This approach is based on a systematic experimental procedure to observe response of composite materials subjected to multiaxial load environment. The energy dissipated by internal failure mechanisms is used as a measure of internal damage and is characterized by an *energy dissipation function*, which is determined by means of a deconvolution procedure using data provided by NRL's automated In-Plane Loader. Use of this information as a failure analysis and prediction tool is demonstrated by simulating the structural response of some naval structural components made from several different composite materials. In addition, a general theory for the derivation of the constitutive behavior of the damaged composites is presented.

EXPERIMENTAL DETERMINATION OF DISSIPATED ENERGY DENSITY AS A MEASURE OF STRAIN-INDUCED DAMAGE IN COMPOSITES

1. INTRODUCTION

The use of composite materials in structural components has increased dramatically in recent years as their cost of production continues to decline and advances in composite design methodology become increasingly wide spread. As applications become more demanding, the need for reliable prediction of their mechanical properties and behavior is becoming ever more important.

The basic obstacle to a comprehensive understanding of failure behavior in composites is the sheer complexity of their observed mechanical behavior. Composites are generally anisotropic, markedly nonlinear, and, unlike metals, usually fail in an extremely complicated spatially diffuse noncatastrophic manner (Badaliance and Hill (1982); Morris and Hetter (1982); Masters and Reifsnider (1982)).The nonlinear mechanical behavior of composites is known to be associated with damage accumulation which causes a local decrease in stiffness of the material in areas where damage is pronounced. In many fibrous composite systems damage, develops at applied loads much lower than the design limit (Highsmith and Reifsnider (1982)). In materials that have a laminated structure, the complicated manufacturing process results in many imperfections that take on a variety of forms including fiber imperfections, fiber misalignment and geometrical irregularities in the distribution of fibers, voids or microcracks in the matrix material, and the presence of debonded areas. These defects, combined with high-stress fields near material or geometric discontinuities, induce matrix cracking, fiber breakage, fiber-matrix debonding, and delamination, all of which influence the overall mechanical properties of these materials. Extensive effort to identify the various modes of damage in composite materials has been undertaken in recent years (i.e,. Aveston and Kelly (1973); Tsai and Hahn (1974); Reifsnider and Stinchcomb (1978); Reifsnider (1980); Highsmith and Reifsnider (1982); Dvorak and Johnson (1980) among others). The primary outcome of these investigations was that macroscopic fracture was usually preceded by an accumulation of the different types of microscopic damage and occurred by the coalescence of this small-scale damage into macroscopic cracks. Moreover, it was generally found impossible to model the effects of the damage using analyses based on classical fracture mechanics approaches.

A more practical approach to modeling failure behavior in composites is to quantify the damage development on a continuum basis and relate it to the material constitutive behavior. The goal of such an approach is to permit accurate modeling of the progressive loss of stiffness and concomitant inelastic behavior due to the underlying micromechanisms of damage. Such modeling would represent an extremely important achievement from an engineering standpoint. For example, consider a laminated composite plate with a center hole made from a commercially available composite (i.e., AS1/3501-6 graphite/epoxy) that is loaded in quasi-static tension. Damage patterns will develop around the hole and near the corners of the plate (Morris and Hetter (1982)) inducing degradation in material properties and forming a precursor to general failure. An examination of the micrographs readily indicates that a detailed micromechanical analysis is out of the

Manuscript approved Dec. 18, 1991.

question because the characteristic scale length of damage is of the order of μm leading to the conclusion that a continuum-based damage model would be far more appropriate under these circumstances.

The analysis of highly localized singular fields by means of continuum approaches has a long history and there exist a number of well-established techniques developed specifically for this purpose. Most of these approaches involve smearing out singular fields in some fashion and replacing them by locally homogeneous fields, an example being continuous dislocation theory (i.e. Bilby, Bullough and Smith (1955); Kratochvil and Dillon (1969), among others). More generally, there have recently been a plethora of continuum damage approaches based on the idea of an internal damage variable first introduced by L.M. Kachanov (1958) (e.g., Allen, Harris and Groves (1987), Bazant (1986), L.M. Kachanov (1986), Krajcinovic (1984,1986), Lemaitre (1987), Onat and Leckie (1988), Talreja (1987)). A common shortcoming of most of these theories is that they are usually not based on observed facts, but rather tend to use models defined over low dimensional parameter spaces that reflect preconceived notions of the dominant failure mechanisms. Virtually no previous studies address this problem; indeed, this is one of the primary purposes of this report.

An appropriate model for composite failure behavior requires a large parameter space for its description if it is to represent physical fact in a high-fidelity, objective manner. Because the phenomena being considered are generally so complex, it seems futile to formulate models in terms of the individual failure events; rather, the chosen model must be generic and phenomenological in nature and must rely on extensive sets of experimental data to identify the model parameters. Only after these parameters are determined can the model be related to particular failure mechanisms.

This report describes the initial stages of an approach to modeling the mechanical behavior of composite materials consistent with the aforementioned standards. This approach, which, in the spirit of the prior discussion is largely based on systematic experimentation, provides a methodology for quantifying the failure behavior of a broad class of composite materials and for characterizing the degree of internal damage the material undergoes when it is part of a structural component subjected to general loadings. This approach also provides a factual base against which any other continuum damage approach can be measured.

The procedure involves the determination of an *energy density dissipation function* that has the dimensions of energy per unit volume and is postulated to be a property of the material. Its volume integral equals the energy dissipated during loading because of various internal failure events, and its value at any point in the material is regarded as a measure of load-induced internal damage. The energy dissipation function thus captures the collective behavior of these failure mechanisms without requiring an explicit knowledge of these mechanisms, and, moreover, can also be related to local stiffness changes which, as will be demonstrated subsequently, lead to a form of nonlinear structural behavior. In the sense that this material model relates load-induced internal damage to nonlinear structural behavior, it is similar to the models recently used by Schapery (1987, 89a, 89b, 90). The present approach is not limited to composites, but has application in the general area of the mechanics of irreversible processes where there is an acute need for a reliable and accurate procedure to experimentally determine equivalent dissipated energy density functions. This issue is more fully addressed in several works that deal with the thermomechanical modelling of irreversible processes associated with material behavior in general under mechanical loading (Michopoulos *et al.* (1984); Sih (1987); and Sih *et al.* (1987)). Section 5 presents a detailed description of the material model and its implementation.

The energy density dissipation function is determined from data obtained by means of an extensive series of tests performed with NRL's In-Plane Loader (IPL) (Mast *et al.* (1983, 84)). This is a completely computer-controlled testing machine capable of producing multiple combinations of opening/closing, sliding, and rotating boundary displacements. Figure 1 schematically describes the methodology for determining (identifying) the dissipation function.

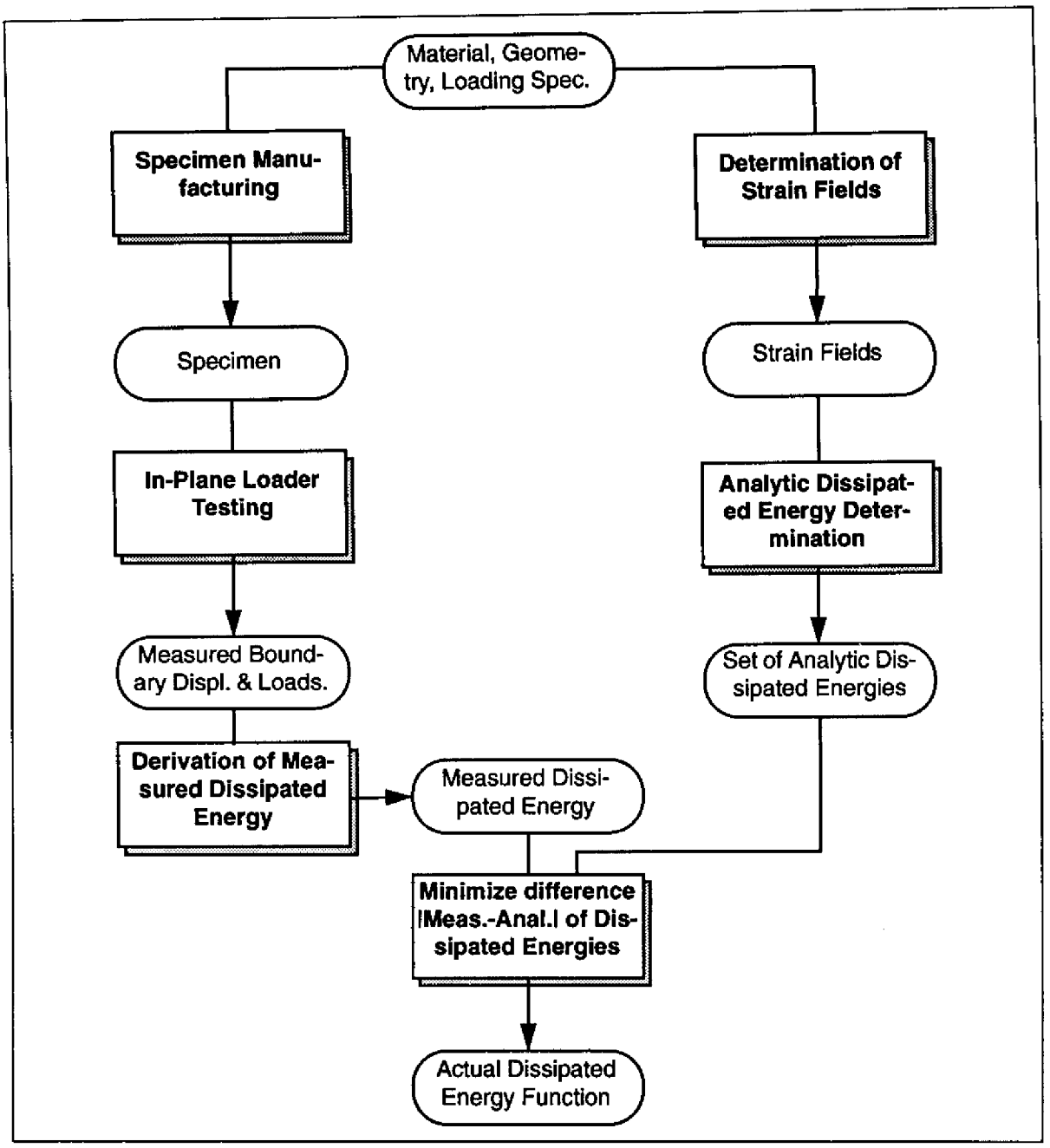

Fig. 1 — Block diagram of processes involved in determining the Dissipated Energy function

The left subpath in Fig. 1 describes the experimental part of the identification process and basically involves determining the energy dissipated in the specimens during the IPL tests. The initial step consists of using the material and geometry specifications to manufacture the test specimens. Next, the loading specifications are applied by using the IPL to load the specimens in the manner prescribed. Finally, the measured boundary displacements and loads are used to compute the total energy dissipated internally in the specimens due to strain-induced damage. Section 2 presents details of this portion of the identification process.

The remaining subpaths in Fig. 1 represent the numerical and analytical part of the process. Initially, as shown in the right subpath, the strain fields associated with each of the loading conditions prescribed in the loading specification are determined for the given material and specimen geometry. This is achieved by finite element analyses. A class of functions with free coefficients is then defined such that one member of this class can represent an analytic representation of the dissipated energy as a function of the strain fields. Finally, as indicated at the bottom of Fig. 1, the particular function that is best suited for representing the dissipation energy is computed by determining the values of the free coefficients that minimize the difference between the experimentally measured and the analytic representation of the dissipated energy. Section 3 details this part of the process.

The aforementioned procedure is a *deconvolution* procedure in the sense that the goal is to extract a material property (i.e., the dissipated energy density function) from information obtained from the material in a particular physical configuration, (i.e., the specimen), and, thus, it is necessessary to factor out specimen geometry effects. By taking this approach, the resulting dissipated energy density function can be applied to any material configuration and used to develop material softening maps for any structure. In Section 4, we demonstrate the applicability of the model by describing a computational approach packaged in a material response simulator and its use in simulating the structural response of a ship's mast. A number of different composite material systems are considered and spatial maps of the dissipation function are produced for various loading magnitudes. These maps illustrate how the energy consumed by the various internal failure events is dissipated within the structure as a function of load and material.

The specimen used for the experimental measurement of the dissipated energy can also be regarded as a structure where the same process can be applied. We perform such an analysis in Section 4. Although this does not seem to be directly associated with naval structures, we chose to emphasize the fact that the technique of simulating the response of a structure does not depend on a particular shape or loading, but rather on the material response used for its construction. At the same time, this structure has additional significance because of the essential role it plays in the whole process. Finally, Section 4 also presents simulations of the structural response of a cylindrical shell representing an idealized section of a submarine hull.

The procedures in our approach have been implemented in a highly automated fashion by a sequence of computational activities that use the analyses described in the following sections. Figure 2 shows a data flow diagram view of these processes and their relationships. The process of acquiring the IPL data and the computation of the measured total dissipated energy for the test specimen is described in Section 2, and is achieved through the processes "IPL15" and "GETABS," the latter of which evaluates the absorbed and dissipated energy in the specimen. Section 3 describes the computation of the dissipated energy density function. This is performed by

- using "PATRAN" to create the complete finite element model of the specimen,
- feeding the finite element data to the "ABAQUS" finite element code via the "PATABA" data translator,
- performing a linear elastic analysis to determine the strain field for each point in the specimen, and
- piping the measured dissipated energy of the specimen and the strain fields through the "ABAPAT" translators into "ABSPAT."
- "ABSPAT" then computes the dissipated energy density function by deconvolution and uses an optimization scheme to minimize the difference between the measured and the approximated values of the dissipated energy as described in Section 3.

Control of the interprocess and intercomputer communications is achieved through a user interface module.

The simulation of material stiffness loss over any particular structure as described in Section 4 is achieved by

- using "PATRAN" to specify the finite element idealization and loading specification of the structure,
- piping the data to "ABAQUS" via the "PATABA" data translator to compute the strain fields associated with the selected loading conditions, and
- piping the computed dissipated energy density function and the strain field via the "ABAPAT" translator into "ABSORB" to obtain the dissipated energy distributions over the structure which can then be displayed using "PATRAN."

Again, control of the interprocess and intercomputer communications is achieved through another user interface module.

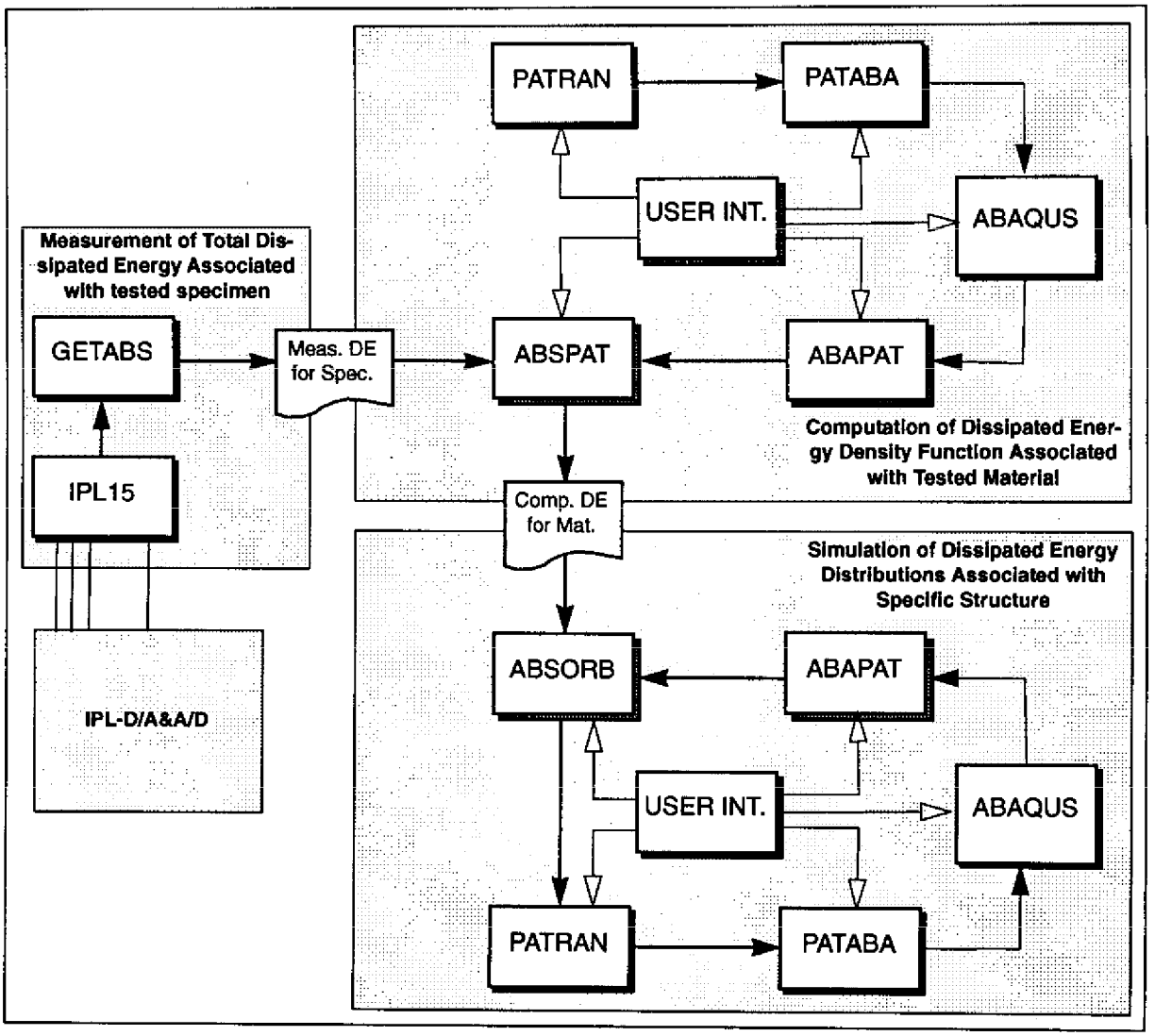

Fig. 2 — Computational implementation of the current approach in terms of the essential modules and their functional relationship

More detailed versions of the computational descriptions pertaining to all the aforementioned processes are presented in the corresponding sections (2, 3 and 4) of the report.

While the energy dissipation function can be approximately determined without explicit knowledge of the damage-induced constitutive nonlinearities as discussed above, a more refined approximation requires a representation of the full-scale nonlinear behavior. This information is also of much interest in its own right since it is needed for stress analysis when analyzing the behavior of structural components loaded well into the nonlinear response range where substantial load redistribution is expected. Section 5 addresses and develops a representation of the constitutive behavior in terms of the energy dissipation function along with a refined scheme for identifying the dissipation function itself.

2. DATA ACQUISITION THROUGH THE IN-PLANE LOADER SYSTEM

2.1 Material Specification

Composites associated with naval applications range through a wide variety of materials. Each different combination of matrix, fiber, fiber coating (for matrix-fiber interface), layup angle, stacking sequence, etc., corresponds to a different material. Our approach is specifically tailored to organic matrix composites. In general, the particular material specification for an application in a structure depends not only on the mechanical considerations but also on a host of additional considerations such as cost, electromagnetic and thermal properties. Approximately 100 material systems with graphite fibers ranging from AS1 to IM7 (Hercules Corp.) and several thermoset and thermoplastic organic polymers have been tested and characterized with the present approach. Here we limit our description to the materials selected for the applications discussed in this report. A brief description of these materials is given in Table I in terms of the matrix, the fiber, and the angle of layup. Appendix A is a complete list of all the materials tested up until now.

Most of the materials were received in the form of panels out of which the specimens were cut and machined to the specimen specification.

Table 1 — Fragment of the Materials Database Describing Four of the 101 Different Materials Used in the Present Study

ITEM	RESIN	FIBER	LAYUP	SUPPLIER	FILE	PROJECT
001	3501-6	AS1	+/- 15	Hercules	mt-1	NAV-SEA
002	.	.	+/- 30	.	mt-2	.
007	.	AS4	+/- 60	.	mt-7	.
040	PEEK	.	+/- 60	ICI	mt-40	.

2.2 Specimen Specification

The specimen geometry shown in Fig. 3 was designed to satisfy the following requirements:

- The characteristic dimensions be large enough relative to fiber diameter and lamina thickness to ensure that the material could be analyzed as either a single mechanically equivalent homogeneous anisotropic monolithic material, or a collection of layers of varying orientations of such materials.
- The overall specimen size be small enough to keep material costs at a manageable level.

- A strain riser be present to guarantee that high-strain regions occur well away from all specimen boundaries.

Figure 3 shows the single edge-notched specimen that resulted. It is important to note that the primary function of the notch is to act as a strain riser to ensure satisfaction of the last requirement above, and *not* to mimic a crack in the fracture mechanics sense.

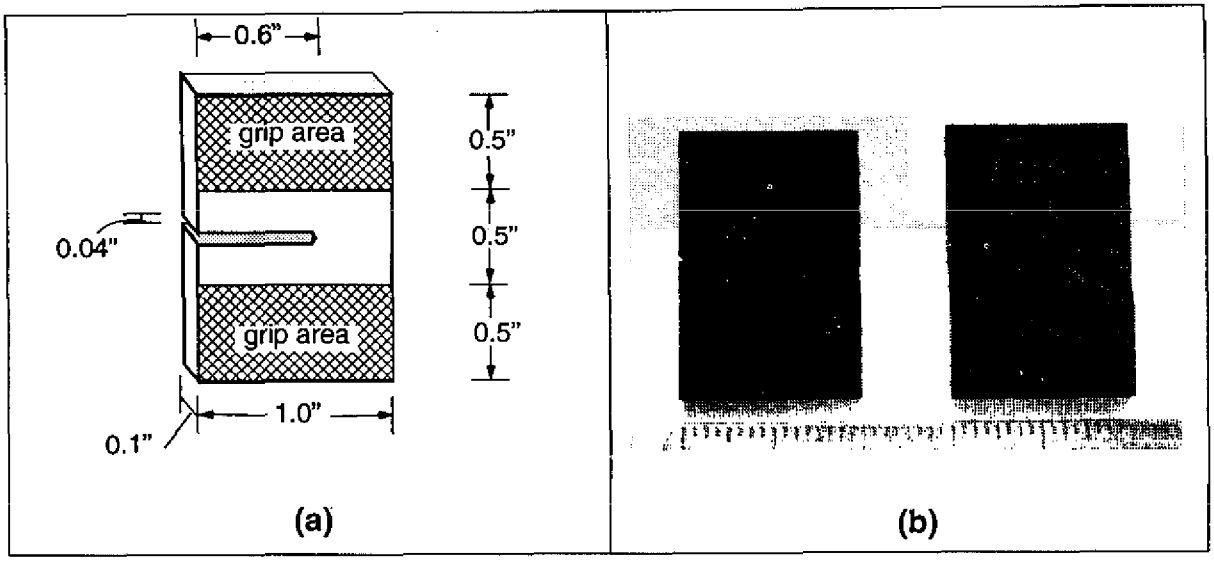

Fig. 3 — (a) Schematic of the specimen and the associated areas, (b) photos of representative specimen before testing (left) and after testing (right) for material 2 with 3501-6 resin AS1 fiber and +/- 30° layup and loading path 11

2.3 Loading Specification

The experimental system used for measuring the dissipated energy in the test specimens is the In-Plane Loader System (IPLS). Appendix B presents a detailed description of this testing system. The primary component of the IPLS is a custom-made, fully automated testing machine (the In-Plane Loader or IPL) shown in Fig. 4. The remaining components of the IPLS are a computer that fully controls the IPL and a graphics processor that is used for various postprocessing operations in conjunction with the computer system.

The objective of the IPLS is to control the rigid body motion of the boundary of the specimen that is held by the movable grip. Because the actuators are constrained to move in a plane parallel to the specimen, the resulting motion involves only three degrees of freedom relative to any frame of reference on that plane.

The relation between the prescribed actuator displacements and the resulting grip motion is illustrated in Fig. B3(a) and B3(b) of Appendix B. It is important to note here is that the grip motion can be resolved into three basic components: sliding u_x, opening/closing u_y, and rotation ω. Specified combinations of actuator displacements, therefore, map into particular combinations of these three basic motions.

It is convenient to use a reference frame located at the initial position of the notch tip for both the boundary displacements (denoted by $\underset{\sim}{u}$ relative to this frame) and the resulting reaction forces $\underset{\sim}{t}$. Figure B3(c) of Appendix B illustrates these displacements and tractions and the resulting deformation of the specimen.

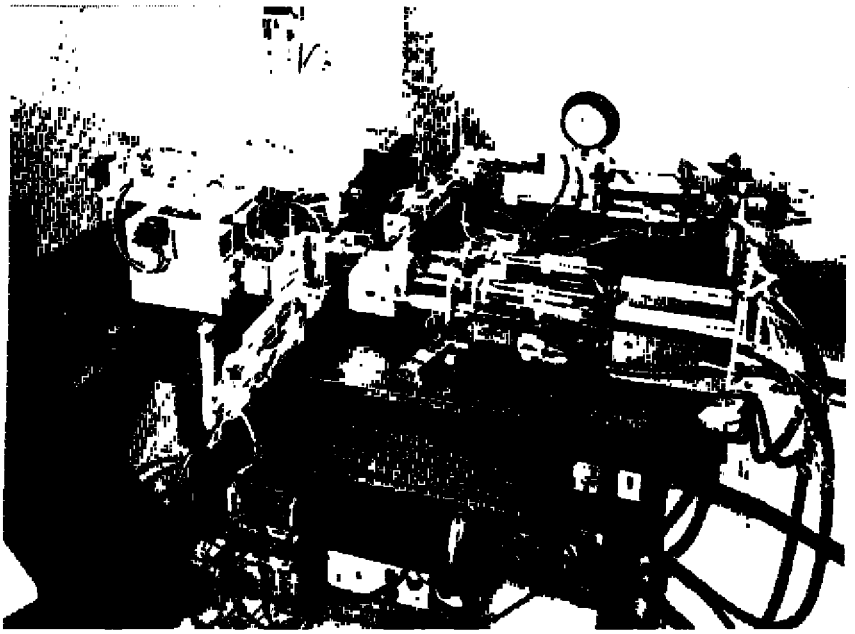

(a)

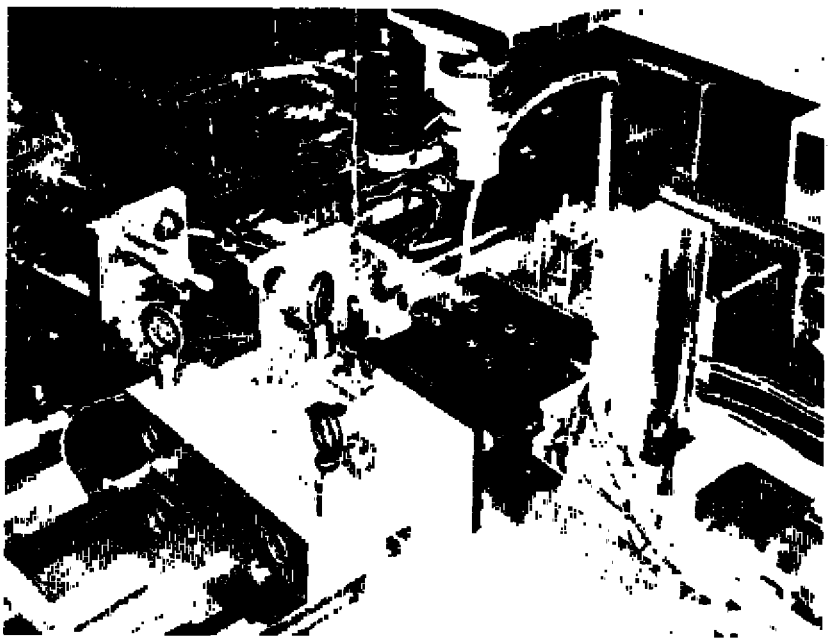

(b)

Fig. 4 — (a) Side view of the In-Plane Loader. (b) View of the grip area of the In-Plane Loader

The decomposition of the applied displacements relative to this frame into a sliding motion u_0, an opening/closing motion u_1, and a rotational motion u_2 is shown in Fig. B3 (d,e,f) of Appendix B and Fig. 5(b, c and d), respectively. For dimensional homogeneity, u_2 is defined as the length of the arc traveled by a point 1 inch away from the notch tip rigidly connected with the moving grip along the direction of the rotation, instead of using the actual rotation in radians.

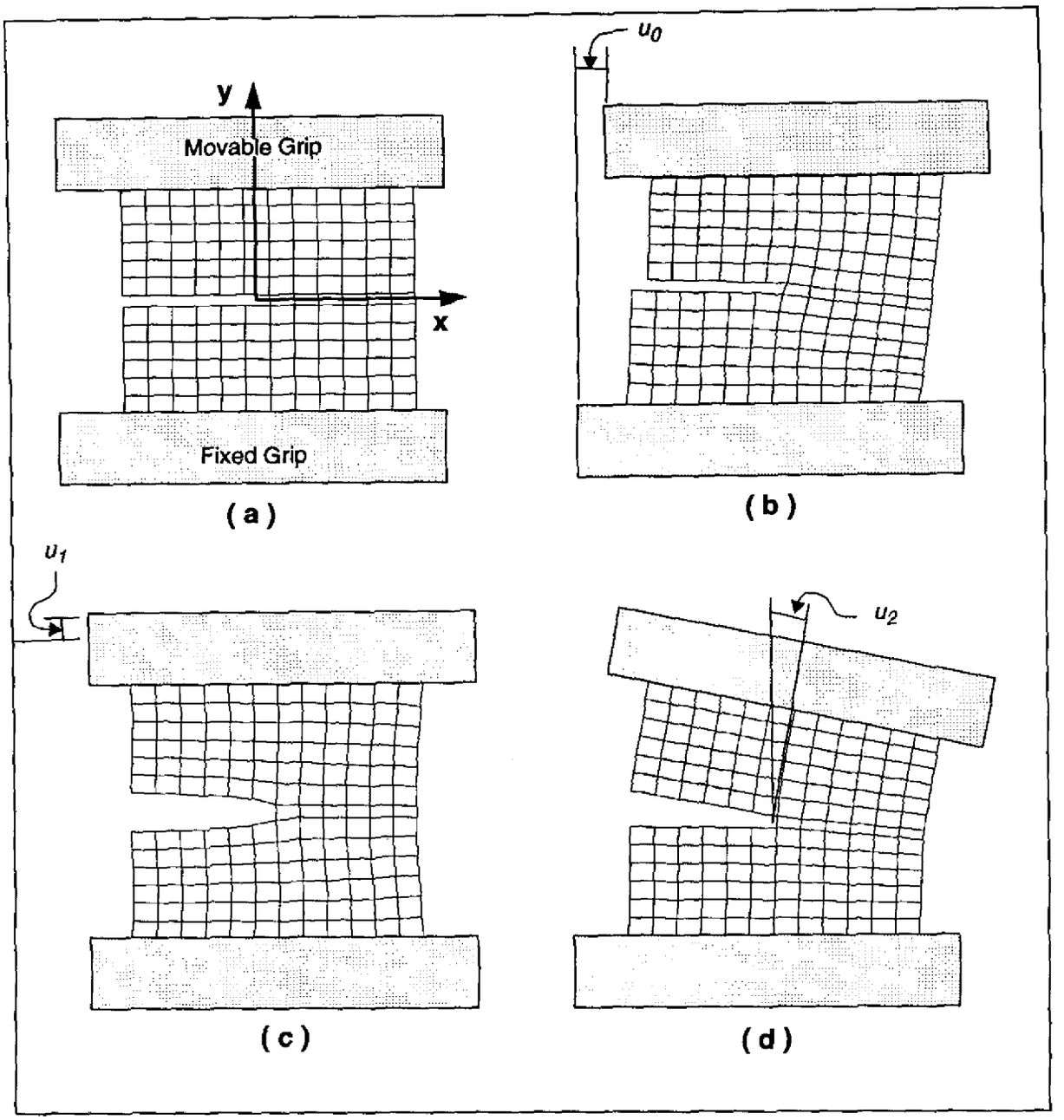

Fig. 5 — View area of the IPL specimen in the grips (a) before applying any loading, (b) after applying some translation of the upper grip parallel to the x- axis, (c) parallel to the y- axis, and (d) after applying rotation about the origin of the x-y frame of reference

Subsequent analysis requires that we compute the energy dissipated within the material at a discrete set of observation points as the specimen is loaded by applying a predetermined series of boundary displacements u^p. Here $p = 1,...,n$ and n denotes the number of observation points. The details of these computations will be discussed in the next section; here we attend to the sampling strategy. It is advantageous to think in terms of a three-dimensional displacement space with coordinates (u_0, u_1, u_2). The issue then is how to select a representative family of paths that cover the space and how to sample along each path.

It is not expected to observe any significant path-dependent behavior *during this initial loading phase*. By this we mean that we expect the mechanical response of the material at any point in this space to depend only on the current state of internal strain and to be independent of the particular path followed to achieve this state. This type of path independence is consistent with the observations of Schapery and Lamborn (1988) and greatly simplifies matters because it permits us to cover the displacement space with a family of loading paths selected solely on the basis of convenience.

Towards this end, it was decided to cover the boundary displacement space with a set of 15 uniformly distributed radial loading paths as indicated in Fig. 6. Note that because of geometry and material symmetry about the x axis (Fig. 5), only the half-space corresponding to positive sliding displacement (u_0>0) need be considered. The required set of observation points is generated by sampling along each path at 50 distinct points starting from 0 mils and terminating at a maximum of 50 mils of displacement yielding a total of 750 points per material system. Then a particular test in that the actuator motions are continuously varied corresponds to a specific path in this space. This path can be represented by a vector originating from the origin of the space and components given by $u_i = ra_i$ for $i = 0, 1, 2$, where a_i are the coordinates of the unit vectors along the loading path direction, and r is a scalar multiple denoting the proportionality of the path and ranging from 0 to 0.05 inches in steps of 0.001 inches corresponding to the successive observation points. Only 15 specimens are required, and 50 observations per loading path are obtained from a single specimen. Table 2 shows the coordinates a_i of the unit vectors for the selected loading paths.

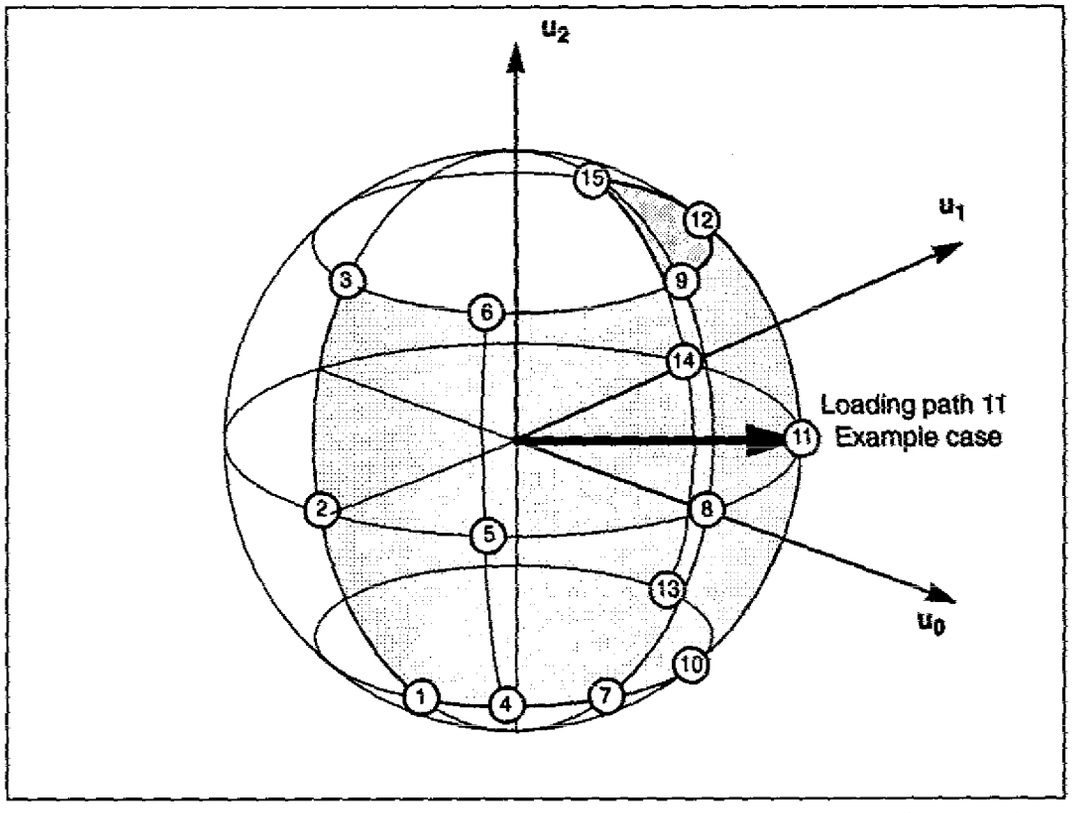

Fig. 6 — Definition of the proportional loading paths in the boundary displacement space (loading path 11 is a representative case), and the uniform distribution of the 15 paths used in the present methodology

Table 2 — Coordinates of Load Path Unit Vectors for each one of the 15 Loading Cases Applied by the IPL

LOADING	a_0	a_1	a_2
1	0.000	-0.707	-0.707
2	0.000	-1.000	0.000
3	0.000	-0.707	0.707
4	0.500	-0.500	-0.707
5	0.707	-0.707	0.000
6	0.500	-0.500	0.707
7	0.707	0.000	-0.707
8	1.000	0.000	0.000
9	0.707	0.000	0.707
10	0.500	0.500	-0.707
11	0.707	0.707	0.000
12	0.500	0.500	0.707
13	0.000	0.707	-0.707
14	0.000	1.000	0.000
15	0.000	0.707	0.707

The locus of the end points of all loading paths for the same increment is a half-sphere as shown in Fig. 6, where loading path 11 at an arbitrary increment is presented as an example.

2.4 Testing Procedure

The IPL is instructed to apply loads along the designated loading path for each specimen. Because each test is performed twice to establish the degree of reproducibility, 30 (2 per loading path) specimens are required for analyzing a single material. After the IPL calibration phase is complete, a stack of thirty specimens from the same material is loaded on the magazine of the automated specimen feeder of the IPL and the testing phase follows. The following sequence of events is repeated for each specimen.

- The specimen is fed from the specimen magazine into the grip area of the IPL.
- Pressure is applied on the hydraulic grips to clamp the specimen with the appropriate force to prevent slippage and crushing of the specimen.
- The operator uses the digital imaging system of the IPL to control the positioning of a crosshair on the image of the area between the grips as acquired by the overhead video camera. Notch tip location and selected points between the grips are thus automatically fed into the computer of the IPLS, to establish the frame of reference.
- The remainder of the test is performed automatically, with the computer control system measuring specimen thickness and controlling the grip pressure, selecting and applying incrementally the loading path. The system monitors and stores the boundary forces and displacements for each loading step,

and using this data the total energy dissipated in the specimen for each loading increment in the loading path is computed and stored along with the force displacement data.

2.5 Computational and Data Description

Figure 7 is a data flow diagram showing the computational process corresponding to the left subpath of Fig. 1. The data from the A/D and D/A converters are directed to module "IPL15" through the Input/Output driver module. "IPL15" controls the data acquisition and control process by controlling the following operations:

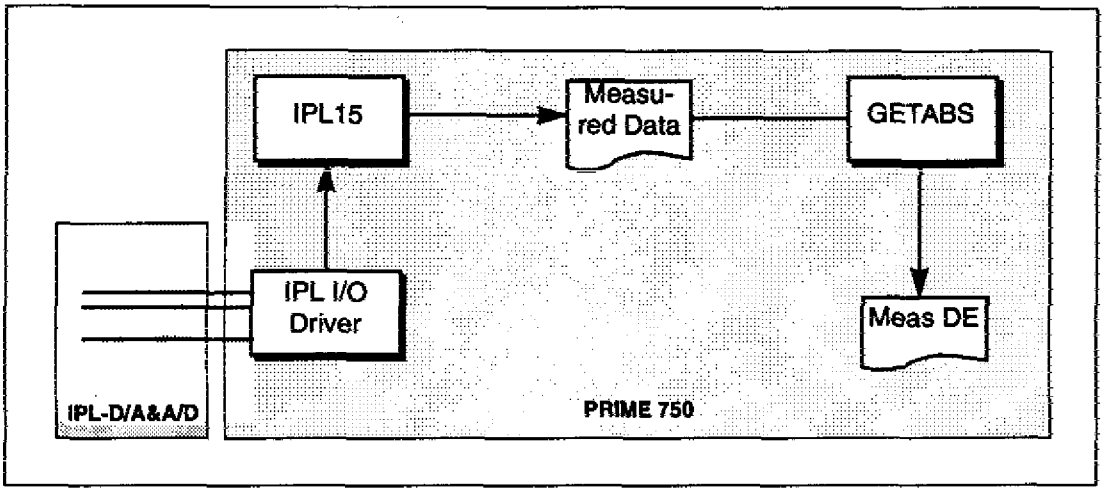

Fig. 7 — Block diagram of the computational modules and resources involved with the determination of the measured total dissipated energy

- it controls the positioning of the actuators and the associated hardware;
- it collects the force and displacements (t, u) at the 50 sampling points along the loading path from the transducers;
- it then transforms them into those referring to the frame of reference attached on the tip of the notch as in Fig. 5(a);
- it computes and displays the total and instantaneous values of the total dissipated energy lost in the specimen due to damage according to the methodology described in Section 2.6;
- it finally stores all measured quantities in files (one per material). Here the term "material" is used for a laminate of specific fiber, matrix, and lamination angle.

Each file contains the data for all specimens and loading paths for a given material. Each file consists of a header and a series of blocks that contain information pertaining to each specimen. The header is at the beginning of the file and contains the original filename. Each specimen block has its own header (which is seven records long) and fifty data records (one for each experimental point on the loading path). The header for each specimen contains all the pertinent information associated with the corresponding specimen and the respective loading path. Figure 8 presents a section of one of these files that corresponds to the second material of Table 1, i.e., graphite epoxy with AS1 fiber and 3501-6 resin with layup angle +/- 30 ^{0}. The fields in the data records, from left to right, are experimental point number, total dissipated energy D, boundary displacements $(u_0, u_1$, and $u_2)$, and boundary forces $(t_0, t_1$, and $t_2)$.

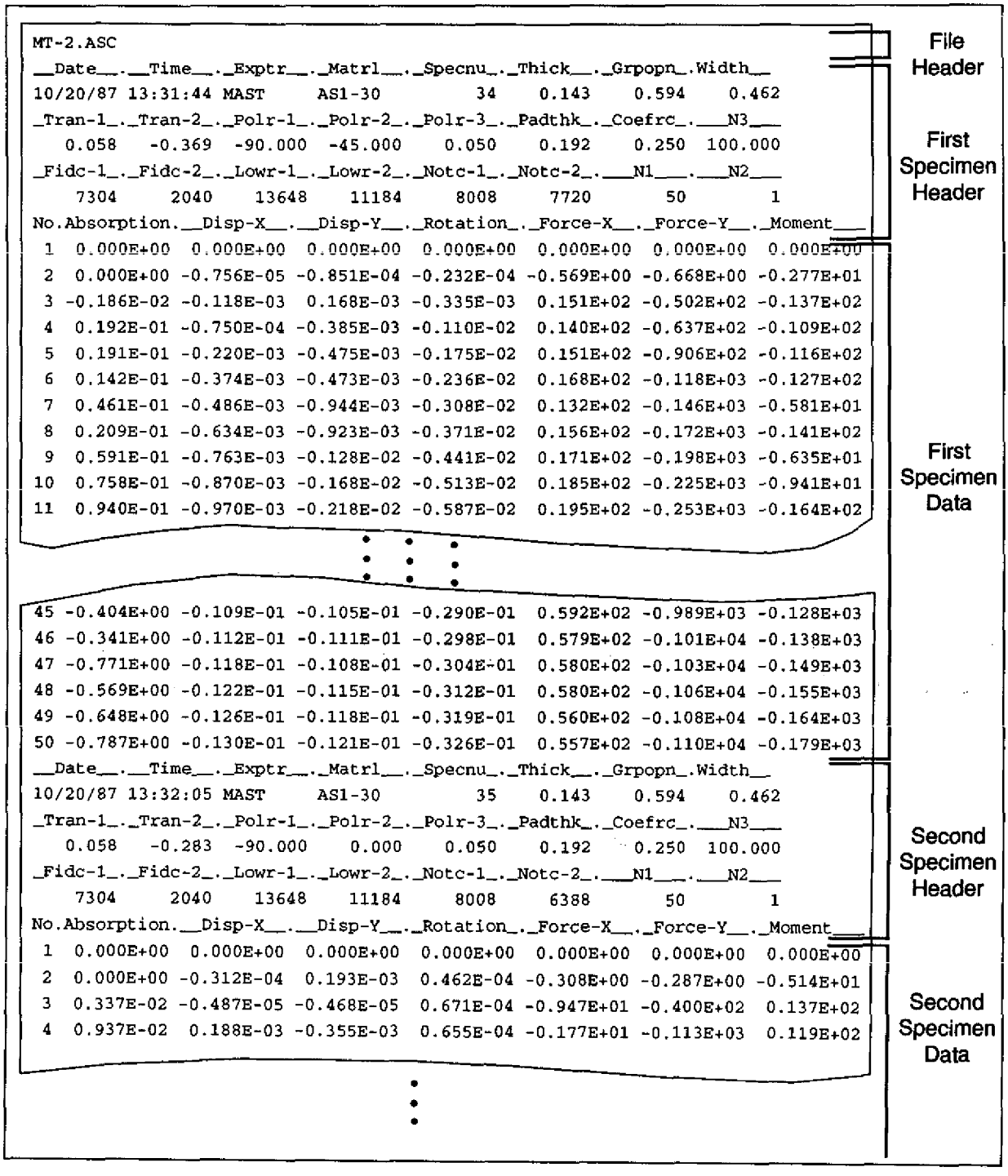

Fig. 8 — Typical parts of file containing the measured through the In-Plane Loader data

Another process called "GETABS" extracts the dissipated energy values from the aforementioned file and stores them into files ready to be used from the resources available for the determination of the dissipated energy density function as described in Section 4.

All these processes were originally executed on a PRIME 750 minicomputer, but recently an effort has been undertaken to recast them in a more contemporary form on the NeXT cube computing platform.

2.6 Computation of the Dissipated Energy

In this section we discuss in detail the procedure for computing the energy dissipated internally in the specimen during an IPL test. We employ the following convention in the rest of this report: superscript p ($p = 1,...,50$) denotes an experimental point on a given loading path; l ($l = 1,...,15$) denotes a particular loading path; $r = 1,2$ denotes a particular test repetition; and subscript i ($i = 0,1,2$) denotes the components of the boundary forces and displacements.

Consider first the total energy imparted to the specimen for each experimental point p as function of the boundary displacement vector $\underline{u}$. These energies, which we denote as W^p, can be computed from the measured boundary forces and displacements by using the standard definition of mechanical work. Thus

$$W^p = W^p(\underline{u}) = \int_0^{\underline{u}^p} \underline{t}^p \cdot d\underline{s}, \tag{1}$$

or in component form,

$$W^p = \int_0^{u_i^p} t_i^p ds_i = \int_0^{u_0^p} t_0^p \, ds_0 + \int_0^{u_1^p} t_1^p \, ds_1 + \int_0^{u_2^p} t_2^p \, ds_2. \tag{2}$$

Each term in Eq. (2) represents the energy stored in the specimen due to one of the measured force-displacement pairs (t_i^p, u_i^p) and is denoted by W_i^p. Hence, we may express W^p as the sum

$$W^p = W_0^p + W_1^p + W_2^p. \tag{3}$$

The integrals in Eq. (2) can be approximated using a discrete representation, i.e.,

$$W_0^p = \frac{1}{2} \sum_{a=1}^{p} (t_0^a + t_0^{a-1})(u_0^a - u_0^{a-1})$$

$$W_1^p = \frac{1}{2} \sum_{a=1}^{p} (t_1^a + t_1^{a-1})(u_1^a - u_1^{a-1}) \tag{4}$$

$$W_2^p = \frac{1}{2} \sum_{a=1}^{p} (t_2^a + t_2^{a-1})(u_2^a - u_2^{a-1}),$$

or in general

$$W_i^p = \frac{1}{2} \sum_{a=1}^{p} (t_i^a + t_i^{a-1}) (u_i^a - u_i^{a-1}), \qquad \text{for } i = 0, 1, 2. \tag{5}$$

This approximation process is graphically depicted in Fig. 9 where the quantities in the summation are defined geometrically on a representative traction vs displacement graph.

The area below the curve represents the energy W_i^p for loading up to point p as the sum of all trapezoids of area $\frac{1}{2} (t^a{}_i + t_i^{a-1}) (u_i^a - u_i^{a-1})$.

The total energy W^p can now be computed by substituting Eq. (5) into Eq. (3) and taking the sum of the three terms. Thus,

$$W^p = \frac{1}{2} \sum_{i=0}^{2} \sum_{a=1}^{p} (t^a{}_i + t_i^{a-1}) (u_i^a - u_i^{a-1}), \qquad \text{for } p = 1, 2, \ldots, 50. \tag{6}$$

Consider now the situation when the specimen unloads. We assume that when the specimen is unloaded proportionally from any point a of the curve in Fig. 9, the unloading occurs elastically along a line from the point a to the origin. This assumption is largely based on observations made during the early years of IPL use when unloading data were collected; it was found then that almost all specimens tested unloaded linearly and showed a maximum 2% permanent displacement set. These permanent displacements are likely a consequence of initial stresses introduced during manufacture and were deemed small enough to ignore. This characteristic non-metallike behavior during unloading has also been observed by other investigators (Shapery and Lamborn (1988)) and it is currently attributed to the propensity of organic composites to form microcracks instead of flowing plastically.

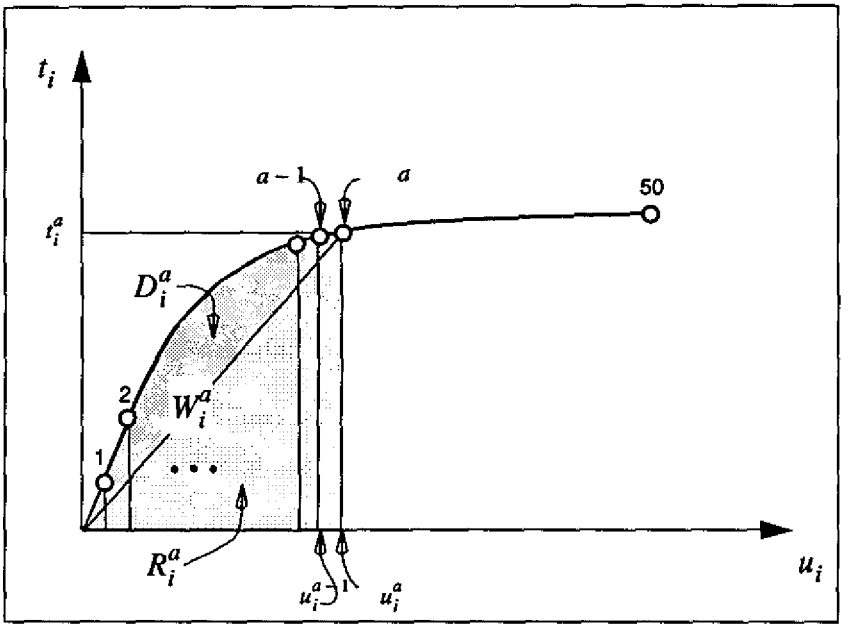

Fig. 9 — Schematic representation of the integration scheme used for the compute W_i^p as the sum of the rectangular slices under the load-displacement curve and of the energies associated with the loading of the specimen up to the point p

During unloading, a portion of the total energy W^p is recovered because of the elastic nature of the unloading response. This recoverable energy, denoted by a componentwise basis as R_i^p, is simply the triangular area under the line from a to the origin, or

$$R_i^p = \frac{1}{2} t_i^p u_i^p, \quad \text{for} \quad p = 1, 2, \ldots, 50. \tag{7}$$

Knowing the available energies W_i^p and the recoverable energies R_i^p, it is a simple matter to compute the energy D^p dissipated in the specimen. Thus, on a componentwise basis, the energy dissipated in the specimen as it is loaded up to point p is simply the difference

$$D_i^p = W_i^p - R_i^p, \quad \text{for} \quad p = 1, 2, \ldots, 50, \tag{8}$$

and, in graphical terms, is just the shaded area under the load-displacement line in Fig. 9. Substituting the expressions for the total and available energies from Eqs. (5) and (7) for each component i in the relation above, therefore, gives for D_i^p

$$D_i^p = \frac{1}{2} \sum_{a=1}^{p} (t^a{}_i + t_i^{a-1}) (u_i^a - u_i^{a-1}) - \frac{1}{2} t_i^p u_i^p, \quad \text{for} \quad p = 1, 2, \ldots, 50. \tag{9}$$

The total dissipated energy D^p (the energy which appears in the second column of the acquired data file shown in Fig. 8) can now be computed by summing D_i^p componentwise and results in

$$D^p = \frac{1}{2} \sum_{i=0}^{2} \sum_{a=1}^{p} (t^a{}_i + t_i^{a-1}) (u_i^a - u_i^{a-1}) - \sum_{i=0}^{2} \frac{1}{2} t_i^p u_i^p, \quad \text{for} \quad p = 1, 2, \ldots, 50. \tag{10}$$

The dissipated energy computed this way can be considered to be a measured value since it is derived directly from measured quantities and the only sources of error are from the discrete numerical integration described and the quantization error of the data acquisition process. However, the very operation of integration also serves as a noise/error reduction methodology and works more in a beneficial rather than a detrimental manner in this case. As far as we know, these energy values represent the only attempt to measure dissipated energy caused by mechanical deformation in composite materials.

Figure 10 is a graphical representation of the boundary displacements and tractions as well as the associated total and dissipated energies for the first specimen for loading path 11 for material AS1-30 (second row of Table 1). Loading path 11 does not have any rotation applied on the specimen as can be seen from Table 2 and from Fig. 6. This results in the apparent zeroing of the curve in Fig. 10(a.2), which consequently results in the blank energy graphs 10(c.2) and 10(d.2). However, due to the other two displacement components, there is a force reaction in the rotation direction as is shown in Fig. 10(b.2).

The dissipated energy curves start with values very close to zero and suddenly rise steeply. This happens as the corresponding displacements exhibit an abrupt increase and the tractions reach a maximum value and then rapidly decrease. This point can be interpreted as defining a transition between purely linear elastic material behavior (i.e., no energy dissipation) and the point at which the material first exhibits nonlinear behavior with accompanying energy dissipation.

Summation of the energies for the three components in Figs. 10(c.0), 10(c.1), and 10(c.2) yields Fig. 10(e) for the energy absorbed from all three component combinations in the specimen. Similarly, summation of the dissipated energy components in Figs. 10(d.0), 10(d.1), and 10(d.2) yields the total energy lost in the

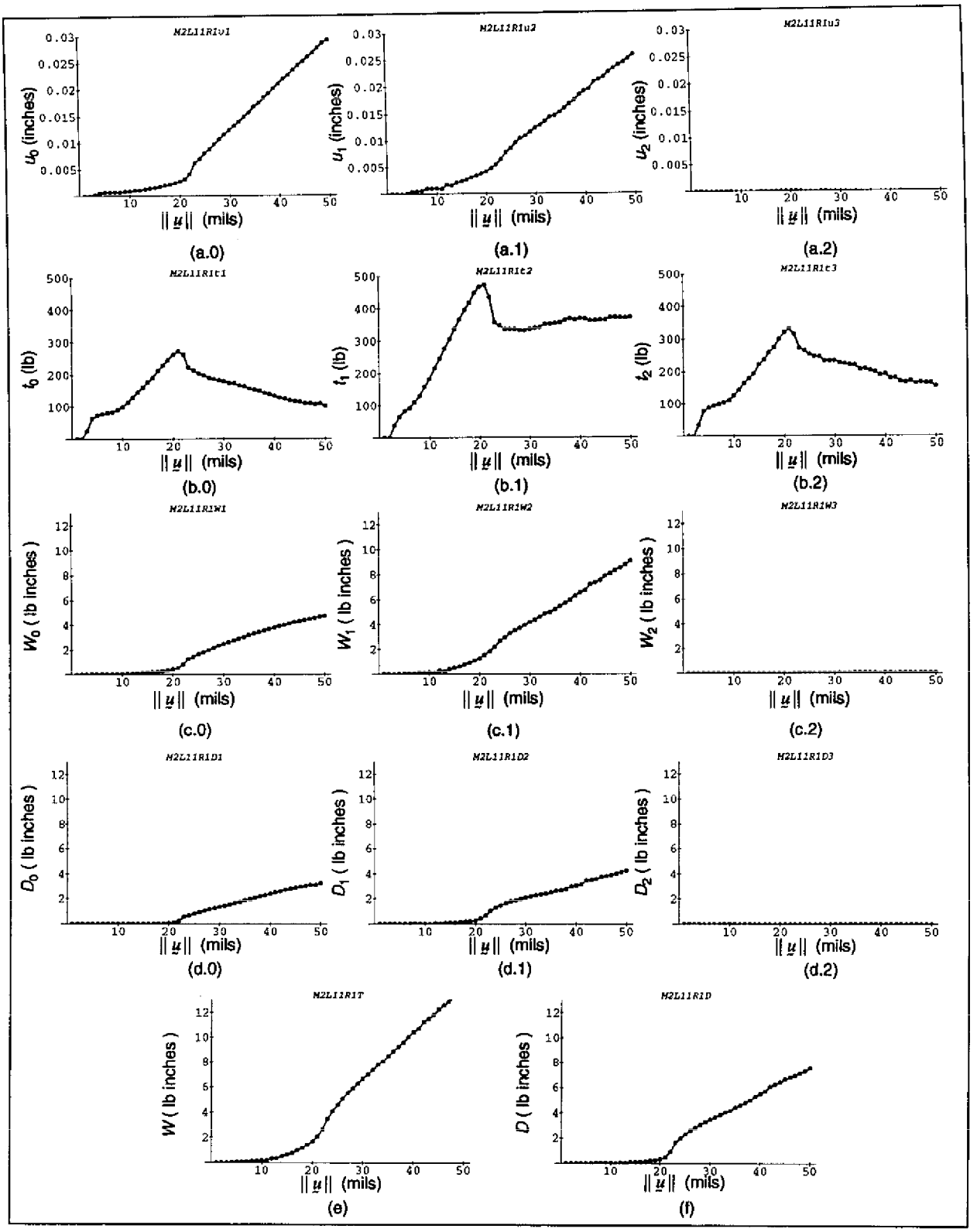

Fig. 10 — Evolution of displacements (a.0, a.1, a.2), tractions (b.0, b.1, b.2), total absorbed energies (c.0, c.1, c.2), dissipated energies (d.0, d.1, d.2), total absorbed energy (e), and total dissipated energy (f), vs the magnitude of the experimentally imposed displacement vector ||u|| of loading path 11 for the first specimen of material 2 (AS1, 3501-6, +/- 30 ^{o})

specimen shown in Fig. 10(f). The morphology of the displacement, traction, and energy evolution curves for the rest of the loading paths is not necessarily identical to that of loading path 11.

2.7 Statistics of the Process

To compare the repeatability of the process, Fig. 11 shows the dissipated energy evolutions for both specimens used on loading path 11 together with their average and absolute difference evolutions.

As it seen in Fig. 11(d) the specimens behave almost identically. A small difference of the order of 12% appears at the last experimental point, very deep in the nonlinear region where the enormous amount of damage has made the material more unstable than it is in the linear region. The root mean square error (RMS) between the two values of the dissipated energy for the two specimens from the same material has never been found to exceed 5% for all materials tested.

An entire IPL test takes about 10 seconds, five of which are spent installing the specimen in the grips. As a result, the specimen testing rate can be 360 specimens/hour. At this rate, data can be collected for 12 different materials per hour. The overall daily production rate for an 8-hour day is, therefore, 960 specimens, or 96 different materials, or 24 materials systems (since we use 4 layup angle combinations for each fiber-resin combination). The total number of experimental points per fiber-resin combination is 6000. Each loading path corresponds to 2.4 KB of data while 288 KB are acquired for each material system. The daily throughput capacity of the acquisition process approaches 20.74 MB/day.

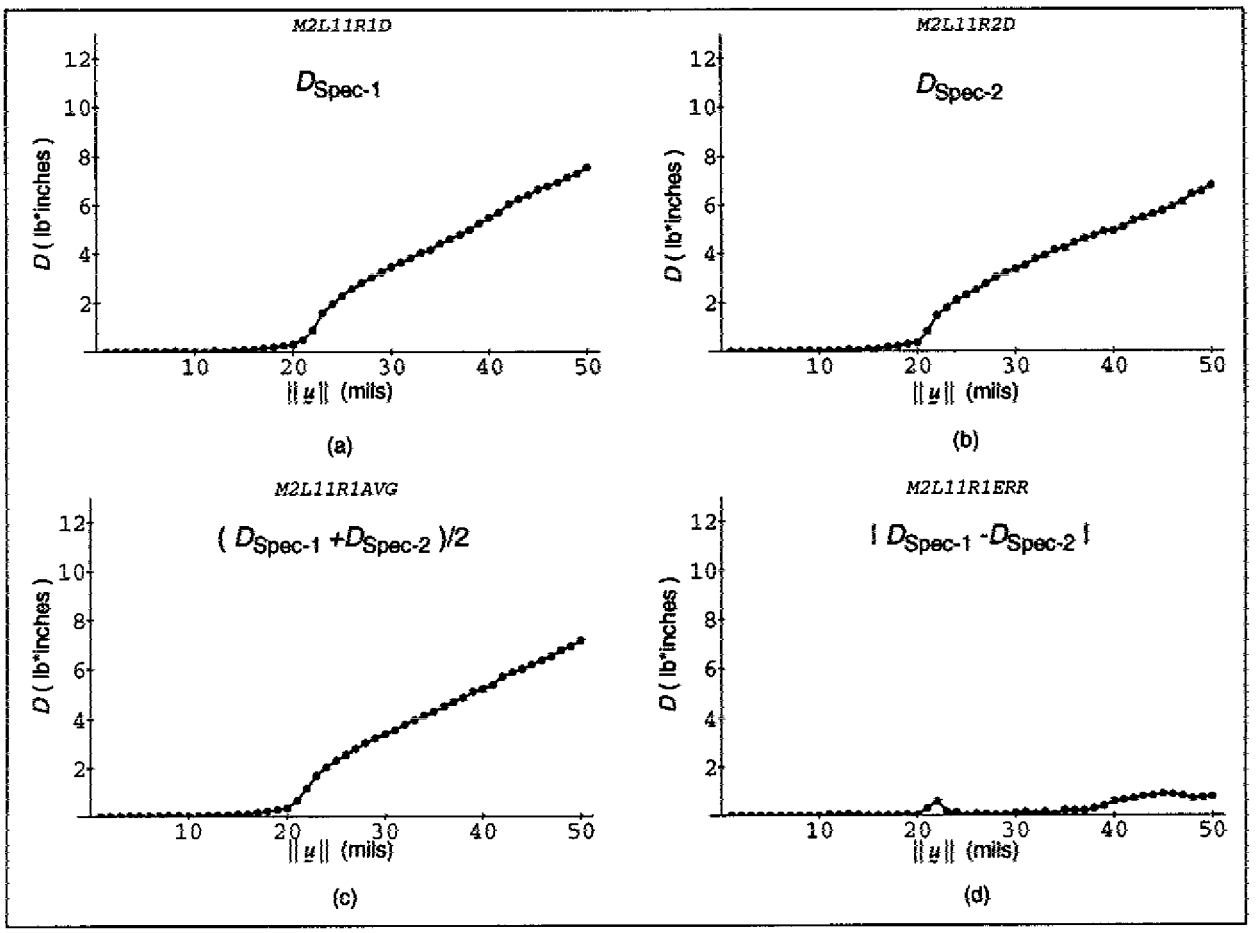

Fig. 11 — Dissipated energies for specimen 1 (a), specimen 2 (b), their average value (c), and the absolute difference between the two (d) for material 2 (AS1/6501-6 [+/- 30 °]) and loading path 11

3. DISSIPATED ENERGY DENSITY FUNCTION DETERMINATION

This section is primarily concerned with the right and the bottom subpaths of Fig. 1. These subpaths represent the flow of activities related to the determination of the dissipated energy density function ϕ . It is important, however, to clarify the range of hypotheses and assumptions employed in the present analysis to illustrate how our procedure relates to the so-called inverse approach in mechanics of materials research.

3.1 Computational Procedures

Figure 12 describes the computational process used to obtain the dissipated energy density function in terms of its evaluation on discrete points over the strain space.

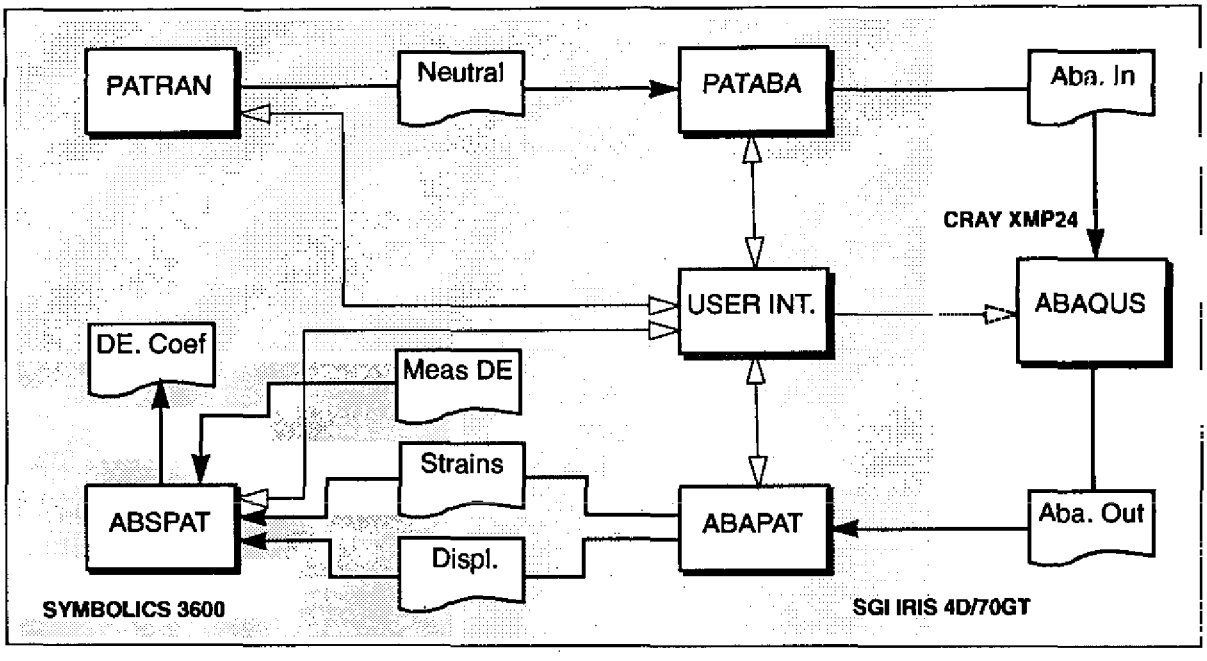

Fig. 12 — Block diagram of the modules used to compute the dissipated energy coefficients for each material, along with the computational resources utilization

A user interface that controls all interprocess and intercomputer communication is the mechanism by which the user controls the overall process. The "PATRAN" solid modeling package is used to define the geometry, material, and loading specifications for the finite element model of the specimen structure, which in turn is fed into the "ABAQUS" finite element code via the "PATABA" format translator. The output from the linear strain analysis from "ABAQUS" is then translated from "ABAPAT" into files containing the strain and displacement distributions for the corresponding loading cases that are displayable by "PATRAN." The "ABSPAT" module developed at NRL then

- uses the analysis results for all the loading cases as well as the experimentally measured values of the dissipated energy from the files discussed in Section 2.5 to synthesize the quantities necessary for estimating the 125 coefficients that describe the dissipated energy function,
- carry out the estimation, and
- generate one file per material system that contains the 125 coefficients.

3.2 Strain Field Determination

The measured absorbed energy is a function of specimen geometry, loading condition, and material. To factor out the influence of specimen geometry and loading and obtain a dissipated energy function that depends solely on material, it is necessary to develop a deconvolution procedure. A description of our approach to achieving this goal follows.

For every structure of a certain geometry s, consisting of a particular material m, and under a specific loading condition l, a strain state exists at any point described by the position vector $\underset{\sim}{x}$. The strain vector corresponding to this state with the classical in-plane components ($\underset{\sim}{\varepsilon} = (\varepsilon_{xx}, \varepsilon_{yy}, \varepsilon_{xy})$) is expected to be a function of s, m, l, and $\underset{\sim}{x}$; that is,

$$\underset{\sim}{\varepsilon} = \underset{\sim}{\varepsilon}(s, l, m, \underset{\sim}{x}) . \tag{11}$$

When the structure under consideration is a specific one, such as the specimen shown in Fig. 2, a subscript 0 for both the corresponding geometry and material is used to refer to this structure (s_0) and material (m_0) thereafter. It will become evident from the analysis that the strain field for each one of the loading cases needs to be determined. In the ideal case, these fields should be experimentally measured along with boundary tractions and displacements in the IPL tests. This will be a feature of the new generation of NRL's automated loading machines, however, the current generation has no such capabilities. The results and analysis presented here are based on an alternative approach. The approach used in this study to estimate the strain field was to discretize the geometry of the specimen into 150 elements as shown in Fig. 13, systematically apply the loading and boundary conditions applied by the IPL on the specimen, and compute the in-plane strains by running an appropriate number of linear elastic finite element analyses using the code "ABAQUS." The selection of the linear analysis was based on the fact that in very few of the experiments

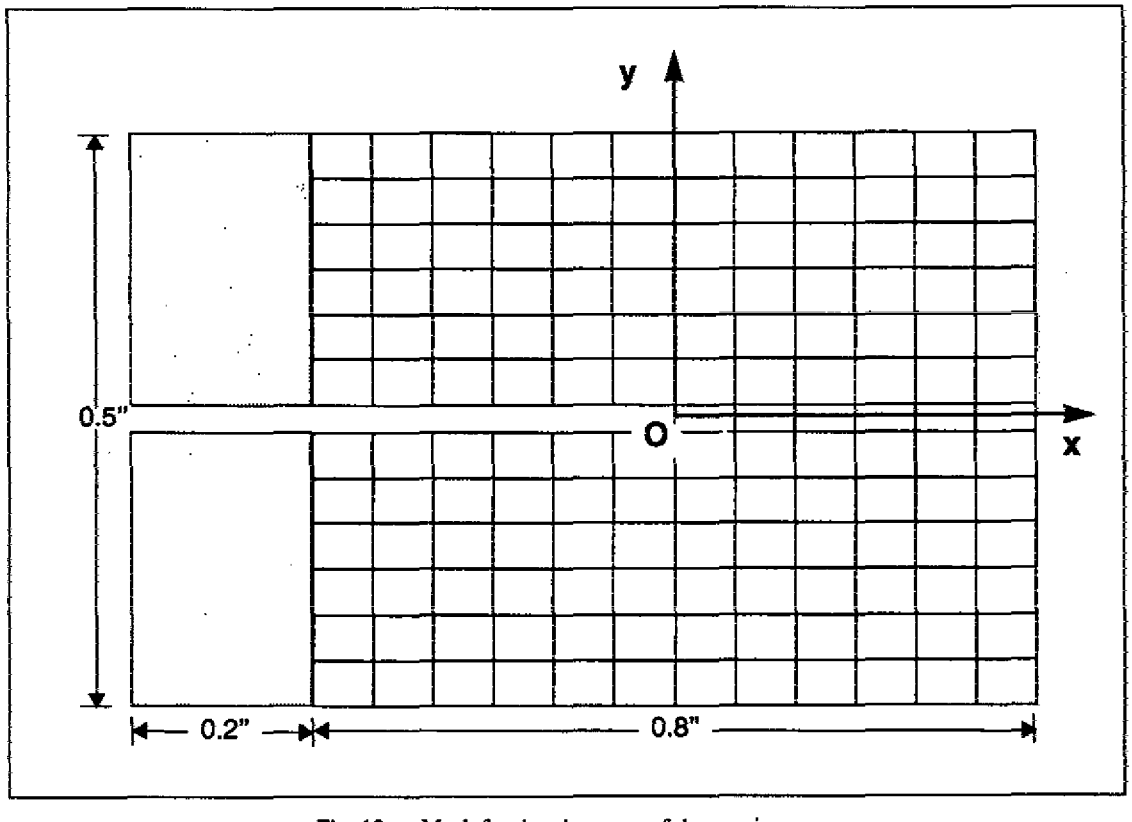

Fig. 13 — Mesh for the view area of the specimen

were specimens observed to fail in a way that would indicate that very large amounts of energy had been dissipated by internal material damage. In addition, our initial purpose was to establish an analytical tool based on experimental evidence for predicting the onset of nonlinear response and an approximation of this response, rather than the exact nonlinear material behavior. The three strain components corresponding to the centroids of the elements of the specimen structure s_0 were stored in files organized according to loading case. For practical purposes, instead of running 15 loading cases (one for each loading path), only the cases corresponding to the loading paths (1, 0, 0), (0, 1, 0), and (0, 0, 1) corresponding to pure shear, opening, and rotation displacements, respectively, were run. This was because all other cases could be synthesized by linear superposition according to Table 2.

Figure 13 shows the finite element mesh idealization of the specimen. Although initially the entire area between the grips had be discretized, subsequent analysis indicated that the area close to the left side of the specimen (the side of the notch) remains unstressed for virtually all loading cases. Thus, only the view area (as shown in Fig. 2) was actually analyzed.

3.3 Dissipated Energy Density Function

We assume that there exists a scalar function ϕ expressing a measure of the dissipated energy density per unit of volume of the material, which only depends on the strain vector $\underset{\sim}{\varepsilon}$ and the material used in the structure, i.e., $\phi(\underset{\sim}{\varepsilon}, m)$.

We furthermore assume that this function can be one of an arbitrarily large set of functions. For computational efficiency, we assume that the effect of the material and strain dependence can be decomposed by an appropriate choice of form for this function. This can be done by selecting a form expressed in terms of a set of coefficients that depend solely on the material properties, and a set of constant basis functions. For simplicity, the following linear combination case is selected:

$$\phi(\underset{\sim}{\varepsilon}, m) = \phi(\underset{\sim}{\varepsilon}, \underset{\sim}{c}) = c_1(m)\chi_1(\underset{\sim}{\varepsilon}) + \ldots + c_m(m)\chi_n(\underset{\sim}{\varepsilon}) = c_i(m)\chi_i(\underset{\sim}{\varepsilon}). \quad (12)$$

In this form, $\underset{\sim}{c}$ represents the vector of the material depended coefficients c_i, and χ_i represents the basis functions depending only on strains $\underset{\sim}{\varepsilon}$ and defined at a total of n distinct points distributed over the strain space. Equation (12) can be thought as being an interpolation function allowing evaluation of ϕ on points other than the ones used to define the basis functions.

In our case, 125 (i.e., 5 per axis) such points were selected to be uniformly distributed in the cartesian representation of the components of the strain space. Figure 14 shows the cuboidal distribution of the points where the basis function for our case is defined.

To have a unique number characterizing each one of the points where the strains are evaluated, three indices o,p, and q have been chosen along the ε_{xx}, ε_{yy}, ε_{xy} axes, respectively, to count from 1 to 5 as the (opq) frame of reference indicates in Fig. 14. This resulted in using a counter i for the points associated with these indices in the following relationship:

$$i = o + 5(p-1) + 25(q-1) \quad \text{for } , o, p, q = 1, \ldots, 5. \quad (13)$$

The increments along the three orthogonal strain component directions in this space are equidistanced and the step is the quotient of the maximum value for any of the strains obtained from the finite element analysis of the structure under consideration divided by 4 (number of spaces between the discrete points of evaluation).

The basis functions have the property of being equal to the value of the function at the evaluation point (in this case, 1), and zero at any other evaluation point of their domain. A consequence of this is that the value of the function ϕ according to Eq. (12) at an evaluation point is equal to the coefficient of the basis function for that point. This, it turns out, is a very convenient feature for the solution scheme described later in this section.

Figure 14 gives a graphic definition of how a basis function behaves. The five successive planes have been shifted out of the strain space and have been drawn such that the vertical axis represents the value of the function χ. The function has been evaluated at the point defined by ($o = 4, p = 3, q = 3$), or ($i = 64$), and as can be seen, the value of the function is zero at all nodal points of the strain space except for the point where it evaluates to 1. There it remains the same regardless of the evaluation point.

By letting $\underset{\sim}{\varepsilon}_i$ signify the strain vector for each point i for all 125 labeled points in the strain space, the basis functions with these properties can be expressed as:

$$\chi_i(\underset{\sim}{\varepsilon}_j) = \begin{cases} 1, & i = j \\ 0, & i = j \end{cases} \quad \text{for } i, j = 1, 2, \ldots, 125. \tag{14}$$

Introducing this relation to Eq. (12), for one of these points i we obtain

$$\phi(\underset{\sim}{\varepsilon}_i, m) = c_1(m)\chi_1(\underset{\sim}{\varepsilon}_i) + \ldots + c_i(m)\chi_i(\underset{\sim}{\varepsilon}_i) + \ldots + c_m(m)\chi_n(\underset{\sim}{\varepsilon}_i)$$

$$\phi(\underset{\sim}{\varepsilon}_i, m) = c_1(m)0 + \ldots + c_i(m)1 + \ldots + c_m(m)\mathrm{C} \tag{15}$$

which after evaluation yields:

$$\phi(\underset{\sim}{\varepsilon}_i, m) = c_i(m). \tag{16}$$

Thus, Eq. (12) may be viewed as an interpolation function that linearly determines the value of the dissipated energy density function at any point in the strain space as long it lies in the cuboidal region spanned by the 125 points.

The problem of determining the analytical expression for ϕ is now reduced to determining the coefficients c_i, such that the family of functions represented by Eq. (12) is restricted to one which represents a "best fit" of experimental data.

For this purpose, we assert that the total energy Φ dissipated throughout the volume of the structure under consideration (s_0) for each loading condition l_0 can be computed as the volume integral of the dissipated energy function over the spatial extent of the structure:

$$\Phi = \int_{\partial s_0} \phi(\underset{\sim}{\varepsilon}, \underset{\sim}{c})\, d\underset{\sim}{x}. \tag{17}$$

By virtue of Eq. (12), this relation reduces to

$$\Phi = \int_{\partial s_0} (c_1(m)\chi_1(\underset{\sim}{\varepsilon}(l_0, \underset{\sim}{x})) + \ldots + c_m(m)\chi_n(\underset{\sim}{\varepsilon}(l_0, \underset{\sim}{x})))\, d\underset{\sim}{x} = \int_{\partial s_0} c_i(m)\chi_i(\underset{\sim}{\varepsilon}(l_0, \underset{\sim}{x}))\, d\underset{\sim}{x}. \tag{18}$$

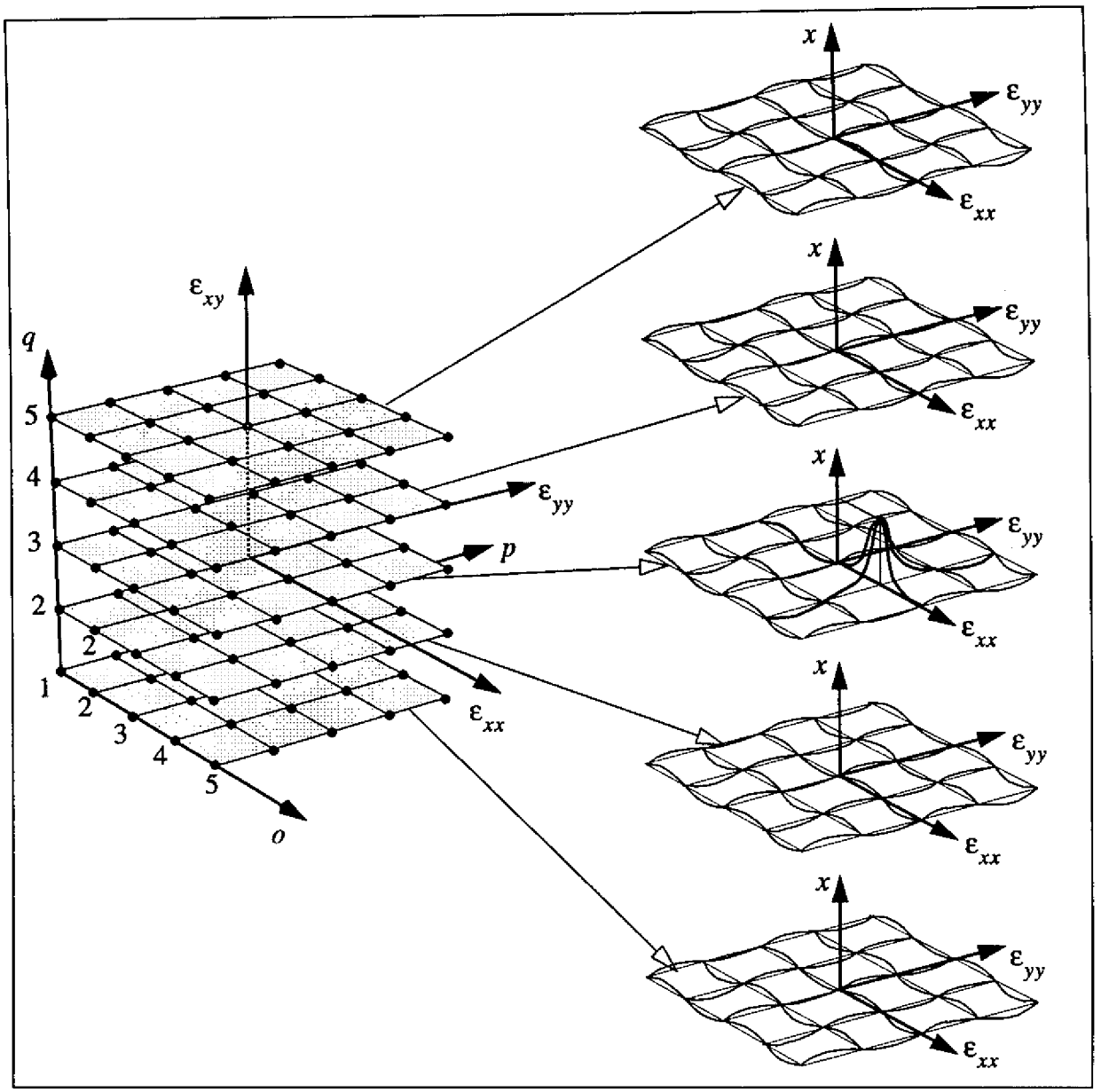

Fig. 14 — Strain space representation and characteristic representation of an indicative basis function

Assuming that D represents an experimentally obtained value of the total dissipated energy for a given structure s_0 and a given loading condition l_0, there is an appropriate selection of the coefficients c_i such that the value obtained from Eq. (18) approximates this measured value. This can be expressed by

$$\Phi(s_0, l_0) + e = D(s_0, l_0), \tag{19}$$

where e expresses the error between the two values of the dissipated energy.

3.4 Solution and Optimization Scheme

For the case of the particular specimen geometry s_0 and the particular loading case that corresponds to a corresponding experimental point p, the integral of Eq. (18) can be equivalenced by a discretized form indicating the sum of the dissipated energy of each of the 150 elements of the specimen structure. Equation (19) can now be rewritten as:

$$\sum_{e=1}^{110} c_i \chi_i (\underline{\varepsilon}^p{}_e)\, V^p{}_e + e^p = D^p, \tag{20}$$

where $V^p{}_e$ represents the volume of the element e for the loading point p.

Since this represents one of many relations we can write for different increments of the index I corresponding to different loading conditions, the set of these relations can now be represented in a matrix form:

$$[X]\,\underline{c} + \underline{e} = \underline{d}, \tag{21}$$

where $[X]$, $\underline{c}$, and $\underline{d}$ matrices have elements described by $\chi_{ip} = \sum_{e=1}^{110} \chi_i (\underline{\varepsilon}^p{}_e)\, V^p{}_e$, c_i and d^l, respectively. We selected every third point from each loading path (17 experimental points per loading path) for all 15 loading paths for a total of 255 experimental points, and $\underline{d}$ is constructed as follows:

$$\underline{d}^T = \left[[\underline{D}^p{}_1]^T, [\underline{D}^p{}_2]^T, \ldots, [\underline{D}^p{}_l]^T, \ldots, [\underline{D}^p{}_{15}]^T \right], \text{ with } p = 1, 4, \ldots, 49, \tag{22}$$

where

$$[\underline{D}^p{}_l]^T = [D^1{}_l, D^4{}_l, D^7{}_l, \ldots, D^{49}{}_l], \tag{23}$$

where the elements are obtained from Eq. (10) for each loading path l.

Equation (21) represents an overdetermined system of 255 equations with 125 unknowns. However, the requirement that the dissipated energy is a monotonically increasing function of the strains imposes a new set of constraints that can be now be expressed in the following inequality:

$$[M]\,\underline{c} \geq 0. \tag{24}$$

The array $[M]$ has 125 columns and 100 rows, since it represents a tuple of 100 additional constraints. It is defined as:

$$[M] = \begin{bmatrix} \underline{M}^T{}_1 \\ \underline{M}^T{}_2 \\ \cdots \\ \underline{M}^T{}_{100} \end{bmatrix} \tag{25}$$

where $\underline{M}^T_c$ for $c = 1, \ldots, 100$ are row matrices corresponding to each one of these constraints.

Thus the problem of determining the 125 coefficients c_i is reduced to the solution of Eq. (21) under the inequality constraints of relation (24). This combination provides a total of 355 relations, and it repre-

sents a classical optimization problem with inequality constraints where the objective is to minimize the function (objective function) $||\underline{e}||$ such that both Eqs. (21) and (24) are satisfied. This is a standard problem in quadratic programming and is readily solved using well-established numerical techniques (see for example Gill, Murray, and Wright (1981)). Appendix C gives a vector space graphical representation of the entities involved in the optimization scheme.

In light of the preceding considerations, the dissipated energy is now fully determined at all 125 points of the strain space since, as discussed previously, the computed coefficients represent the values of the dissipated energy at those points. The dissipated energy can, therefore, now be computed at any point in any material that has been tested. The strains determine the particular subregion in the cube spanning the strain space, such that a linear interpolation performed between the values of the dissipated energy at the surrounding point establishes the value of the dissipated energy at the intermediate point.

As a consequence of this, we can spatially map the absorbed energy over the specimen for each experimental point. Figure 15 shows the evolution of the dissipated energy distribution for the experimental points corresponding to 20%, 40%, and 60% of the total load (points 10, 20, and 30) in association with the total dissipated energy evolution curve for the specimen associated with loading path 11, repetition 1. These distributions were obtained by using the structural simulator described in Section 4. In these distributions,

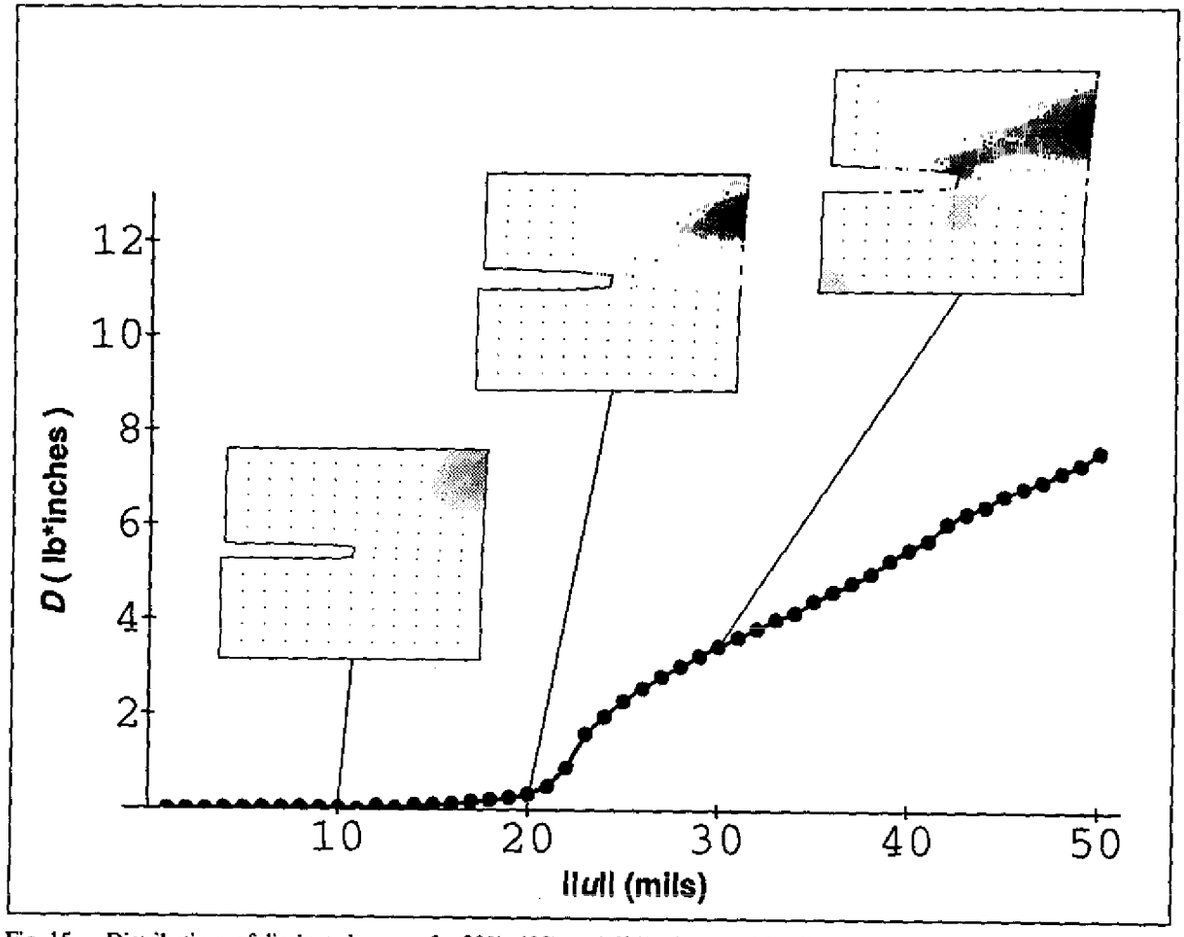

Fig. 15 — Distributions of dissipated energy for 20%, 40%, and 60% of the total loading, associated with corresponding the total experimentally measured dissipated energy for the first specimen of loading path 11

the darker the shade of gray, the higher the value of the dissipated energy density. From this figure it can be deduced that for the low load level corresponding to 20% of the total, the total dissipated energy evolution curves shows that almost the entire specimen is in the linear region because of the very small value of the dissipated energy, and the corresponding distribution shows indeed that only a very small region on the upper right corner entered into the nonlinear domain with very small values. As the load increases, the total dissipated energy of the specimen increases and, as expected, more areas in the specimen enter into the nonlinear region, while the old ones intensify their absorption levels.

4. APPLICATIONS ON NAVAL STRUCTURES

In this section we develop the idea of a *structural response simulator* and show how the computed energy dissipation functions can be used within the simulator to design structural components and predict various aspects of their mechanical behavior.

Because dissipated energy is taken as a measure of internal structural damage, one use of a simulator would be for structural designers to examine simulated spatial dissipated energy distributions to form selection criteria for evaluating the structural response of structures at a particular state of the design process. Material system designers could also use a simulator to generate spatial dissipated energy maps from which they could determine the material response of a composite material system, and then select sets of manufacturing parameters to optimize the damage tolerance of new systems. Using the simulator to analyze material softening distribution patterns could also assist in selecting a material system for a particular structural design. Finally, a structural response simulator could even be used to qualify material systems by using far more realistic qualification criteria than are currently employed, e.g., strength or fracture toughness, which only indirectly and partially assess some qualitative aspects of the materials. Indeed, it is shown in this section that higher strength does not necessarily imply better damage tolerance.

4.1 Structural Response Simulator

To provide the engineering community with a tool for addressing the types of problems discussed above, a structural response simulator was created that takes user-specified geometries, materials, and loading conditions as inputs and creates spatial material distributions of local stiffness loss using the experimentally obtained dissipated energy functions. Figure 16 shows the architecture of the structural response simulator in the configuration used to generate the results presented in this section. It has since evolved into a much more sophisticated form and its design now includes such advanced functionality as user-simulator interaction modelling via artificial neural nets and other techniques.

The Fig. 16 block diagram shows the structure of the simulator in terms of component subsystems. The user interface was created by writing a library of function calls using the "PATRAN Command Language" (PCL) that allows the user to specify the geometry, the material, and the loading for the structure of interest. Visualization capabilities are provided through PDA's "PATRAN" 2.4 solid modeling package. A finite element idealization of the structure is achieved through appropriate use of PCL and all relevant model information is stored in "PATRAN" neutral files on the mass storage memory resources of the computer system hosting the simulator, which is currently a Silicon Graphics Iris 4D/70GT with 16 Mb of RAM and 1.5 GB of mass storage memory. The actual finite element analysis is performed by using the "ABAQUS" finite element code on a CRAY X-MP-24 and assuming linear elastic behavior. The objective of the finite element analysis is to generate the strain field in the structure for the initial elastic state. The data required by "ABAQUS" are provided by the "PATABA" process that translates the "PATRAN" neutral files to an "ABAQUS" input file. The output from "ABAQUS" is stored in a file that is subsequently converted to a strain file and a displacement file in "PATRAN" format by the "ABAPAT" process. The displacement files are identified by the suffix ".dis" and the strain files have the suffix ".els." At this stage, the strains and dis-

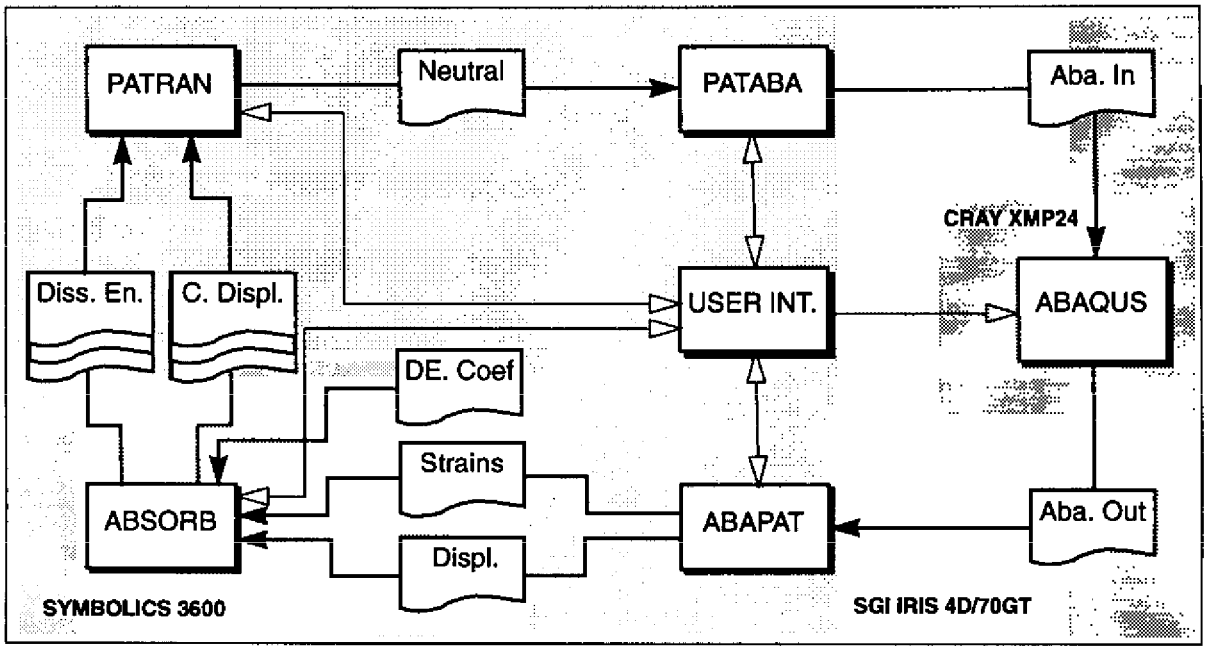

Fig. 16 — Block diagram of the architecture of the structural simulator and computational resource allocation

placements can be visualized from "PATRAN" or be fed into the dissipated energy module "ABSORB" which runs on a Symbolics 3600 and generates a spatial energy absorption map by associating a value of dissipated energy with each strain combination at every spatial evaluation point. The required dissipated energy values are computed by interpolation using the coefficients in the file "rmt.x.y.pred" that were produced by the process depicted in Fig. 12. Finally, the white arrows that connect the user interface module with the other simulator modules signify user control over these modules through both the user interface and the networking TCP/IP utilities that control intermachine data transfer.

4.2 Ship Mast

One of the design goals is to investigate the merits of using composite materials for ship masts. The primary reasons composite masts are being considered are weight reduction and favorable radar return characteristics. Traditional designs for metal masts were based on the assumption of linear elastic behavior and stress-based damage criteria; namely, that internal load-induced damage was assumed to occur whenever the stress exceeded a specified maximum stress set at 2.5 times the yield stress for the material used. As mentioned previously, such a simplistic view of failure behavior is not justified in composites, and a more realistic damage model such as the one being proposed in this study is required. The enhanced understanding provided by such a model should lead to lower safety factors and, therefore, more efficient mast designs. The structural response simulator together with a database of computed dissipated energy functions represent a unique medium to achieve the efficient design of composite masts.

The DDG-51 class of frigates was selected as a candidate ship for a representative mast installation. The geometry of the mast is that of a tripod mast with a rectangular box beam and two struts with two antenna platforms attached to it and the associated deckhouse as shown in Fig. 17.

The design loads selected for this case were extracted from the "DDS-170" manual. For demonstration purposes, a wind load of 30 psf (lb/ft^2) corresponding to a 90 kn head wind was selected. In addition, an inertial load of 0.6 g's applied downwards to the center of gravity of the mast, or 0.2 g's applied upwards

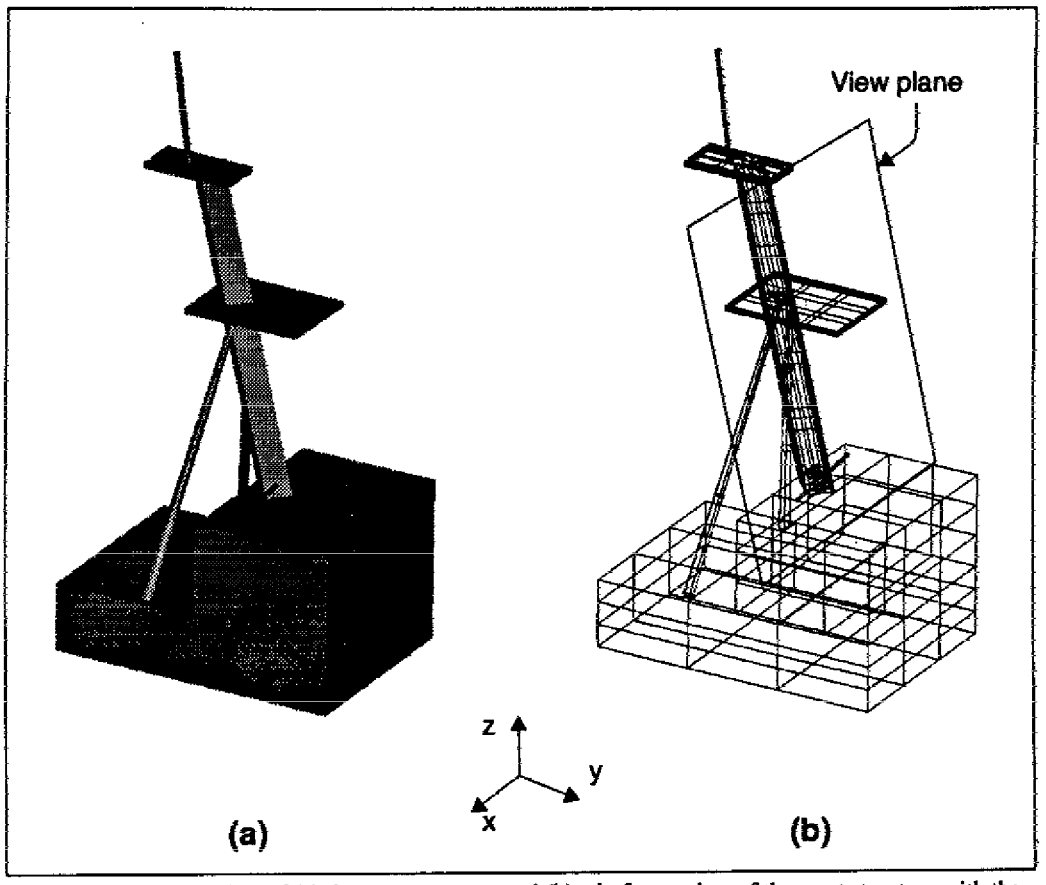

Fig. 17 — Rendered view of (a) the mast structure and (b) wireframe view of the mast structure with the view plane used for displaying the dissipated energy density distributions

on the center of gravity of the mast. A 500 lb antenna load was assumed to be applied at the upper platform and a 1000 lb antenna load applied at the lower platform of the mast were also considered. Only the case of head-on wind load is presented here, however.

The materials used for this simulation were item 007 (Resin 3501-6, Fiber AS4, Layup +/- 60°) and item 040 (Resin PEEK, Fiber AS4, Layup +/- 60°) as described in Table 1. These materials were selected to establish the relative merits of the thermoset 3501-6 resin material vs the thermoplastic PEEK resin material. The material was composed of 130 successive plies of 0.0075 in. each, thus accounting for a total thickness of 0.975 in.

Figure 18 shows the dimensions and the finite element mesh for the simulation of the mast structure itself. A total of 106 "ABAQUS" "QUAD" elements were used for the finite element idealization. In addition, battle damage was simulated by considering a 5 inch hole at the right side of the foot of the mast as shown in Fig. 18.

Figures 19 through 22 present the simulation results for different loading and material choices as seen from the front of the mast in the region indicated in Fig. 17 with a rectangular window. All figures are fringe plots of the dissipated energy distribution over the structure. In all of these figures, the views on the left represent the dissipated energy distribution for the 3501-6 thermoset material, and the views on the right represent the dissipated energy distribution for the PEEK thermoplastic material.

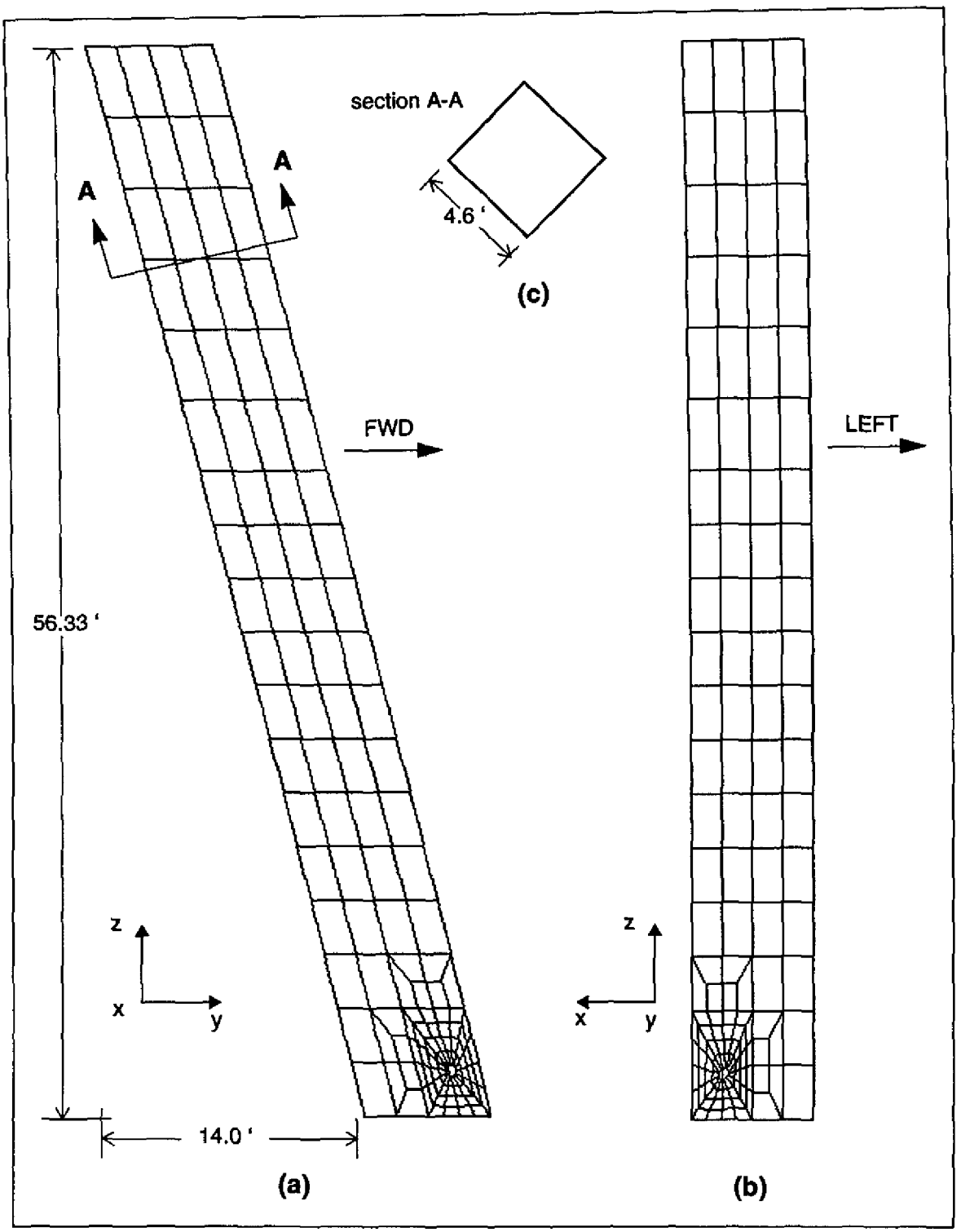

Fig. 18 — Right side view of the finite element meshing and dimensions of the mast (a); front view of the mesh (b); cross section of the mast (c)

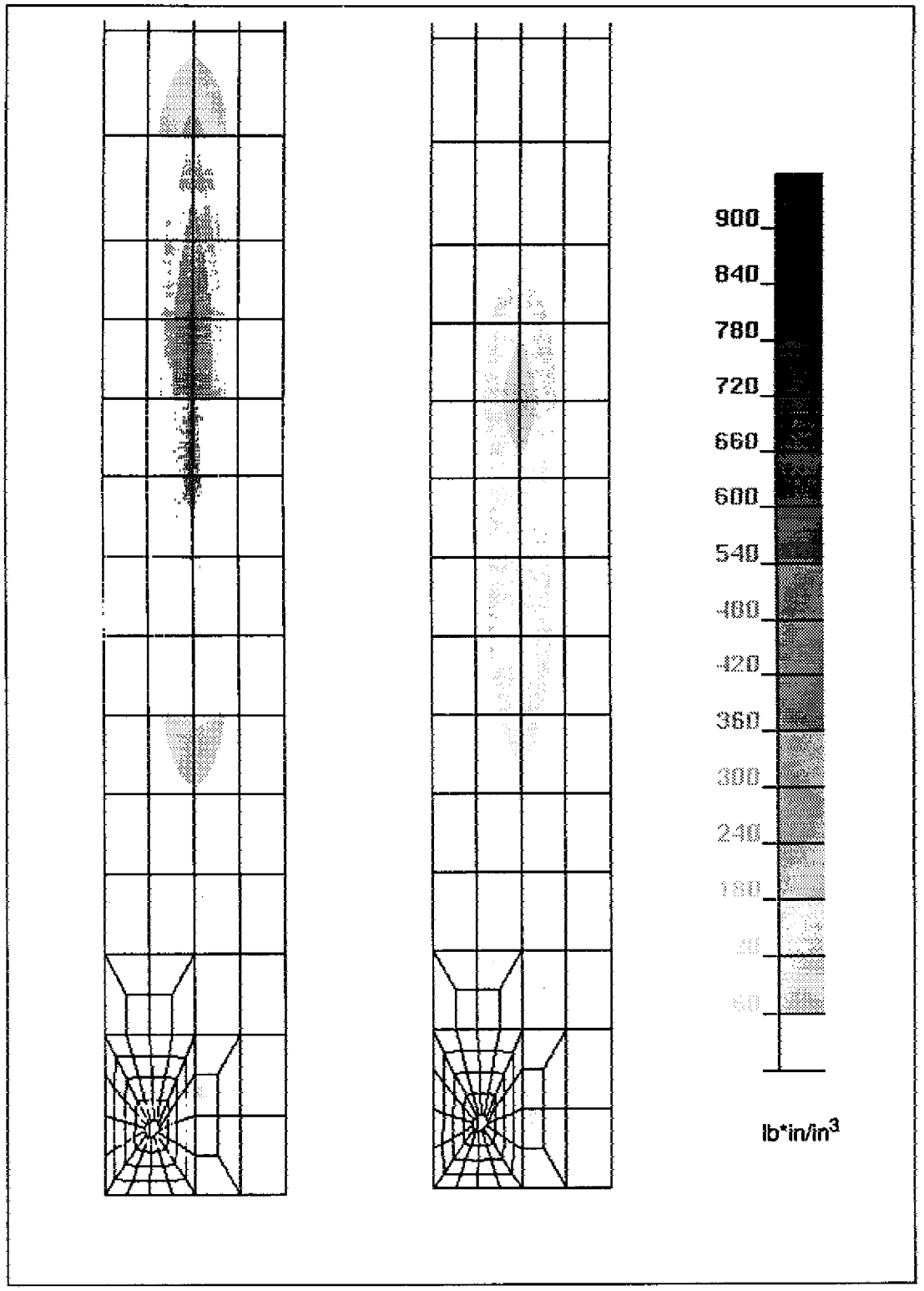

Fig. 19 — Front views of dissipated energy distributions of ship mast made out of thermoset material 007 (AS4/3501-6 [+/-60°]) (left) and out of thermoplastic material 040 (AS4/PEEK [+/-60°]) (right), for 1x of the total loading corresponding to front wind

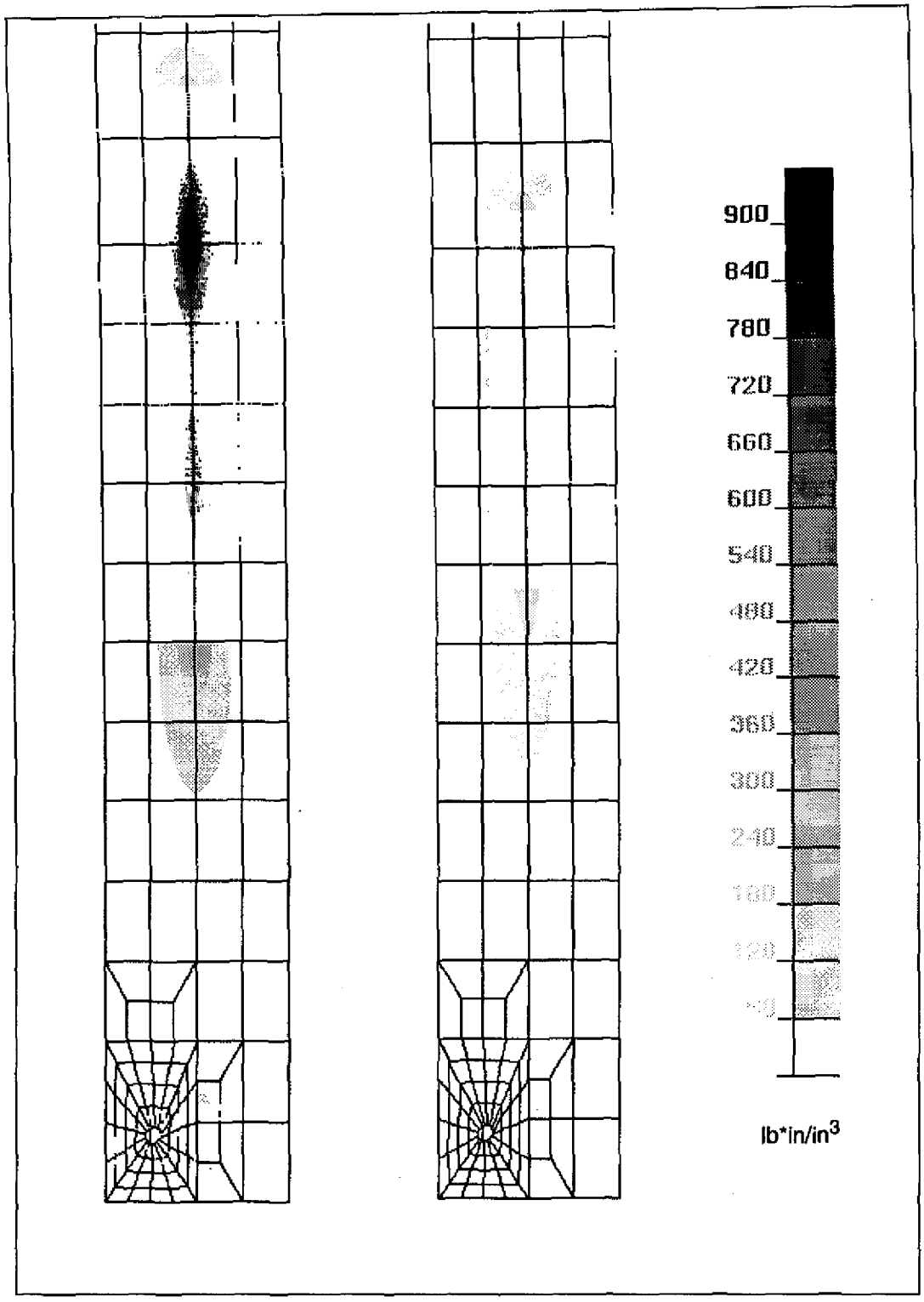

Fig. 20 — Front views of dissipated energy distributions of ship mast made out of thermoset material 007 (AS4/3501-6 [+/-60°]) (left) and out of thermoplastic material 040 (AS4/PEEK [+/-60°]) (right), for 2x of the total loading corresponding to front wind

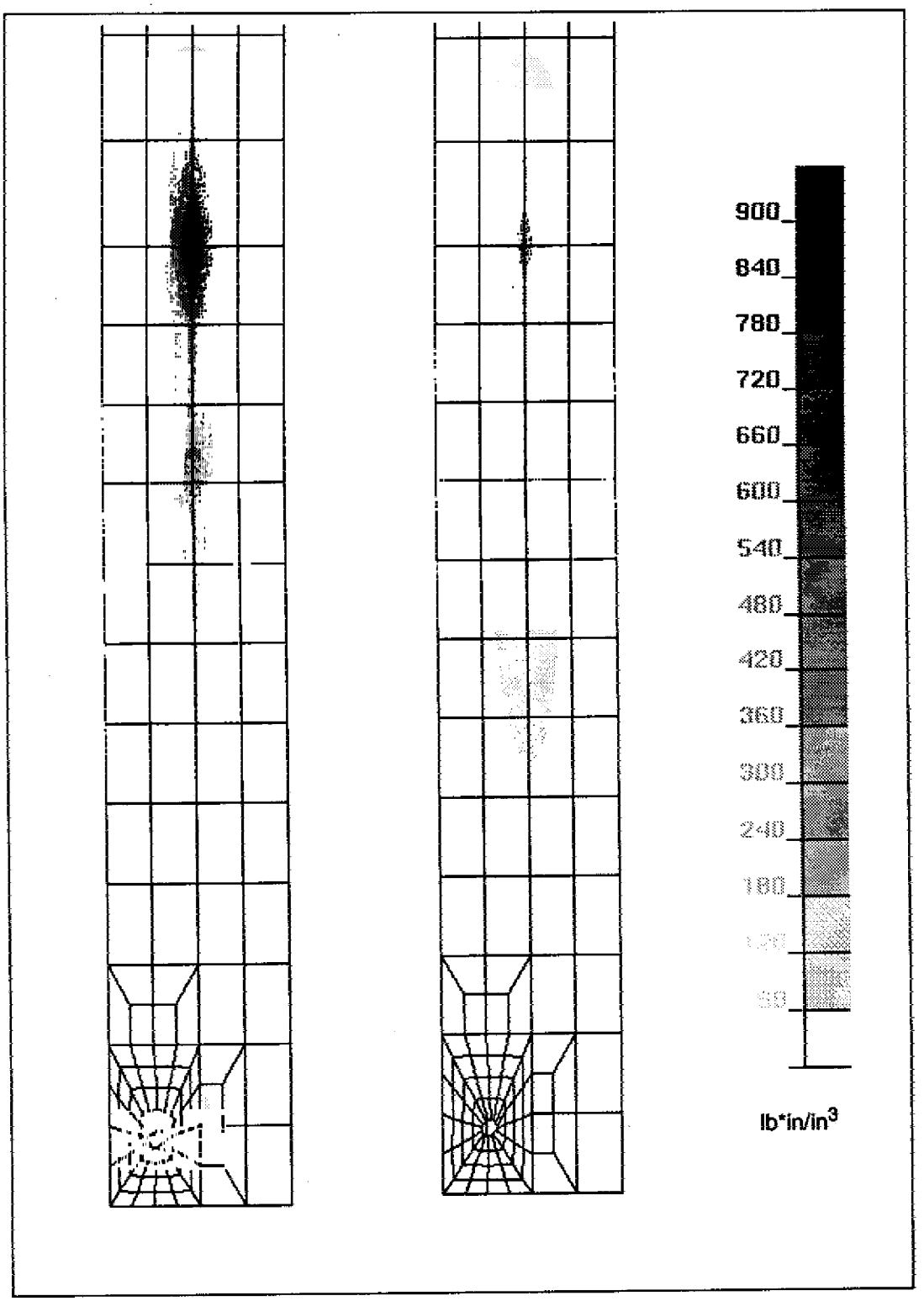

Fig. 21 — Front views of dissipated energy distributions of ship mast made out of thermoset material 007 (AS4/3501-6 [+/-60°]) (left) and out of thermoplastic material 040 (AS4/PEEK [+/-60°]) (right), for 3x of the total loading corresponding to front wind

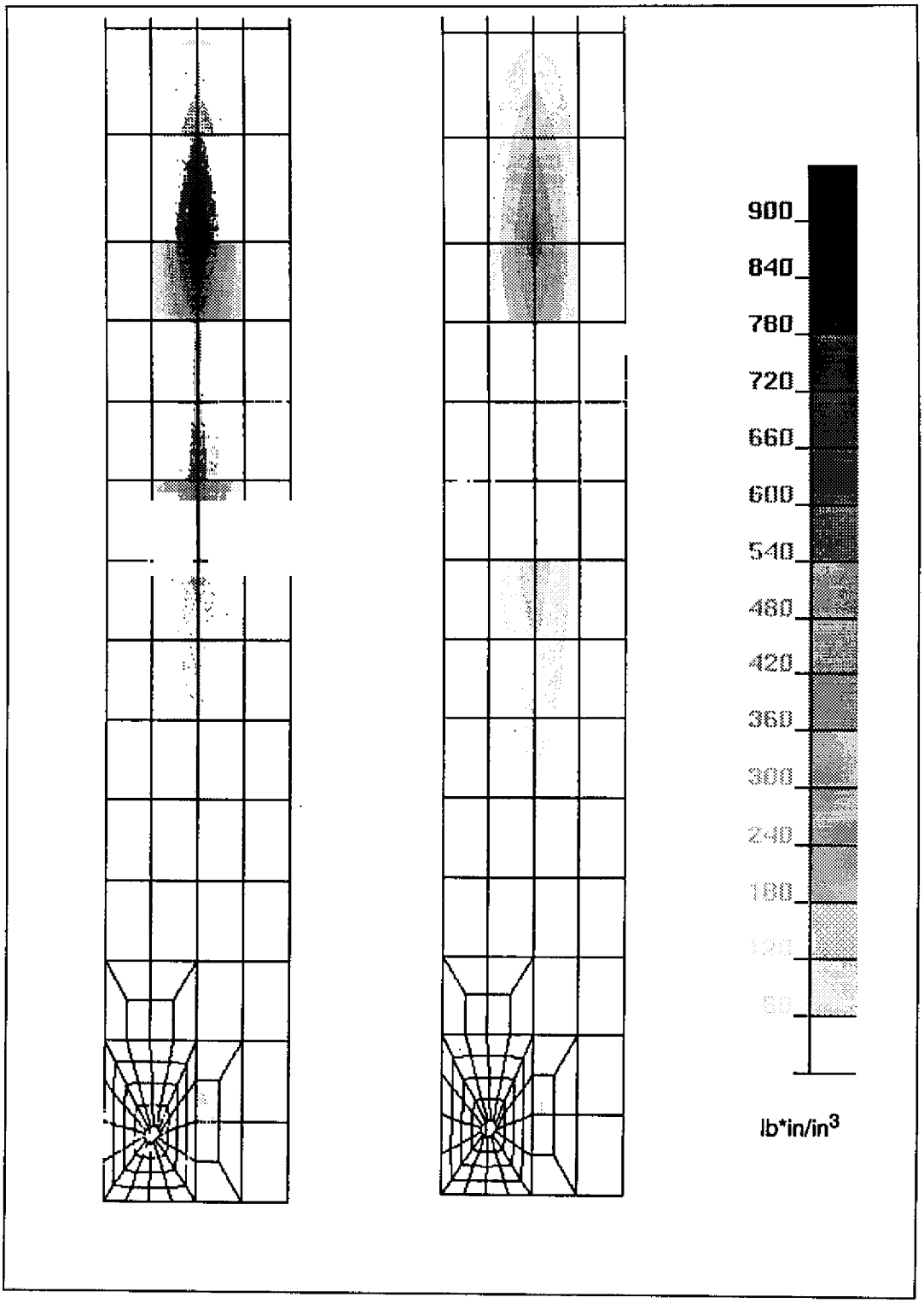

Fig. 22 — Front views of dissipated energy distributions of ship mast made out of thermoset material 007 (AS4/3501-6 [+/-60°]) (left) and out of thermoplastic material 040 (AS4/PEEK [+/-60°]) (right), for 4x of the total loading corresponding to front wind

The effect of applying an increasingly higher load corresponding to front wind is manifested as an increasingly higher distribution of fringes for higher levels of loading. Each one of these figures has been plotted for 1x, 2x, 3x, and 4x overload levels of the original 30 lb/ft^2 loading in the same order they appear in the document.

Another characteristic of the response of the structure due to the increasing load is the effect demonstrated in Fig. 23 where the maximum dissipated energy is plotted as a function of the load magnitude. That is, after a certain loading level, the material reaches a saturation level, where the dissipated energy in the material ceases to increase. This was the reason the distributions of overload magnitudes 4 and 5 were almost identical and, therefore, it seemed appropriate not to present the plotted distributions for loading magnitude 5. Evidence of this can be seen by comparing the dissipated energy distributions for loading magnitudes 3 and 4 in Figs. 21 and 22.

A significant observation is that the 3501-6 material seems to show a significantly higher propensity to go into its nonlinear region than does the PEEK material. This is evident from the higher number of fringes and their higher intensity as they appear on the 3501-6 distributions in Figs. 19 through 22 compared to those of the PEEK in Figs. 19 through 22. In addition, the 3501-6 material also has the tendency to dissipate higher amounts of dissipated energy as is shown by the saturation levels in Fig. 23.

As is apparent from all these figures, the mechanical damage, in terms of dissipated energy, caused by the round penetration on the left side of the base area of the mast is negligible compared to the one on the middle level of the structure.

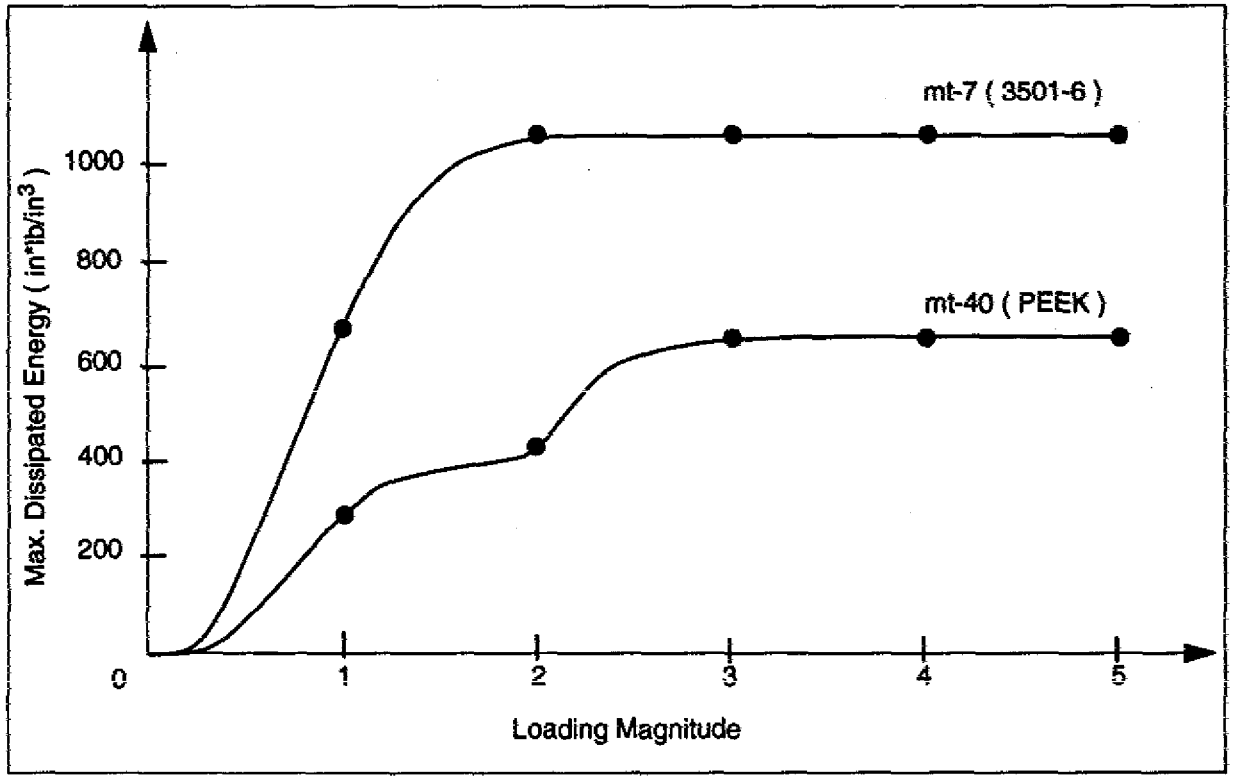

Fig. 23 — Distribution of the maximum dissipated energy of the ship mast structure for materials 007 (AS4/3501-6 [+/-60°]) and 040 (AS4/PEEK [+/-60°]) , vs the loading magnitude

4.3 In-Plane Loader Specimens

The specimen used in the IPL tests is an example of a structural object. It has structural loads, i.e., the loads applied by the IPL actuators. It has a structural geometry, i.e., the geometry of the specimen. And it has a structural material, i.e., the material under investigation.

At any point within the structural object, strains are induced that act upon the material. In this instance, strains induced by the actuator loads act upon the specimen material. The strains are occasionally the same at different points of the specimen, but in general they are not. The strains act upon the specimen material, changing it on occasion. When the strains do change, the material shows the change by exhibiting a different elastic behavior suggesting reduction in local stiffness (softening).

The experimentally determined dissipated energy is a measure of material softening. It is a nonlinear, monotonic function of the strains that act upon the material. As such, the material exhibits behavioral changes that may be unexpected.

This application uses the IPL structural object to showcase the nature of the unexpected behavior.

Continuing in the spirit of Sections 2 and 3, material 002 in Table 1 was used as the *straw person* in this application. With a layup construction of $[(+30/-30)_4]_S$, this laminated composite material has plies constructed from AS1 carbon fibers, and 3501-6 epoxy resin.

Load icons were employed in the figures of this application to facilitate recognition of the particular load combination being applied to a specimen. Five graphic symbols were used in combination to produce these icons. They are: a clockwise arrow to indicate clockwise motion of the movable boundary of the specimen; a counterclockwise arrow to indicate the opposite motion; an upwards-pointing arrow to indicate motion of the points of the movable boundary parallel to the y-axis; a downwards arrow for the opposite motion; and a right-pointing arrow to indicate motion of the points of the movable boundary parallel to the x-axis.

The interpretation of a particular combination of the graphic symbols is that the corresponding combination of IPL applied motion is applied proportionally to the specimen's movable boundary. The specimen, caught between its movable and immovable boundaries, deforms with a compatible motion. Loads that are proportional to each other are represented by the same icon. The particular magnitude of the proportional load is indicated individually, or by group where applicable.

That specimen dissipated energy is *a continuous nonlinear monotonic function of load displacement magnitude* is an experimentally determined fact. The material dissipation energy is forced to be *a continuous nonlinear monotonic function of strain magnitude.* How this was done is explained in Section 3; the point being that though the specimen, undeniably, is nonlinear monotonic, the computed material dissipation function behaves that way *by analytic design.*

Figure 24 depicts the loading case for load path 11 (lp-11). The load magnitudes shown are 20, 40, and 60 percent of the maximum boundary motion applied during the experiment for this particular specimen. Figure 24 also illustrates the monotonic nature of dissipated energy with respect to strains. Dissipated energy never decreases with increasing magnitudes of loading. It is also apparent here that the dissipated energy may not increase after reaching a certain magnitude of strain, and that a minimum magnitude of strain is required before the dissipated energy can become greater than zero. This observed behavior corresponds precisely to what we mean by the term a *nonlinear monotonic function of strain magnitude.*

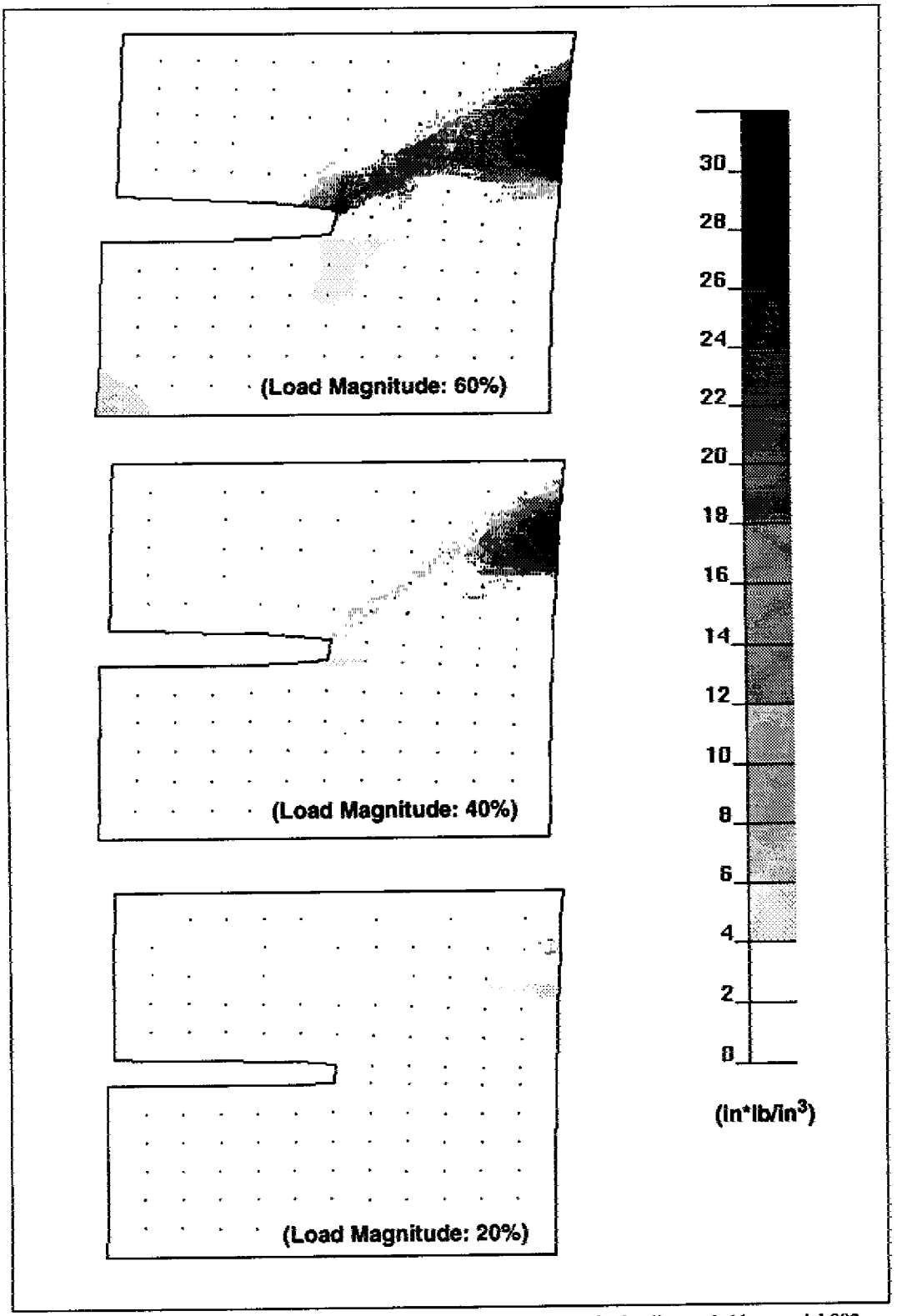

Fig. 24 — Distributions of dissipated energy on the deformed specimen for loading path 11, material 002 (AS1/3506-1 [+/- 30°]) for three different magnitudes of loading

To reiterate, that specimen dissipated energy is *a continuous nonlinear function of load combination* is an experimentally determined fact. In computing the material dissipation energy function from the specimen dissipated energy, the only analytic control exercised is to ensure continuous behavior with respect to the strain combination. Consequently, the nonlinear effect of strain combination as illustrated in Figs. 25, 26, and 27 is closely related to the experimentally *observed behavior.*

Figures 25, 26, and 27 all depict the same set of the 15 different load combinations used in obtaining the experimental results. Figure 25 is for the case of 20% of full load magnitude, while Fig. 26 is for 40%, and Fig. 27 for 60%. The effect of opening vs closing motion (lp-14 vs lp-2), which may be likened to tension vs compression behavior, is quite distinctive. At the 20% level, both cases are indistinguishable. At the 40% load level, the opening or tension case has developed an extensive *hot* area from the notch tip out along the +/- 30^{0} fiber directions all the way to the edge of the specimen, while the closing or compression case has changed only slightly. At the 60% load level, the situation has changed dramatically again. The compression case has developed a *hot* zone of the same configuration as that for tension. But while the zone for opening is diffuse, that for closing is concentrated at the notch and at the edge.

The effect of opening, sliding, and closing load combinations (lp-14, lp-8, lp-2), demonstrates clearly the distinction between linear effect and nonlinear effect. The opening and sliding combination is lp-11. Lp-14 and lp-8 both show extensive zones of nonzero dissipated energy in the lower half of the specimen. A linear effect would show dissipated energy as a proportional sum of the dissipated energy from cases lp-14 and lp-8. Clearly, lp-11 shows no nonzero dissipated energy in the lower half of the specimen. The effect is typical of nonlinearity. The sliding, closing combination, lp-5, exhibits the same nonlinear effect.

The general assertion is that "if the IPL experiments were conducted using another specimen shape, then the material dissipation energy function would be the same." In other words, the material behavior should be independent of the structure or of the loads that may be applied to that structure. If the preceding discussion had been about this alternative experimental specimen, then the different specimen shape would have produced different strain distributions and consequently different material dissipated energy distributions. The same general continuous, nonlinear, monotonic nature of the material dissipation energy function would have been noted, but their distributions within the specimen would have been different. If a strong relationship had been drawn between the specimen, its loadings, and the consequent distributions of material dissipated energy from the cases presented, then a different strong relationship would have been drawn from consideration of the results for the alternative specimen.

The danger is in attempting to infer material behavior from specimen behavior, without regard to how the strains are distributed within that particular specimen.

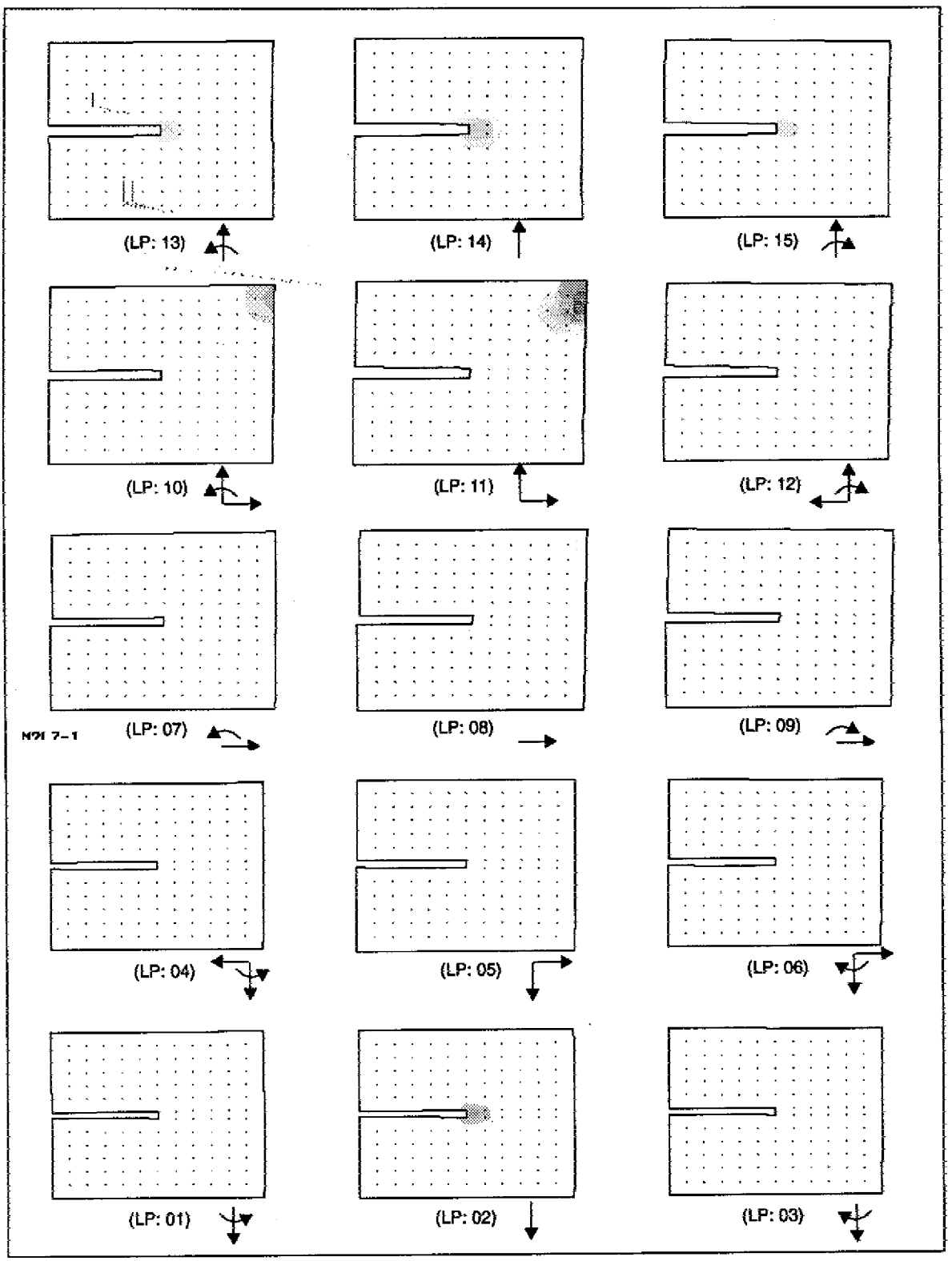

Fig. 25 — Distributions of dissipated energy on the deformed specimen for load magnitude 2, material 002 (AS1/3506-1 [+/- 30°]), for each of the load paths 1-15

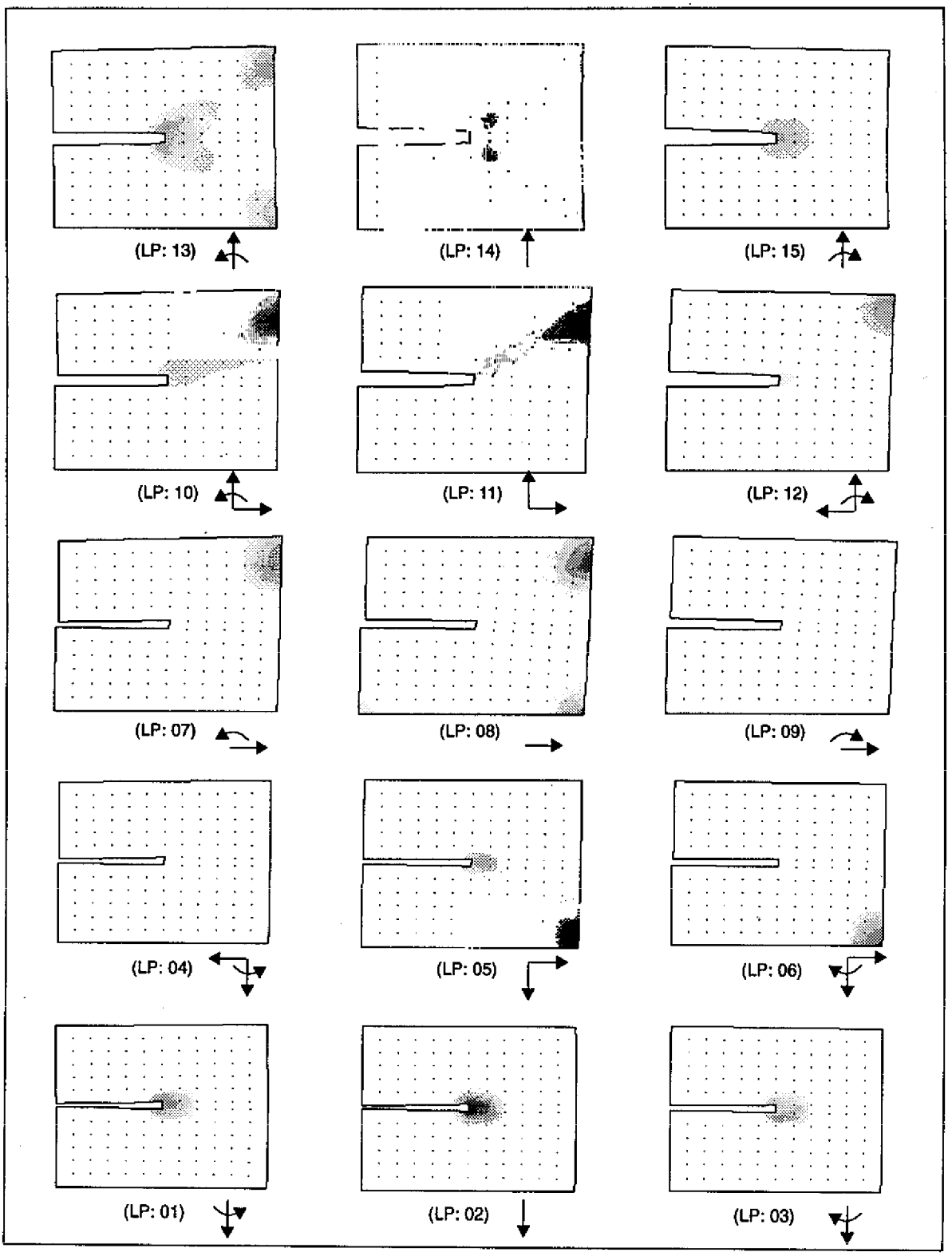

Fig. 26 — Distributions of dissipated energy on the deformed specimen for load magnitude 3, material 002 (AS1/3506-1 [+/- 30°]), for each of the load paths 1-15

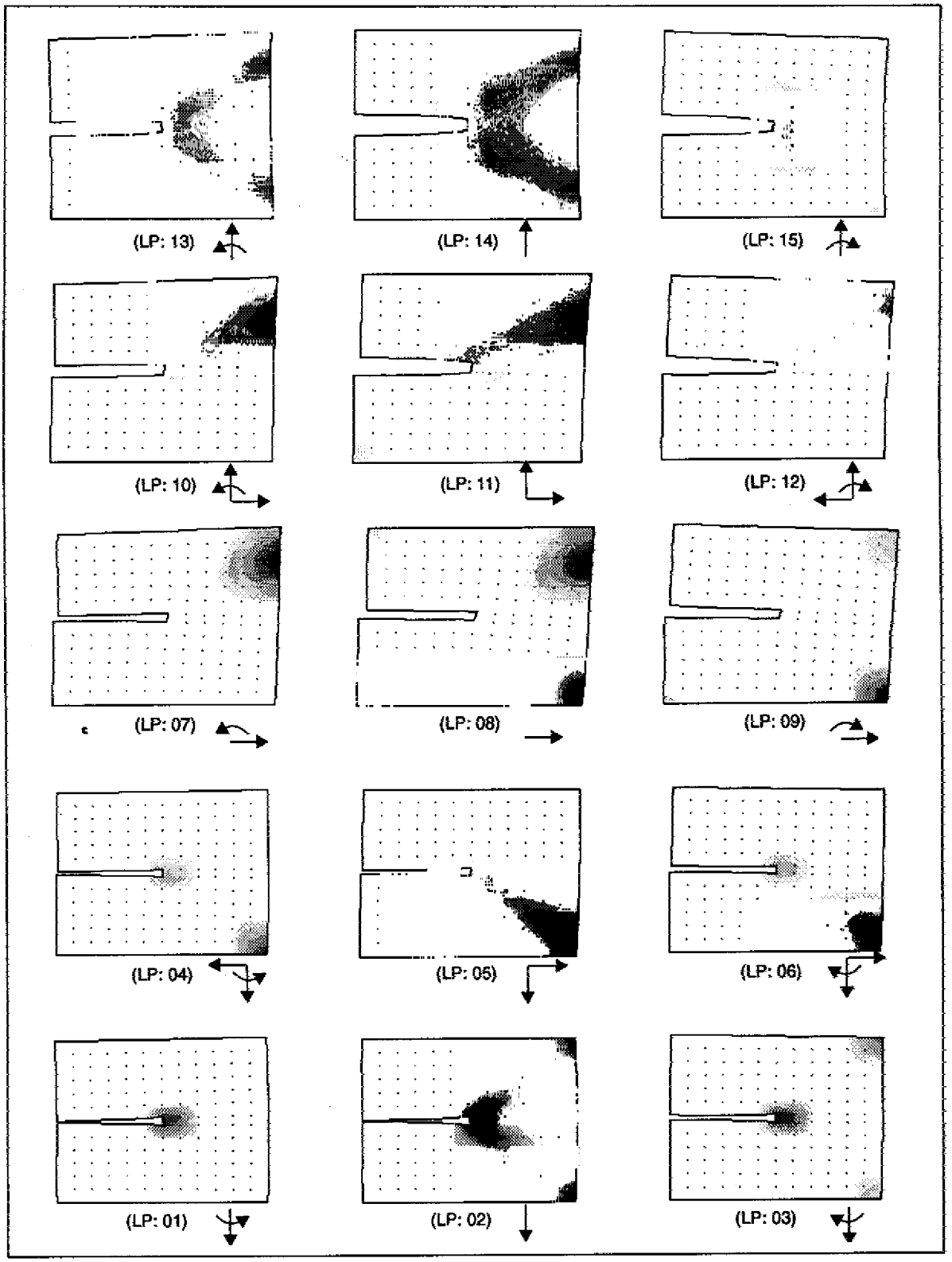

Fig. 27 — Distributions of dissipated energy on the deformed specimen for load magnitude 4, material 002 (AS1/3506-1 [+/- 30°]), for each of the load paths 1-15

4.4 Submarine Hull

An underwater structure, such as a submarine, is subject to a vast range of loads. These loads vary from underwater explosions, underwater wave actions, maneuvering loads, depth loads, to a whole variety of other types of loads. The survivability of the structure under these conditions is of prime importance.

Since their invention, submarines have mainly been constructed from metals, but today, composites are being considered as a viable alternative. Dissipated energy offers a means of mapping out or *hot spotting* areas of concern on composite submarine structures. The structural loads, structural geometry, and the structural material act to produce strains throughout the structure that may induce changes in the material. Dissipated energy as a function of strain determines when a material will change from one elastic state to another, and is an important means of measuring both the extent of the material changes and the structural survivability.

In this application, we consider a generic submarine and, in particular, analyze the cylindrical hull section. The actual dimensions used are those of a generic dry dock shelter. The cylindrical shell idealization was selected as a simple showcase for dissipated energy mapping.

The finite element model used is shown in Fig. 28 and consists of 256 shell "QUAD" elements. The cylinder that was analyzed was 100 inches long, 80 inches diameter, and 1 inch thick. The boundary loading conditions were those induced by rigid body plane rotations of the ends of the cylinder. These loading conditions where chosen as a nominal representation of the kinds of loads that might be carried through to the cylinder by the rest of the submarine in response to bending loads about the vertical or y-axis.The shell material was a laminated graphite thermoset epoxy. The layers were oriented at +/- 60° to the longitudinal, or z-axis. The fibers were AS4 and the resin was a 3501-6 type epoxy.

The finite element code "ABAQUS" was used to determine the interior strain field.The strains as reported back by the code are for the Gauss integration points used by "ABAQUS" to determine the shell properties. Three integration points were used in this analysis, one point at the center of the laminate and two points at about an eighth of the thickness in from each side. In this case, the dissipated energy is not computed on a per ply basis, but rather on a smeared-out point basis, or a *partial dissipated energy* number at an integration point. Gaussian integration is then used to compute a *total dissipated energy* through the thickness. Both types of dissipated energy are illustrated in the following figures where the partial dissipated energy at the outer part of the shell is shown in Fig. 28 and total dissipated energy in Fig. 29.

Figure 29 depicts the dissipated energy maps for overloads of 7X, 9X, 11X, 13X and 15X. The values shown are for partial dissipated energy close to the outer side of the shell. As can be seen in Fig. 29, the boundary of the hot-spotted zone (higher values of dissipated energy) at 7X overload is practically the same as at 15X overload. An observer may interpret this in several ways; however, it is reasonable to surmise that the damage as indicated by the hot-spotting is not going to grow unstably, and that regardless of the point of view taken as to the meaning of the damage, the material degrades only so far and thereafter gets no worse.

Figure 30 depicts the distribution of dissipated energy from below the inside surface, the outside surface, and throughout the thickness, i.e,. partial vs total viewpoints. The partial viewpoints show both similarities and differences. In both, the extent of the hot zone is roughly the same; however, each exhibits markedly different distributions within the zone.

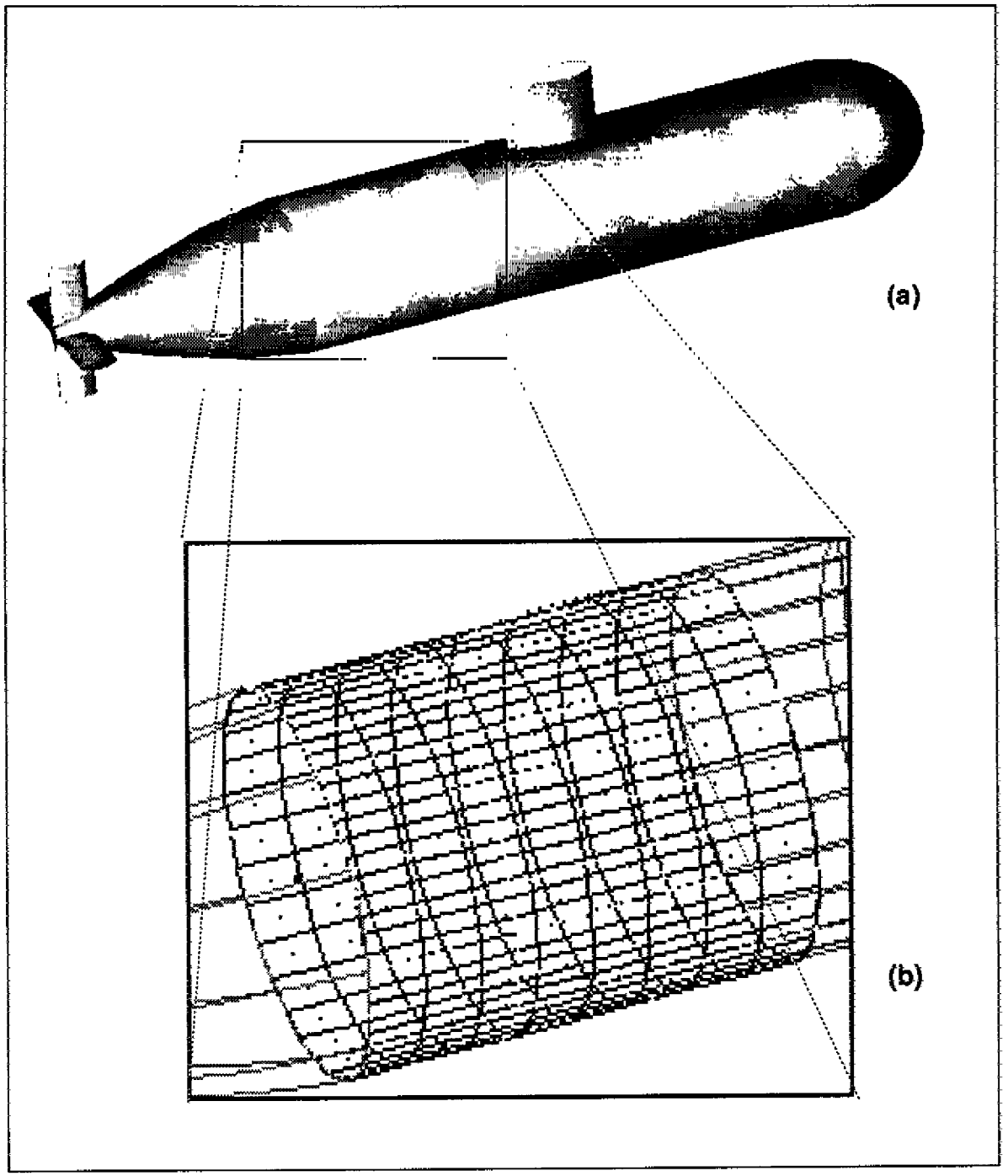

Fig. 28 — Cylindrical shell as a section of (a) an idealized submarine , and (b) the corresponding finite element mesh

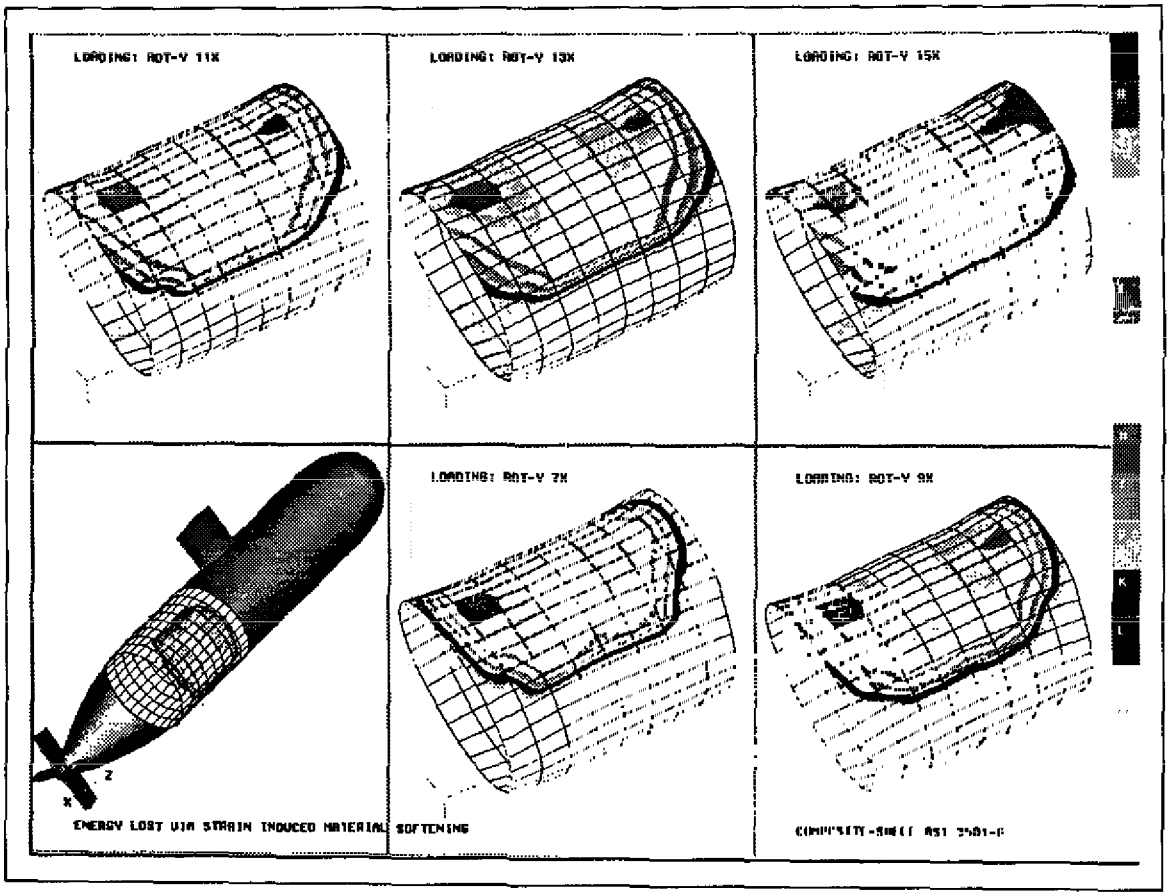

Fig. 29 — Dissipated energy distributions at the outer surface of the shell structure, for loading magnitudes of 7,9,11,13, and 15 times overload

The total dissipated energy viewpoint shows a larger hot zone than either of the partial dissipated energy maps. It also shows a rather constant value of dissipated energy over the area of the hot zone.

From this an important inference may be drawn, that the nonlinear effect of strain on material loss of local stiffness, or change, may not be characterizable strictly on the basis of a partial or a total viewpoint.

5. A GENERAL PROCEDURE FOR DETERMINING THE DISSIPATED ENERGY DENSITY FUNCTION AND A DESCRIPTION OF MATERIAL CONSTITUTIVE BEHAVIOR

The approximate procedure for determining the dissipated energy function $\phi(\underline{\varepsilon})$ discussed in Section 3 is currently included in the response simulator. As presently formulated, this procedure has the following shortcomings: first, the required strain fields are computed by assuming linear elastic behavior and by using the elastic constants corresponding to the "virgin" material, rather than by using the proper nonlinear constitutive behavior, and second, the procedure is formulated only in terms of a particular piecewise linear collocation set of basis functions for representing $\phi(\underline{\varepsilon})$, rather than in terms of arbitrary basis functions.

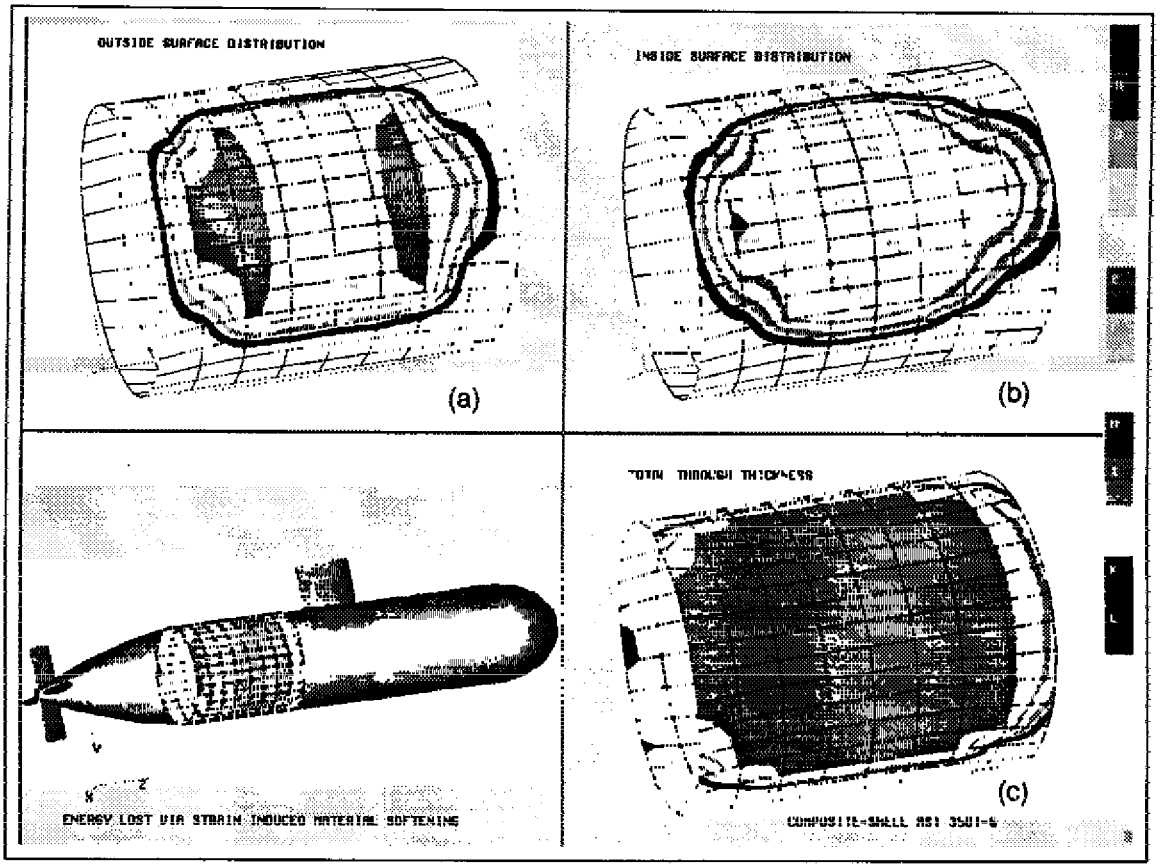

Fig. 30 — Dissipated energy distribution for (a) the inside surface of the shell, (b) the outside surface of the shell and (c) integrated through the thickness.

Both of these issues are addressed in the present section and the underlying assumptions involved in the material model are carefully laid out.

To determine the dissipated energy function, we regard the composite as being composed of either a single mechanically equivalent homogeneous anisotropic material, or a collection of layers of varying orientations of such materials. Provided that the applied loads are either quasi-static or dominated by low temporal frequencies, these homogenization procedures should provide acceptable models since it is expected that the wavelengths corresponding to the spatial variation of the stresses, strains, etc. should be large compared to the microstructural characteristic lengths. If this is not the case, events on the micro scale can take on a predominant role and cause significant inaccuracies.

We also postulate that the material constitutive behavior can be completely described by specifying stress as a function of only strain and a set of internal state variables, i.e.,

$$\underset{\sim}{\sigma} = \underset{\sim}{C}(\underset{\sim}{\xi},\underset{\sim}{\varepsilon}), \tag{26}$$

where $\underline{\underline{C}}(\underline{\xi},\underline{\varepsilon})$ is a nonlinear fourth order tensor function and $\underline{\xi}$ is the state variable vector. The form of Eq. (26) thus obviously precludes dealing with materials that exhibit marked strain-rate-dependent behavior. Finally, we ignore any residual stresses or strains which may exist when the loads are removed such as those induced by the curing process.

The form of the above constitutive relation implies a *restricted* implicit type of path dependency in the sense that any path dependent behavior results only from internal state transitions that are reflected by changes in the state variables $\underline{\xi}$, and not from an explicitly stated load history dependence. This section considers this issue in more detail. It suffices to state here that for the most part the material behaves in a manner similar to that of a hyperelastic material (a nonlinear elastic material with a strain energy potential) as long as the state variables $\underline{\xi}$ remain unchanged. Thus, for example, when a material point is loaded up to a specified strain, the subsequent structural response is dependent solely on the current strains and is independent of deformation history provided no unloading takes place. Upon unloading, the material behaves elastically in that no further internal material damage takes place, however, a state transition occurs when the unloading commences, and it is this state transition that is responsible for any memory the material might have of its previous loading history. As mentioned in the introduction, this material model and its particular type of path independence is similar to the model employed by Schapery (1987, 89a, 9b, 90). Moreover, it is consistent with the observations of Lamborn and Schapery (1988) who observed a type of path independence for a range of tensile and torsional loads in several graphite-epoxy systems.

The remainder of this section describes a general procedure for determining the dissipation density function using boundary force and displacement data obtained from IPL tests. The procedure is a deconvolution process in the sense that the observations reflect both the effects of material behavior and specimen geometry, and that the geometric effects must be factored out to obtain information relating to the material alone. We also present a derivation of the precise analytical form of the constitutive equations.

5.1 Caveats

In the course of our analysis we have introduced a number of assumptions and simplifications, some having already been mentioned. Nevertheless, we itemize them below in their entirety for the sake of completeness:

- The material can be regarded as a mechanically equivalent homogeneous anisotropic material as discussed above. In an angle-ply composite, this assumption can be applied either on a ply-by-ply basis or to the collection, as appropriate.
- Loading is either static or slowly varying in accordance with the considerations already discussed.
- The material behavior can be represented as $\underline{\underline{\sigma}} = \underline{\underline{C}}(\underline{\xi},\underline{\varepsilon})$ discussed previously. This assumption by definition precludes consideration of materials that exhibit marked viscous, rate, and explicit load history dependencies. Moreover, given this assumption, a so-called work potential (energy per unit volume), $\psi(\underline{\varepsilon})$, can be defined such that $\underline{\underline{\sigma}} = \text{grad}_{\underline{\varepsilon}}\psi(\underline{\xi}, \underline{\varepsilon})$ (Schapery 1987).
- The total energy absorbed by the material during loading can be regarded as being composed of the sum of a reversible (recoverable) and an irreversible (dissipative) part. The reversible component is the energy that would be recovered if the material were to unload, whereas the irreversible part represents the energy which is dissipated by the internal damage mechanisms. The latter can be described by a dissipation density function $\phi(\underline{\varepsilon})$ (dissipation energy per unit volume).
- The constitutive relation is continuous in both stress and strain.
- The deformations are sufficiently small so that the infinitesimal stress and strain tensors may be employed.

- Only shell-like structures are considered so that the stress and strain fields in either the entire material or in each ply are two-dimensional with no transverse components, i.e., the stresses and strains can be regarded as vectors having the form $\underset{\sim}{\sigma} = (\sigma_{\eta\eta}, \sigma_{\zeta\zeta}, \sigma_{\eta\zeta})^T$, and $\underset{\sim}{\varepsilon} = (\varepsilon_{\eta\eta}, \varepsilon_{\zeta\zeta}, \varepsilon_{\eta\zeta})^T$, where (η, ζ, ξ) is a coordinate system embedded in the material or layer with one axis along the fiber direction as shown in Fig. 31.
- Displacement continuity is maintained between layers.

It should be stressed here that no explicit assumptions are made concerning the detailed nature of the various failure processes. Rather, the approach is to introduce a minimal number of hypotheses that we feel are in accordance with physical fact and readily defensible. Moreover, many of the above restrictions can be relaxed when the situation warrants.

5.2 Analysis Overview

The primary issue here is the estimation of the dissipated energy density function $\phi(\underset{\sim}{\varepsilon})$ and the subsequent computation of constitutive behavior. We summarize the steps below and provide more detailed explanations in the remaining subsections.

- A representation is chosen for the dissipation function in terms of a set of m basis functions $\underset{\sim}{\chi} = (\chi_1, \chi_2, \ldots, \chi_m)^T$ and an initially unknown parameter vector $\underset{\sim}{c} = (c_1, c_2, \ldots, c_m)^T$.
- A uniform set of loading paths in displacement space is selected (15 for each material or 15 for each of a set of layup configurations for angle-ply composites), boundary forces and displacements $(\underset{\sim}{t}, \underset{\sim}{u})$ are measured at 50 equally spaced points on each loading path as described in Section 2, and the energy imparted to the specimen, W^p, is computed for each observation point p. If the composite is regarded as a single equivalent homogeneous material (in the case of an angle-ply composite, this implies that each layup configuration is to be counted as a separate material), then this procedure yields n=750 values of W^p per material. If the material is an angle-ply composite and we wish to an-

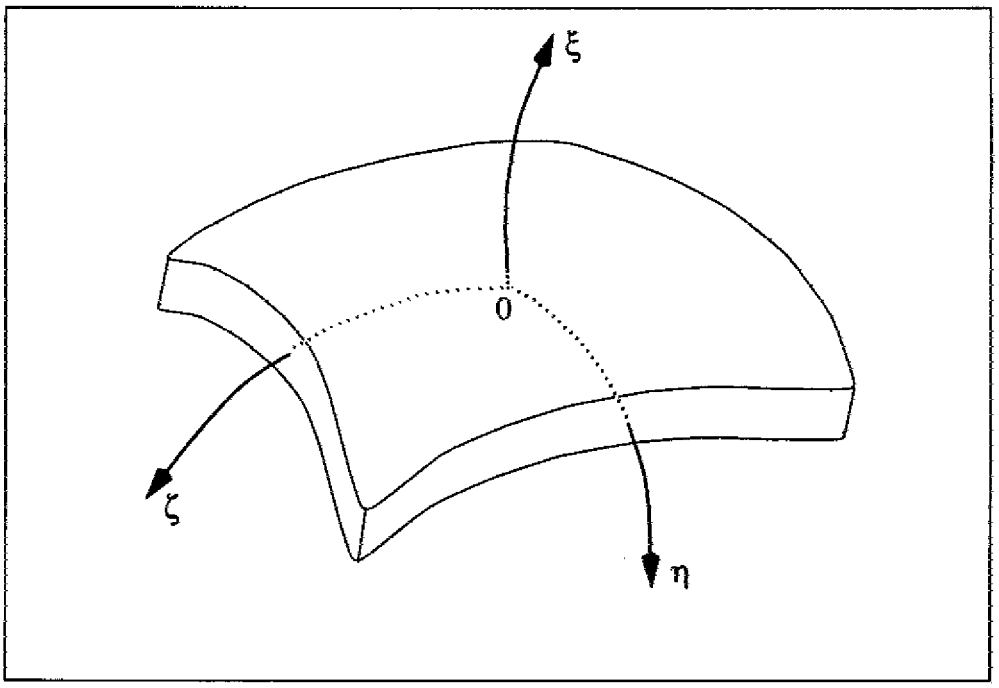

Fig. 31 — Coordinate system embedded in the shell structure

alyze the constitutive behavior on a ply-by-ply basis, then the procedure yields $n = 750 \times np$ values of W^p for each material, where np denotes the number of layup configurations.

- The irreversible portion of the imparted energy, D^p, is computed for each observation point p using the relationship

$$D^p = W^p - \frac{1}{2}(\underline{t}^p \cdot \underline{u}^p) \tag{27}$$

where u^p are the boundary displacements and t^p are the reaction forces.

- The assertion that D^p equals the integral of $\phi(\underline{\varepsilon}(\underline{x}))$ over the volume of the specimen, where $\underline{x} = (\eta, \zeta, \xi)$ is applied at each of the n observation points p and, in conjunction with a representation of the constitutive relation in terms of $\phi(\underline{\varepsilon})$ to be described later, the strain-displacement and equilibrium relations, and any appropriate additional constraints, results in a highly overdetermined set of nonlinear equations for the m components of the parameter vector $\underline{c}$ (a system of $n \times m$ equations with $n \gg m$).
- These equations are solved numerically for $\underline{c}$ and the dissipation density function $\phi(\underline{\varepsilon})$ computed.
- The aforementioned representation of the constitutive relation is used in conjunction with the computed values of $\underline{c}$ to determine the constitutive behavior $\underline{\sigma} = \underline{C}(\underline{\xi}, \underline{\varepsilon})$.

5.3 Representation of the Dissipation Function

The dissipation density function $\phi(\underline{\varepsilon})$ is represented by the linear combination

$$\phi(\underline{\varepsilon}) = \underline{c} \cdot \underline{\chi}(\underline{\varepsilon}) \tag{28}$$

where $\underline{\chi}(\underline{\varepsilon})$ is a vector of suitable C^0 (or smoother basis) functions over the 3-space $(\varepsilon_{\eta\eta}, \varepsilon_{\zeta\zeta}, \varepsilon_{\eta\zeta})$, and $\underline{c}$ the parameter vector to be determined. This representation is quite general in the sense that χ_i may be chosen more or less arbitrarily, for instance, as interpolation basis functions over a suitable mesh defined on $(\varepsilon_{\eta\eta}, \varepsilon_{\zeta\zeta}, \varepsilon_{\eta\zeta})$ in which case any of the usual three-dimensional finite element shape functions may be used; as B-splines or cardinal splines; or as locally defined or global orthogonal polynomials. The only significant restriction on the form of the basis functions is that positivity of the quantity $\phi(\underline{\varepsilon})$ must be assured to maintain agreement with physical observation. When $\underline{\chi}$ is an interpolation basis, the components of the parameter vector $\underline{c}$ are simply the values of ϕ at the node points; however, this is not true when the later two representations for $\underline{\chi}$ are employed. In practice, we almost always chose to use a locally defined linear interpolation basis and this is indeed the situation described in Section 3.

5.4 The Constitutive Relations

In this section we present an overview of the material model and describe in detail a procedure for computing the constitutive behavior in terms of the dissipated energy density function $\phi(\underline{\varepsilon})$.

The basic premise is that the material can be regarded as always being in one of two distinct domains: namely, either purely *elastic* or *inelastic*. When the material is in an elastic domain, no internal damage is presumed to occur; this results in behavior that is load history independent and reversible in the sense that no energy dissipation takes place. The material enters an inelastic domain during loading after a certain strain-dependent threshold is crossed. Here progressive internal damage leads to behavior that is irreversible in nature with energy being dissipated by the various internal damage mechanisms. A restricted type of load path independence, whose precise nature will be discussed shortly, is applicable in this domain.

One way to model this type of behavior is to postulate the existence of a surface $\Gamma(\underset{\sim}{\xi})$ such as $F(\underset{\sim}{\varepsilon}, \underset{\sim}{\xi}) = 0$ in strain space with the following property: namely, that whenever the strain $\underset{\sim}{\varepsilon}$ associated with some material point P is either inside the surface $\Gamma(\underset{\sim}{\xi})$, or outside $\Gamma(\underset{\sim}{\xi})$ with decreasing dissipated energy ($d\phi(\underset{\sim}{\varepsilon})/d|\underset{\sim}{\varepsilon}| < 0$), then P is in an elastic domain. When $\underset{\sim}{\varepsilon}$ is outside of $\Gamma(\underset{\sim}{\xi})$ with increasing dissipated energy ($d\phi(\underset{\sim}{\varepsilon})/d|\underset{\sim}{\varepsilon}| > 0$), P is in an inelastic domain. Here the vector $\underset{\sim}{\xi}$ is a vector of internal state variables that can be thought of as damage parameters and the surface $\Gamma(\underset{\sim}{\xi})$ acts as a threshold that defines the elastic/inelastic transition. The surface $\Gamma(\underset{\sim}{\xi})$ thus plays a role that is loosely analogous to that of the yield surface (in stress space) in classical plasticity theory with the state variables $\underset{\sim}{\xi}$ in the role of strain hardening parameters.

The model we used is based on the above considerations with the additional assumptions that there is only a single scalar state variable ξ that takes on discrete values ξ^j, (j=0,1...), and that the function $F(\underset{\sim}{\varepsilon}, \xi^j)$ in the definition of $\Gamma(\xi^j)$ be identified with level surfaces of the dissipation function $\phi(\underset{\sim}{\varepsilon})$. A state transition takes place each time the material switches from an inelastic to an elastic domain. The state variable ξ^0 is defined by

$$\xi^0 = 0 \tag{29}$$

for material in the initial state, and by

$$\xi^j = \max \phi(\underset{\sim}{\varepsilon}), j = 1,2,... \tag{30}$$

otherwise, where max $\phi(\underset{\sim}{\varepsilon})$ represents the maximum value of energy dissipation encountered in the previous inelastic domain. Also, the function $F(\underset{\sim}{\varepsilon}, \xi^j)$ is taken in the form

$$F(\underset{\sim}{\varepsilon}, \xi^j) = \phi(\underset{\sim}{\varepsilon}) - \xi^j. \tag{31}$$

We assert that the state variable ξ is monotonically increasing, which implies that the threshold surface $\Gamma(\underset{\sim}{\xi})$ always expands in strain space in the sense that the elastic domain interior to the surface $\Gamma(\xi^j)$ must always be included in the elastic domain interior to $\Gamma(\xi^{j+1})$. Also, the parameters that occur in the description of the constitutive behavior in both the elastic and inelastic domains are functions of the state variable ξ^j, thereby implying the existence of a denumerable set of elastic and inelastic domains parametrized by ξ^j alone. This leads to the important conclusion that the only memory the material has of its past is via the state variable ξ^j, which implies a *one parameter* type of history dependence.

Some aspects of the inelastic behavior implied by this model are illustrated in Fig. 32, which shows how the dissipation density function and an arbitrary stress component σ_w vary with $\underset{\sim}{\varepsilon}$ along three arbitrary radial paths in strain space in the two inelastic domains bounded by the surfaces Γ^0 and Γ^1, respectively. Here Γ^j denotes $\Gamma(\xi^j)$ and increasing values of j imply increasing values of the associated state variable ξ^j.

Inelastic Behavior

We examine the inelastic behavior regime first. Let us assume that the work potential $\psi(\underset{\sim}{\varepsilon})$ can be taken as

$$\psi(\underset{\sim}{\varepsilon}) = \Phi(\underset{\sim}{\varepsilon}) + \phi(\underset{\sim}{\varepsilon}) \tag{32}$$

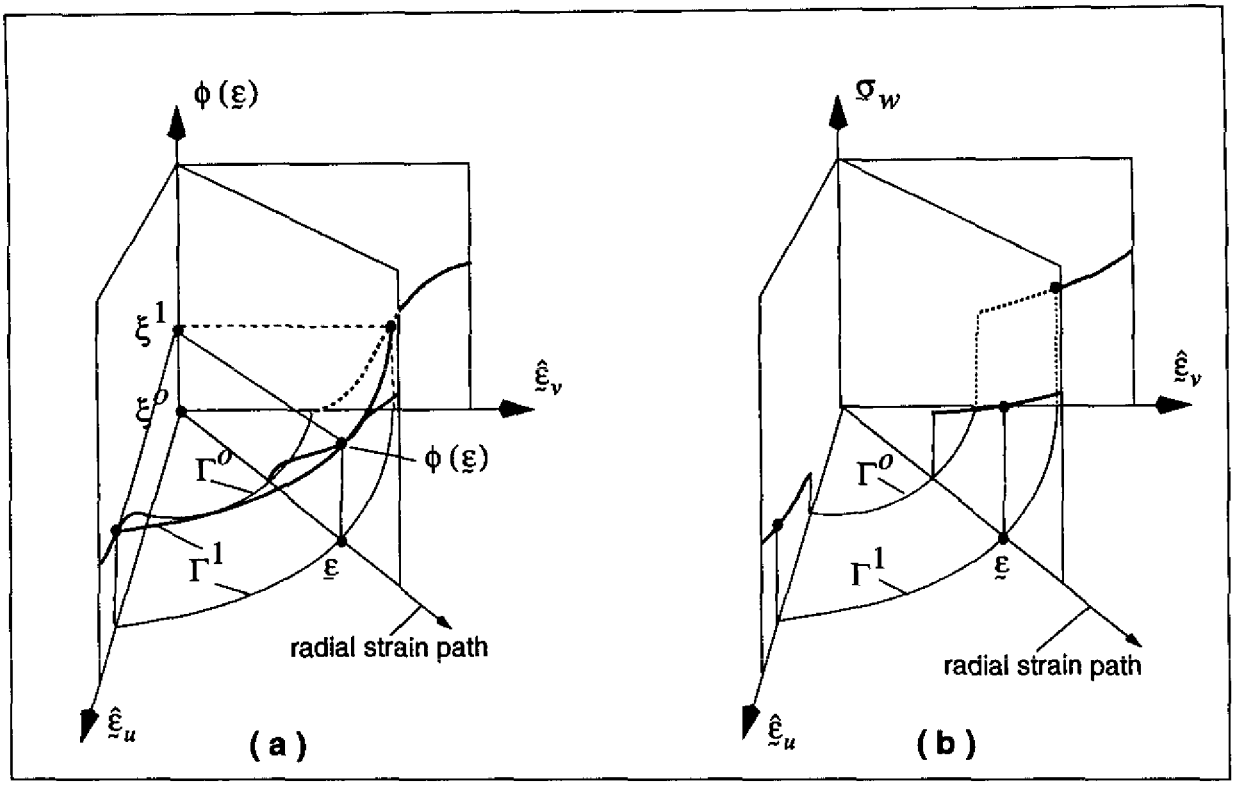

Fig. 32 — Dissipated energy density as a function of (a) strains, and (b) corresponding stress-strain space

where

$$\Phi(\underset{\sim}{\varepsilon}) = \frac{1}{2}(\underset{\sim}{\sigma}(\underset{\sim}{\varepsilon}) \cdot \underset{\sim}{\varepsilon}) \tag{33}$$

We chose this particular form for Eq. (33) because the term $\Phi(\underset{\sim}{\varepsilon})$ is equal to the energy density recovered if the material were to unload linearly from its present state, and, as is shown in this section, is energetically consistent with the postulated elastic unloading behavior. It is obviously not the only choice we could have made, but it is by far the simplest.

Since $\underset{\sim}{\sigma} = \text{grad}_{\underset{\sim}{\varepsilon}} \psi(\xi^j, \underset{\sim}{\varepsilon})$, by definition, taking the gradient of Eq. (32) gives

$$\underset{\sim}{\sigma} = \text{grad}_{\underset{\sim}{\varepsilon}} \Phi(\underset{\sim}{\varepsilon}) + \text{grad}_{\underset{\sim}{\varepsilon}} \varphi(\underset{\sim}{\varepsilon}) \tag{34}$$

Equation (34) is a system of first order linear partial differential equations in $\underset{\sim}{\sigma}(\underset{\sim}{\varepsilon})$ and can be dealt with routinely the method of characteristics (Courant and Hilbert (1962)) when the proper initial conditions are specified on the surface $\Gamma(\xi^j)$; namely,

$$\underset{\sim}{\sigma}(\underset{\sim}{\varepsilon}^{\Gamma'}) = \left[\underset{\sim}{\mathcal{C}}^e(\underset{\sim}{\varepsilon}^{\Gamma'}, (\alpha_1, \alpha_2))\right]. \tag{35}$$

Here (α_1, α_2) are surface coordinates on $\Gamma(\xi^j)$, $\underset{\sim}{\varepsilon}^{\Gamma'} = \underset{\sim}{\varepsilon}^{\Gamma}(\xi^j, \alpha_1, \alpha_2)$ denotes the set of $\underset{\sim}{\varepsilon} \in \Gamma(\xi^j)$ and are regarded as specified, and $\left[\underset{\sim}{\mathcal{C}}^e(\underset{\sim}{\varepsilon}^{\Gamma'}, (\alpha_1, \alpha_2))\right]$ is the known matrix representation of the constitutive relation for the previous elastic domain.

In general we cannot find explicit closed-form expressions for $\underset{\sim}{\sigma}(\underset{\sim}{\varepsilon})$ that satisfy the initial conditions of Eq. (35). There is, however, one such case where such a solution can indeed be found; namely the case where the constitutive relation for the prior elastic domain, i.e., Eq. (35) is linear in $\underset{\sim}{\varepsilon}$, i.e.,

$$\underset{\sim}{\sigma}(\underset{\sim}{\varepsilon}) = \left[\underset{\sim}{\mathcal{C}}^e(\underset{\sim}{\varepsilon}^{\Gamma'}, (\alpha_1, \alpha_2))\right]\underset{\sim}{\varepsilon}, \tag{36}$$

and where the matrix $\left[\underset{\sim}{\mathcal{C}}^e(\underset{\sim}{\varepsilon}^{\Gamma'}, (\alpha_1, \alpha_2))\right]$ is constant over the transition surface $\Gamma(\xi^j)$, i.e., $\left[\underset{\sim}{\mathcal{C}}^e(\underset{\sim}{\varepsilon}^{\Gamma'}, (\alpha_1, \alpha_2))\right] = [\underset{\sim}{\mathcal{C}}^e(\xi^j)]$ on Γ^j. These criteria are certainly met when the elastic domain corresponds to that of the "virgin" material assuming it to be linear and homogeneous in a mechanical sense. Thus, taking the scalar product of Eq. (34) with $\underset{\sim}{\varepsilon}$ and using the definition of $\Phi(\underset{\sim}{\varepsilon})$ decouples the system of Eq. (34) and results in the following *single* first order linear partial differential equation for $\Phi(\underset{\sim}{\varepsilon})$;

$$\underset{\sim}{\varepsilon} \cdot \operatorname{grad}_{\underset{\sim}{\varepsilon}} \Phi - 2\Phi = -(\underset{\sim}{\varepsilon} \cdot \operatorname{grad}_{\underset{\sim}{\varepsilon}} \varphi(\underset{\sim}{\varepsilon})), \tag{37}$$

with initial conditions

$$\Phi(\underset{\sim}{\varepsilon}^{\Gamma'}) = \frac{1}{2}(\underset{\sim}{\varepsilon}^{\Gamma'}(\xi^j, \alpha_1, \alpha_2)\,[\underset{\sim}{\mathcal{C}}^e(\xi^j, \alpha_1, \alpha_2)]\,\underset{\sim}{\varepsilon}^{\Gamma'}(\xi^j, \alpha_1, \alpha_2)). \tag{38}$$

Equation (37) with initial conditions of Eq. (38) again can be solved by means of characteristics to yield the following expression for $\Phi(\underset{\sim}{\varepsilon})$

$$\Phi(\xi^j, \alpha_1, \alpha_2, \beta) = \beta^2\left((\Phi(\underset{\sim}{\varepsilon}^{\Gamma'})) - \int_1^{\beta} \frac{1}{\zeta^2}\frac{d\phi}{d\zeta}d\zeta\right), \tag{39}$$

evaluated on the characteristic lines. The above integral is taken along a characteristic line, that are defined by

$$\underset{\sim}{\varepsilon} = \underset{\sim}{\varepsilon}(\xi^j, \alpha_1, \alpha_2, \beta) = \underset{\sim}{\varepsilon}^{\Gamma'}(\xi^j, \alpha_1, \alpha_2)\,\beta, \tag{40}$$

and where by $\frac{d\phi}{d\zeta}$ we mean

$$\frac{d\phi}{d\zeta} = \frac{d}{d\zeta}\phi(\zeta\underset{\sim}{\varepsilon}^{\Gamma'}(\xi^j, \alpha_1, \alpha_2)). \tag{41}$$

Equation (40) can be regarded as a coordinate transformation relating the coordinates $(\alpha_1, \alpha_2, \beta)$ to $(\varepsilon_1, \varepsilon_2, \varepsilon_3)$. To obtain $\underset{\sim}{\sigma}(\underset{\sim}{\varepsilon})$ we also need the inverse transformation $(\varepsilon_1, \varepsilon_2, \varepsilon_3) \rightarrow (\alpha_1, \alpha_2, \beta)$ and we must be able to evaluate the gradients $\operatorname{grad}_{\underset{\sim}{\varepsilon}}\underset{\sim}{\varepsilon}^{\Gamma'}(\underset{\sim}{\varepsilon})$, $\operatorname{grad}_{\underset{\sim}{\varepsilon}}\beta^2(\underset{\sim}{\varepsilon})$, and $\operatorname{grad}_{\underset{\sim}{\varepsilon}}\underset{\sim}{\alpha}(\underset{\sim}{\varepsilon})$, with $\underset{\sim}{\alpha} = (\alpha_1, \alpha_2)$. A closed-form expression for the inverse can be found when the $\alpha_\gamma\,(\gamma = 1,2)$ are taken as the cosines of the angles that the position vector $|\underset{\sim}{\varepsilon}^{\Gamma'}|$ makes with the ε_γ axes, i.e.,

$$\alpha_\gamma = \frac{\varepsilon_\gamma^{\Gamma'}}{\left|\underset{\sim}{\varepsilon}^{\Gamma'}\right|}. \tag{42}$$

Then using Eq. (40), Eq. (42) becomes

$$\alpha_\gamma = \frac{\varepsilon_\gamma}{|\underset{\sim}{\varepsilon}|}, \tag{43}$$

and from Eq. (40), we get for β:

$$\beta = \frac{|\underset{\sim}{\varepsilon}|}{\left|\underset{\sim}{\varepsilon}^{\Gamma'}\right|}, \tag{44}$$

where the term $\underset{\sim}{\varepsilon}^{\Gamma'}$ in Eq. (44) is now understood to be a function of $\underset{\sim}{\varepsilon}$ whose values are obtained by substituting Eq. (43) into $\underset{\sim}{\varepsilon}^{\Gamma'}(\xi^j, \alpha_1, \alpha_2)$. Equations (43) and (44) therefore define the sought after coordinate transformation $(\varepsilon_1, \varepsilon_2, \varepsilon_3) \rightarrow (\alpha_1, \alpha_2, \beta)$.

The gradients $[\text{grad}_{\underset{\sim}{\varepsilon}} \underset{\sim}{\alpha}(\underset{\sim}{\varepsilon})]$, $\text{grad}_{\underset{\sim}{\varepsilon}} \underset{\sim}{\varepsilon}^{\Gamma'}(\underset{\sim}{\varepsilon})$, and $\text{grad}_{\underset{\sim}{\varepsilon}} \beta^2(\underset{\sim}{\varepsilon})$ are now readily evaluated by using Eqs. (40) and (42) through (44). Thus,

$$\text{grad}_{\underset{\sim}{\varepsilon}} \alpha_\gamma(\underset{\sim}{\varepsilon}) = \frac{1}{|\underset{\sim}{\varepsilon}|}\left(\delta_{i\gamma} - \frac{\varepsilon_i \varepsilon_\gamma}{|\underset{\sim}{\varepsilon}|^2}\right), \tag{45}$$

where

$$\delta_{i\gamma} = \begin{bmatrix} 1 & 0 \\ 0 & 1 \\ 0 & 0 \end{bmatrix}, \tag{46}$$

$$\left[\text{grad}_{\underset{\sim}{\varepsilon}} \underset{\sim}{\varepsilon}^{\Gamma'}(\underset{\sim}{\varepsilon})\right] = \left[\text{grad}_{\underset{\sim}{\alpha}} \underset{\sim}{\varepsilon}^{\Gamma'}(\underset{\sim}{\varepsilon})\right]\left[\text{grad}_{\underset{\sim}{\varepsilon}} \underset{\sim}{\alpha}(\underset{\sim}{\varepsilon})\right], \tag{47}$$

where $\left[\text{grad}_{\underset{\sim}{\alpha}} \underset{\sim}{\varepsilon}^{\Gamma'}(\underset{\sim}{\varepsilon})\right] = \left[\text{grad}_{\underset{\sim}{\alpha}} \underset{\sim}{\varepsilon}^{\Gamma'}(\underset{\sim}{\alpha})\right]\Big|_{\underset{\sim}{\alpha} = \underset{\sim}{\alpha}(\underset{\sim}{\varepsilon})}$ is known since the transition surface is already determined, and

$$\text{grad}_{\underset{\sim}{\varepsilon}} \beta^2(\underset{\sim}{\varepsilon}) = \left(\frac{2}{\left|\underset{\sim}{\varepsilon}^{\Gamma'}\right|^2}\left(\mathbf{I} - \beta\left[\text{grad}_{\underset{\sim}{\varepsilon}} \underset{\sim}{\varepsilon}^{\Gamma'}(\underset{\sim}{\varepsilon})\right]^T\right)\right)\underset{\sim}{\varepsilon}, \tag{48}$$

where $\mathbf{I}$ is the identity matrix.

The stress field $\underset{\sim}{\sigma}(\underset{\sim}{\varepsilon})$ can now be obtained by substituting the expression for $\Phi(\xi, \alpha_1, \alpha_2, \beta)$ in Eq. (39) into Eq. (34) and using the relationships between $\underset{\sim}{\varepsilon}$ and $(\xi, \alpha_1, \alpha_2, \beta)$ as given in Eq. (40). Thus $\underset{\sim}{\sigma}(\underset{\sim}{\varepsilon})$ is given by

$$\underline{\sigma} = \left([\underline{C}^e] + \frac{2}{|\underline{\varepsilon}^{\Gamma'}|^2} (\mathbf{I} - \beta \left[\text{grad}_{\underline{\varepsilon}} \underline{\varepsilon}^{\Gamma'}(\underline{\varepsilon}) \right]^T) \int_1^\beta \frac{1}{\zeta^2} \frac{d\phi}{d\zeta} d\zeta \right) \underline{\varepsilon}$$
$$-\beta^2 \int_1^\beta \frac{1}{\zeta^2} \left[\text{grad}_{\varepsilon} \underline{\varepsilon}^{\Gamma'}(\underline{\varepsilon}) \right] \text{grad}_{\underline{\alpha}} \left(\frac{d\phi}{d\zeta} \right) d\zeta \tag{49}$$

Elastic behavior

In the elastic regime we assume that the material can be modeled as a particular type of nonlinear hyperelastic material; namely one that allows for no initial stresses and has linear stress-strain behavior along *radial* paths in strain space. This later assumption was invoked to maintain energetic consistency with the representation for ψ in Eq. (32) so that the energy available for elastic unloading is always given by $\Phi(\underline{\varepsilon})$. This assumption also agrees with repeated observations of linear unloading behavior during the IPL tests.

The type of behavior we are attempting to model is illustrated in Fig. 33 where the linear behavior along radial paths is shown for two elastic domains with associated transition surfaces Γ^0 and Γ^1 (Fig. 33 (a) and (b), respectively). The important point to note here is that the elastic constitutive behavior is generally nonlinear; it is only guaranteed to be linear along the radial paths mentioned above. Also note that the

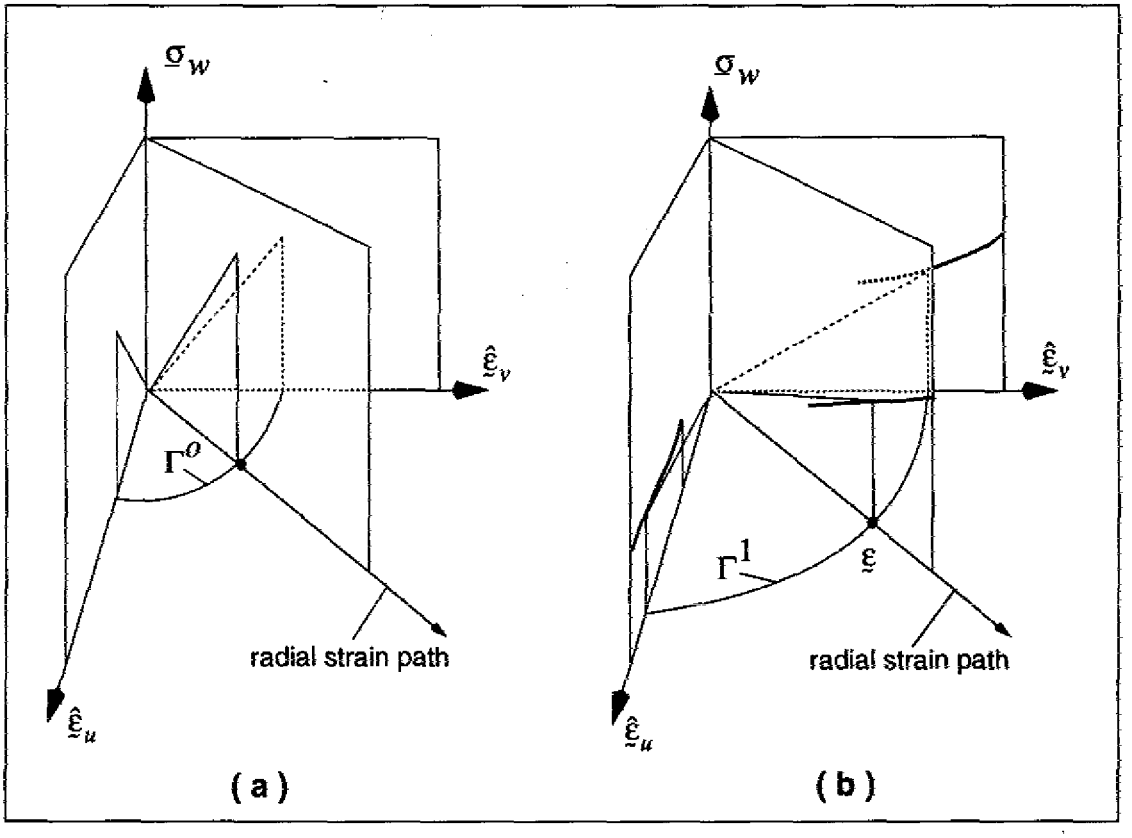

Fig. 33 — Stress-strain behavior for state Γ^0 (a) and state Γ^1 (b)

effective elastic stiffness is expected to decrease with increasing values of the state variable ξ^j, which in turn correspond to increasing values of energy dissipation as illustrated in the Fig. 33.

Consistent with the above assumptions, we propose a constitutive relation in the elastic domain having the form

$$\underset{\sim}{\sigma} = (\underset{\sim}{C}^e(\xi, \alpha_1, \alpha_2))\,|\underset{\sim}{\varepsilon}|, \tag{50}$$

where $\underset{\sim}{C}^e$ is now taken to be a *vector* rather than a matrix. Equation (50) has a deceptively simple form; however it is really quite general and easily subsumes the usual linear form

$$\underset{\sim}{\sigma} = [\underline{A}]\,\underset{\sim}{\varepsilon}. \tag{51}$$

That this is indeed the case is readily demonstrated since $\underset{\sim}{\varepsilon}$ can always be written as $\underset{\sim}{\varepsilon} = \hat{\underset{\sim}{\varepsilon}}(\alpha_1, \alpha_2)\,|\underset{\sim}{\varepsilon}|$ along some path with $\hat{\underset{\sim}{\varepsilon}}$ being the associated unit vector. Therefore Eq. (51) assumes the form of Eq. (50) with $\underset{\sim}{C}^e$ given as

$$\underset{\sim}{C}^e(\alpha_1, \alpha_2) = [\underline{A}]\,\hat{\underset{\sim}{\varepsilon}}(\alpha_1, \alpha_2). \tag{52}$$

For the initial state ξ_0, the constitutive behavior is assumed to be given by the equivalent form of Eq. (51) with the matrix $\underline{A}$ computed using the "virgin" material properties. For subsequent states ξ_i, $i = 1, 2, \ldots$, Eq. (50) is used where stress continuity across the surface Γ^j leads to the following expression for the vector $\underset{\sim}{C}^e(\xi^j, \underset{\sim}{\varepsilon})$

$$\underset{\sim}{C}^e(\xi^{j+1}, \underset{\sim}{\varepsilon}) = \frac{\underset{\sim}{\sigma}(\underset{\sim}{\varepsilon}^{\Gamma^j})}{|\underset{\sim}{\varepsilon}^{\Gamma^j}|}, \tag{53}$$

where $\underset{\sim}{\sigma}(\underset{\sim}{\varepsilon}^{\Gamma^j})$ is computed by evaluating the stresses given by Eq. (44) on the surface Γ^j.

We stress that Eq. (51) with $\underset{\sim}{C}^e$ given by Eq. (53) usually results in elastic constitutive behavior that is inherently nonlinear because $\underset{\sim}{C}^e_s(\xi, \underset{\sim}{\varepsilon})$ is generally not of the form given in Eq. (52).

5.5 Equations for the Determination of the Parameter Vector

The irreversible portion R^i of the total energy imparted to the specimen via the boundary loads at every observation point i in an IPL test series for a given material can be computed by numerical integration since all tractions $\underset{\sim}{t}$ and applied boundary displacements $\underset{\sim}{u}$ required for the computations were previously measured and stored. Thus, R^i is given by

$$R^i = \int_0^{\underset{\sim}{u}^i} \underset{\sim}{t} \cdot d\underset{\sim}{u} - \frac{1}{2}(\underset{\sim}{t}^i \cdot \underset{\sim}{u}^i) \tag{54}$$

where $i = 1,\ldots,n$. On the other hand, the energy absorbed by the specimen is by linear additivity

$$\Phi^i = \int_{vol} \varphi(\underset{\sim}{\varepsilon}(\underset{\sim}{x}))\,d\underset{\sim}{x} = c_j \int_{vol} \chi_j(\underset{\sim}{\varepsilon}^i(\underset{\sim}{c}, \underset{\sim}{x}))\,d\underset{\sim}{x}, \tag{55}$$

where the volume integration is to be taken in a Stieltjes sense over the plies. When doing ply-level analyses of angle-ply materials, we have used the representation given by Eq. (28), and the Einstein summation convention is in effect. But Φ^i must equal R^i by energy conservation, therefore

$$R^i = c_j \int_{vol} \chi_j (\underline{\varepsilon}^i (\underline{c}, \underline{x})) \, d\underline{x} . \tag{56}$$

The quantity $\underline{\varepsilon}^i (\underline{c}, \underline{x})$ that appears in Eq. (55) is the specimen strain field corresponding to the i^{th} observation and is not known explicitly; however, it must satisfy the constitutive relation as given by Eq. (49) as well as the equilibrium and strain-displacement equations, i.e.

$$\operatorname{div} \underline{\sigma}^i = 0, \tag{57}$$

and

$$\underline{\varepsilon}^i = \operatorname{sym} (\operatorname{grad} \underline{u}^i) . \tag{58}$$

The appropriate boundary conditions are free surface conditions (no tractions) except on the gripped surfaces where displacements are prescribed. Equations (54) through (58) form a coupled system of nonlinear equations whose solution places restrictions on the quantities $(\underline{c}, \underline{\varepsilon}, \underline{\sigma}, \underline{u})$.

5.6 Method of Solution

The nature of the system of Eqs. (54) through (58) suggests solution by the following iterative procedure:

1. An initial estimate of the strain field, i.e., $\underline{\varepsilon}^{i0} (\underline{x})$ is obtained by solving Eqs. (57) and (58) using the constitutive relation

$$\underline{\sigma} = [\underline{C}^0] \underline{\varepsilon} \tag{59}$$

where $[\underline{C}^0]$ is the stiffness matrix for the unstressed material and can either be obtained from the literature (when available) or estimated from mixture theory. The problem defined here is linear and is readily solved by finite element methods, or, in certain cases, by closed-form procedures (Muskhelishvili (1953), Mast (1973a,73b)).

2. Using $\underline{\varepsilon}^{i0} (\underline{x})$ as the estimate for $\underline{\varepsilon}^i (\underline{\alpha}, \underline{x})$, an estimate of the parameter vector $\underline{c}$ is obtained from Eq. (56) subject to the constraints that each component of the imparted energy be monotonically increasing along every loading path. This involves solving a linear or quadratic programming problem as explained in Section 5.7.

3. Equations (57), (58), and (49) are solved numerically with the value of $\underline{c}$ in the representation for ϕ (Eq. (28)) taken as $\underline{c}^0$; the new estimate of $\underline{\varepsilon}$ is utilized in Eq. (56) to obtain an updated estimate of $\underline{c}$; and the process is repeated until successive estimates differ by (hopefully) a sufficiently small amount.

Note that except for the initial step, determining the estimate of $\underline{\varepsilon}^i (\underline{c}, \underline{x})$ always involves solving a set of *nonlinear* boundary value problems. Although this is in general difficult and time consuming, as a practical matter, unless one is interested in venturing deeply into the nonlinear regime where significant strain redistribution occurs due to spatially widespread material stiffness changes, sufficient accuracy should be attainable by implementing only a single cycle of the iteration procedure. Thus, we usually need only to solve the *linear* problem described in Item 1 above, and the difficulties mentioned above should be of little

concern. If the need does arise to implement more than one cycle of the iteration procedure, techniques such as homotopic continuation methods (Watson (1986)) applied along each loading path are available to help alleviate the difficulties.

5.7 Initial Estimates of the Parameter Vectors

As mentioned previously, $\underset{\sim}{\varepsilon}^{i0}(\underset{\sim}{x})$ is computed by solving a *linear* boundary value problem. Indeed, using the fact that any boundary displacement $\underset{\sim}{u}$ produced by the IPL can be represented by a linear combination of opening/closing (u_1), sliding (u_0), and rotating (u_2) displacements, only three finite element analyses need be performed in this step since any strain field $\underset{\sim}{\varepsilon}^{i0}(\underset{\sim}{x})$ can be represented as

$$\underset{\sim}{\varepsilon}^{i0} = \sum_k \underset{\sim}{\varepsilon}^{i0k} \tag{60}$$

by linear superposition, where $\underset{\sim}{\varepsilon}^{i0k}(\underset{\sim}{x})$ are the strain fields corresponding to unit boundary displacements in the k^{th} direction.

With $\underset{\sim}{\varepsilon}^{i0}(\underset{\sim}{x})$ known, the quantity $\int_{vol}\chi_j(\underset{\sim}{\varepsilon}^{i0}(\underset{\sim}{x}))\,d\underset{\sim}{x}$ in Eq. (56) may be computed. Thus, setting

$$\int_{vol}\chi_j(\underset{\sim}{\varepsilon}^{i0}(\underset{\sim}{x}))\,d\underset{\sim}{x} \equiv F_{ij}, \tag{61}$$

Eq. (56) may be written as the *linear* set of equations

$$[\underset{\sim}{F}]\,\underset{\sim}{z} = \underset{\sim}{W}, \tag{62}$$

where $\underset{\sim}{W} \equiv (R^1, \ldots, R^n)^T$; $\underset{\sim}{z} \equiv \underset{\sim}{c}^0$, and

$$[\underset{\sim}{F}] = \begin{bmatrix} F_{11} & \cdots & F_{1m} \\ \cdots & \cdots & \cdots \\ F_{n1} & \cdots & F_{nm} \end{bmatrix}, \tag{63}$$

as long as rank ($[\underset{\sim}{F}]$) < rank ($[\underset{\sim}{\bar{F}}]$) , where $[\underset{\sim}{\bar{F}}]$ is the augmented matrix

$$\begin{bmatrix} F_{11} & \cdots & F_{1m} & W_1 \\ \cdots & \cdots & \cdots & \cdots \\ F_{n1} & \cdots & F_{nm} & W_m \end{bmatrix}. \tag{64}$$

Equation (62) is an overdetermined system and there exists no value of $\underset{\sim}{z}$ that satisfies it exactly. Rather, one must seek to minimize the norm of the error vector $\underset{\sim}{e} = (\underset{\sim}{W} - [\underset{\sim}{F}]\,\underset{\sim}{z})$ to obtain a best approximation to the solution. This is the usual state of affairs in parameter estimation; indeed, the more highly overdetermined the system, the better the situation since one generally wants to work with as many independent observations as possible to filter out any undesirable stochastic variations (noise). Only if enough observations are linearly dependent can it happen that rank ($[\underset{\sim}{F}]$) = rank ($[\underset{\sim}{\bar{F}}]$) < m, in which case there exists n − rank ($[\underset{\sim}{F}]$) solutions to Eq. (62). This situation should not arise if the experimental testing program is well thought out.

Assuming for the moment that Eq. (62)(62) is indeed overdetermined, we seek to minimize the norm of $\underset{\sim}{e} = \underset{\sim}{W} - [\underset{\sim}{F}]\,\underset{\sim}{z}$ subject to the constraints that

- the values of φ are positive at the node points of the interpolation mesh, i.e.,

$$z^i > 0, \tag{65}$$

to maintain positivity,

- the dissipated energy is monotonically increasing along each radial loading path in displacement space, i.e.,

$$\text{row}\,([\underset{\sim}{F}])_{i_p} \cdot \underset{\sim}{z} > 0$$

$$(\text{row}\,([\underset{\sim}{F}])_{i+1} - \text{row}\,([\underset{\sim}{F}])_i) \cdot \underset{\sim}{z} \geq 0,\ i = i_p, \ldots, i_q - 1 \tag{66}$$

where Eq. (66) applies to each loading path, i_p is a point at the beginning of the path, and i_q is the end point.

Note that the above constraints are *linear* inequality constraints in $\underset{\sim}{z}$, and as such are readily dealt with. Two widely used measures of vector magnitude are the L^2 (Euclidean) and L^∞ (Chebychev) norms given by

$$\|\underset{\sim}{x}\|_{L^2}^2 = (x_1^2 + x_2^2 + \ldots + x_n^2)^2, \tag{67}$$

and

$$\|\underset{\sim}{x}\|_{L^\infty} = \max_{x_i}(|x_1|, |x_2|, \ldots, |x_n|) \tag{68}$$

respectively. Minimizing $\|\underset{\sim}{e}\|$ in Eq. (62) under the L^2 norm subject to the constraints of Eqs. (65) and (66) is a problem in *quadratic programming* since the objective function $\|\underset{\sim}{W} - [\underset{\sim}{F}]\,\underset{\sim}{z}\|_{L^2}$ is quadratic in the variables $(z_1, z_2, \ldots, z_n)$. This is a well-established discipline and many efficient procedures are available to deal with such problems. Minimizing $|\underset{\sim}{e}|$ under the L^∞ norm is just as straightforward, and perhaps easier, because there exists a well-known technique due to Lagrange for converting such problems into *linear programming* problems that can be solved using the simplex method or one of its variants. A highly readable discussion of these optimization issues is presented by Gill Murray, and Wright, (1981).

ACKNOWLEDGMENTS

We wish to acknowledge past and current financial support of the following Navy organizations and the indicated program managers:

Office of Naval Technology (J.J. Kelly* and I.L. Caplan* [DTRC Block Manager])
Strategic Systems Project Office (E.L. Throckmorton*, R. Kinert, and F. Vondersmith)
Naval Air Systems Command (C.F. Bersch)
Naval Sea Systems Command (H.H. Vanderveldt, C. Zanis, W.R. Graner, and T.F. White).

We also wish to acknowledge helpful technical discussions with H. Marshall, Lockheed Palo Alto Research Laboratory, and J. Pitman, Gibbs and Cox Inc.

* Current Program Managers.

REFERENCES

D.H. Allen, C.E. Harris, and S.E. Groves "A thermomechanical constitutive theory for elastic composites with distributed damage-i and ii," *Int. J. Solids Structures*, **23**, 301 (1987).

J. Aveston and A. Kelly, "Theory of multiple fracture of fibrous composites," *J. Material Science*, **8**, 352 (1973).

J. Aveston and A. Kelly, *Int. J. Solids Structures* **23**, 301 (1987).

R. Badaliance and H. D. Hill, "Damage mechanisms and life prediction of graphite/epoxy composites," in STP775 Damage in Composite Materials, K. L. Reifsnider, ed. , 1982, ASTM, Philadelphia, PA., 1982, pp. 229-242.

Z.P. Bazant, "Mechanics of distributed cracking," *Appl. Mech. Rev.*, **39**, 675 (1986).

B.A. Bilby, R. Bullough, and E. Smith, "Continuous distributions of dislocations: a new application of the methods of non-riemannian geometry," *Proc. R. Soc. London A*, **231**, 263 (1955).

R. Courant and D. Hilbert, *Methods of Mathematical Physics*, Vol. II (Wiley-Interscience, New York, 1962).

O.W. Dillon, Jr. and J. Kratochvil, "Thermodynamics of elastic-plastic materials as a theory with internal state variables," *J. Appl. Physics*, **40**, 3207 (1969).

G.J. Dvorak and W.S. Johnson, "Fatigue of metal matrix composites," *Int. J. Fracture*, **16**, 585 (1980).

P. E. Gill, W. Murray, and M. H. Wright, "Practical Optimization," (Academic Press, London, 1981).

A. Highsmith and K.L. Reifsnider, "Stiffness-Reduction Mechanisms in Composite Laminates, in STP775 Damage in Composite Materials, K. L. Reifsnider, ed., 1982, ASTM, Philadelphia, PA., 1982, p. 103.

L.M. Kachanov, "On the creep fracture time," Izv. AN SSR, Otd. Tekhm. Nauk, 8, 26 (1958).

L.M. Kachanov, *Introduction to Continuum Damage Mechanics* (Martinus Nijhoff, Dordrecht, 1986).

D. Krajcinovic, "Continuum damage mechanics," *Appl. Mech. Rev.*, **37**, 1 (1984).

D. Krajcinovic, "Update to continuum damage mechanics," *Appl. Mech. Update*, **LW3** (1986).

M.J. Lamborn and R.A. Schapery, "An investigation of deformation path-independence of mechanical work in fiber-reinforced plastics," in Proc. Fourth Japan-U.S. Conference on Composite Materials, 1988, Technomic, Washington D.C., 1988, pp. 991-1000.

J. Lemaitre, "Formulation and Identification of Damage Kinetic Constitutive Equations," in *CISM Courses and Lectures No. 295* (Springer-Verlag, Wien, 1987) p. 37.

P.W. Mast, "Tensor Manipulations in Complex Coordinated with Applications to the Mechanics of Materials", Naval Reserch Laboratory Report 7537, NRL Wahington D.C., May 1973.

P.W. Mast, "Solution Graphs: Simple Algebraic Structures for Problems in Linear Anisotropic Elasticity," NRL Report 7577, September 1973.

P.W. Mast, L.A. Beaubien, D.R. Mulville, S.A. Sutton, R.W. Thomas, J. Tirosh, and I. Wolock, "Failure Criteria for Composite Structures in High Performance Composites and Adhesives for V/STOL Aircraft," C.F. Poranski ed., NRL Memorandum Report 5231, Washington D.C. , 1984, pp. 59-90.

P.W. Mast, L.A. Beaubien, M. Clifford, D.R. Mulvile, S.A. Sutton, R.W. Thomas, J. Tirosh, and I. Wolock, "A semi-automated in-plane loader for material testing," *Experimental Mechanics*, **23**(2), 236-241 (1983).

J.E. Masters and K.L. Reifsnider, "An investigation of cumulative damage development in quasi-isotropic graphite/epoxy," in STP775 Damage in Composite Materials, K. L. Reifsnider, ed., 1982, Philadelphia, PA., ASTM, 1982, pp. 40-62.

J.G. Michopoulos, G.C. Sih, S.C. Chou, and J.F. Dignam, "Energy dissipation in highly compressed cylindrical bar specimens," *J. Theoret. and Appl. Fracture Mech.*, **2**(2), 105-110 (1984).

J.G. Michopoulos, G.C. Sih, and D.Y. Tzou, "Secondary temperature fluctuation in cracked 1020 steel specimen loaded monotonically," *J. Theoret. and Appl. Fracture Mech.*, **7**(2), 74-87 (1987).

G.E. Morris and C.M. Hetter, "Fractographic studies of graphite/epoxy fatigue specimens," in STP775 Damage in Composite Materials, K. L. Reifsnider, ed., 1982, Philadelphia, PA., 1982, ASTM, pp. 27-39.

N.I. Muskhelishvili, *Some Basic Problems of the Mathematical Theory of Elasticity*, (P. Noordhoff, Groningen Holland, 1953).

Naval Sea Systems Command, *Design Data Sheet 170-0*, (DoD Naval Sea Systems Command, March 1982).

E.T. Onat and F.A. Leckie, "Representation of mechanical behavior in the presence of changing internal structure," *J. Appl. Mech.*, **55**, 1 (1988).

K.L. Reifsnider and W.W. Stinchcomb, "Fatigue damage mechanisms in composite materials: A review," in Symposium on Basic Mechanisms of Fatigue, ASTM, 1978, Kansas City, Missouri, 1978.

K.L. Reifsnider, "Fatigue behavior of composite materials," *Int. J. Fracture*, **16**, 563 (1980).

R.A. Schapery, "Deformation and fracture characterization of inelastic composite materials using potentials," *Polymer Eng. and Scie.*, **27**(1), 63-76 (1987).

R.A. Schapery, "Mechanical Characterization and Analysis of Inelastic Composite Laminates with Growing Damage," in Mechanics of Composite Materials, ASME AMD, Number 2, 1989, pp. 1-9.

R.A. Schapery, "A method for mechanical state characterization of inelastic composite laminates with damage," in Advances in Fracture Research, Proc. Seventh Int. Conf. Fracture, Vol. 3, 1989, pp. 2177-2189.

R.A. Schapery, "A theory of mechanical behavior of elastic media with growing damage and other changes in structure," *J. Mech. Phys. Solids*, **38**(2), 215-253 (1990).

G.C. Sih, D.Y. Tzou, and J.G. Michopoulos, "Secondary Temperature Fluctuation in Cracked 1020 Steel Specimen Loaded Monotonically," *J. Theoret. and Appl. Fracture Mech.*, **7**(2), 74-87 (1987).

G.C. Sih, "Thermal/Mechanical Interaction Associated with the Micromechanisms of Material Behavior," Institute of Fracture and Solid Mechanics, Lehigh University, Bethlehem, PA, 1987.

R. Talreja, *Fatigue of Composite Materials* (Technomic, Lancaster, PA, 1987).

S.W. Tsai and H.T. Hahn, "On the behavior of composite laminates after initial failures," *J. Composite Materials*, **8**, 288 (1974).

L.T. Watson, "Numerical linear algebra aspects of globally convergent homotopy methods," *SIAM Review*, **28**(4), 529-545 (1986).

Appendix A
Materials Data Base Description

ITEM	RESIN	FIBER	LAYUP	SUPPLIER	FILE	PROJECT
		Material System AS1/3501-6 (Thermoset)				
001	3501-6	AS1	+/- 15	Hercules	mt-1	NAV-SEA
002	.	.	+/- 30	.	mt-2	.
003	.	.	+/- 60		mt-3	.
004	.	.	+/-75	.	mt-4	.
		Material System AS4/3501-6 (Thermoset)				
005	.	AS4	+/-15	.	mt-5	.
006	.	.	+/-30	.	mt-6	.
007	.	.	+/- 60	.	mt-7	.
008	.	.	+/-75	.	mt-8	.
		Material System AS6/3501-6 (Thermoset)				
009	.	AS6	+/-15	.	mt-9	.
010	.	.	+/-30	.	mt-10	.
011	.	.	+/-60	.	mt-11	.
012	.	.	+/-75	.	mt-12	.
		Material System IM6/3501-6 (Thermoset)				
013	.	IM6	+/-15	.	mt-13	.
014	.	.	+/-30	.	mt-14	.
015	.	.	+/-60	.	mt-15	.
016	.	.	+/-75	.	mt-16	.
		Material System IM7/3501-6 (Thermoset)				
017	.	IM7	+/-15	.	mt-17	.
018	.	.	+/-30	.	mt-18	.
019	.	.	+/-60	.	mt-19	.
020	.	.	+/-75	.	mt-20	.

ITEM	RESIN	FIBER	LAYUP	SUPPLIER	FILE	PROJECT
			Material System HMS4/3501-6 (Thermoset)			
021	3501-6	HMS4	+/-15	Hercules	mt-21	.
022	.	.	+/-30	.	mt-22	.
023	.	.	+/-60	.	mt-23	.
024	.	.	+/-75	.	mt-24	.
			Material System HS 12000/5245 (Thermoset)			
025	5245	HS 12000	+/-15	Celanese	mt-25	.
026	.	.	+/-75	.	mt-26	.
			Material System HS 12000/5208 (Thermoset)			
027	5208	.	+/-15	.	mt-27	.
028	.	.	+/-75	.	mt-28	.
			Material System 6000/5208 (Thermoset)			
029	.	CELION 6000	+/- 15	.	mt-29	.
030	.	.	+/-75	.	mt-30	.
			Material System AS4W/3501-6 (Thermoset)			
031	3501-6	AS4W	0,90,0%z	FMI	mt-31	.
032	.	.	0,90,5%z	.	mt-32	.
033	.	.	0,90,13%z	.	mt-33	.
			Material System IM6/PEEK (Thermoplastic)			
034	PEEK	IM6	+/-15	ICI	mt-34	.
035	.	.	+/-30	.	mt-35	.
036	.	.	+/-60	.	mt-36	.
037	.	.	+/-75	.	mt-37	.
			Material System AS4/PEEK (Thermoplastic)			
038	.	AS4	+/-15	.	mt-38	.
039	.	.	+/-30	.	mt-39	.
040	.	.	+/- 60	.	mt-40	.
041	.	.	+/-75	.	mt-41	.

ITEM	RESIN	FIBER	LAYUP	SUPPLIER	FILE	PROJECT
			Material System E-glass/Epoxy (Thermoset)			
042	Epoxy	E-glass	Cloth	Fiberite	mt-42	.
043	.	.	.	Magnaweave	mt-43	.
044	.	.	.	.	mt-44	.
			Material System B238/Polyester (Thermoset)			
045	Polyester	B238	0,90	Proform Fab.	mt-45	.
046	.	.	$((0,90)(+/-45))_2$	.	mt-46	.
047	.	.	$(0,90)(+/-45)_2(0,90)$	.	mt-47	.
048	.	.	$(+/-45)_4$	.	mt-48	.
			Material System CDB340/Polyester (Thermoset)			
049	.	CDB340	(0,+/-45)	.	mt-49	.
050	.	.	(+/-45,90)	.	mt-50	.
			Material System DB170/Polyester (Thermoset)			
051	.	DB170	$(0,90)_5$	.	mt-51	.
052	.	.	$(+/-45,0,90)_2$	.	mt-52	.
053	.	.	$(0,90)(+/-45)_3(0,90)$	.	mt-53	.
054	.	.	$(+/-45)_5$	.	mt-54	.
			Material System Quartz/Polybutadiene (Thermoplastic)			
055	Polybutadiene	Quartz	+/-0	Brunswick	mt-55	RAS
056	.	.	+/-15	.	mt-56	.
057	.	.	+/-30	.	mt-57	.
058	.	.	+/- 45	.	mt-58	.
059	.	.	+/-60	.	mt-59	.
060	.	.	+/-75	.	mt-60	.
061	.	.	+/-90	.	mt-61	.

ITEM	RESIN	FIBER	LAYUP	SUPPLIER	FILE	PROJECT
Material System Quartz/Polybutadiene 5% Powder Carbon (Thermoplastic)						
062	Polybutadiene,5%C,	Quartz	+/-0	Brunswick	mt-62	.
063	.	.	+/-15	.	mt-63	.
064	.	.	+/-30	.	mt-64	.
065	.	.	+/-45	.	mt-65	.
066	.	.	+/-60	.	mt-66	.
067	.	.	+/-75	.	mt-100	.
068	.	.	+/-90	.	mt-101	.
Material System IM7/HBRF-55A (Thermoset)						
069	HBRF-55A	IM7	+/-22	Hercules	mt-70	SP
070	.	.	+/-35	.	mt-71	.
071	.	.	+/-55	.	mt-72	.
072	.	.	+/-68	.	mt-73	.
073	.	.	(+/-22,90)	.	mt-74	.
074	.	.	(+/-68,0)	.	mt-75	.
Material System IM7/HBRF-55A (Thermoset)						
075	HBRF-55A	IM7	+/-22	.	mt-102	.
076	.	.	(-55,+35,-35,+35)	.	mt-103	.
077	.	.	(+35,-55,+55,-55)	.	mt-104	.
078	.	.	+/-68	.	mt-105	.
079	.	.	(90,+/-22)	.	mt-106	.
080	.	.	(0,+/-68)	.	mt-107	.
Material System Kevlar/Polyether-Sulfone (Thermoplastic)						
081	Polyether-Sulfone	Kevlar 49	Fabric	ICI	mt-108	Chem.
Material System TORAY 300/Polyether-Sulfone (Thermoplastic)						
082	.	TORAY 300	.	.	mt-109	.
Material System E-glass/Polyether-Sulfone (Thermoplastic)						
083	.	E-glass	.	.	mt-110	.
Material System Graphite A004/Epikot 828 (Thermoset)						
084	Epikote 828	A004	(0,90,90/0)	TTCP	mt-111	TTCP
Material System S-2 glass/Shell 828(Thermoset)						
085	Shell 828	S-2 glass	$(0,90)_5$	.	mt-112	.

ITEM	RESIN	FIBER	LAYUP	SUPPLIER	FILE	PROJECT
Material System RYTON PPS/GRAPHITE (AC 40-66) (Thermoset)						
086	Ryton PPS	graphite	+/-15	Phillips	mt-113	Boeing
087	.	.	+/-30	.	mt-114	.
088	.	.	+/-60	.	mt-115	.
089	.	.	+/-75	.	mt-116	.
Material System IM7/HBRF-55A (Thermoset)						
090	HBRF-55A	IM7	+/-22	Hercules	mt-117	SP-D5
091	.	.	+/-35	.	mt-118	.
092	.	.	+/-55	.	mt-119	.
093	.	.	+/-68	.	mt-120	.
094	.	.	(+/-22,90)	.	mt-121	.
095	.	.	(+/-68,0)	.	mt-122	
Material System AS4/PEEK (APC-2) (Thermoplastic)						
096	PEEK	AS4	+/-15	.	mt-123	.
097	.	.	+/-30	.	mt-124	.
098	.	.	+/-45	.	mt-125	.
099	.	.	+/-60	.	mt-126	.
100	.	.	+/-75	.	mt-127	.
101	.	.	(0,90)	.	mt-128	.

Appendix B
The In-Plane Loader System

The IPLS, shown schematically in Fig. B1, is an automated testing facility whose primary function is to produce reliable data from which the energy dissipation function can be deduced with a minimum of ancillary hypotheses.

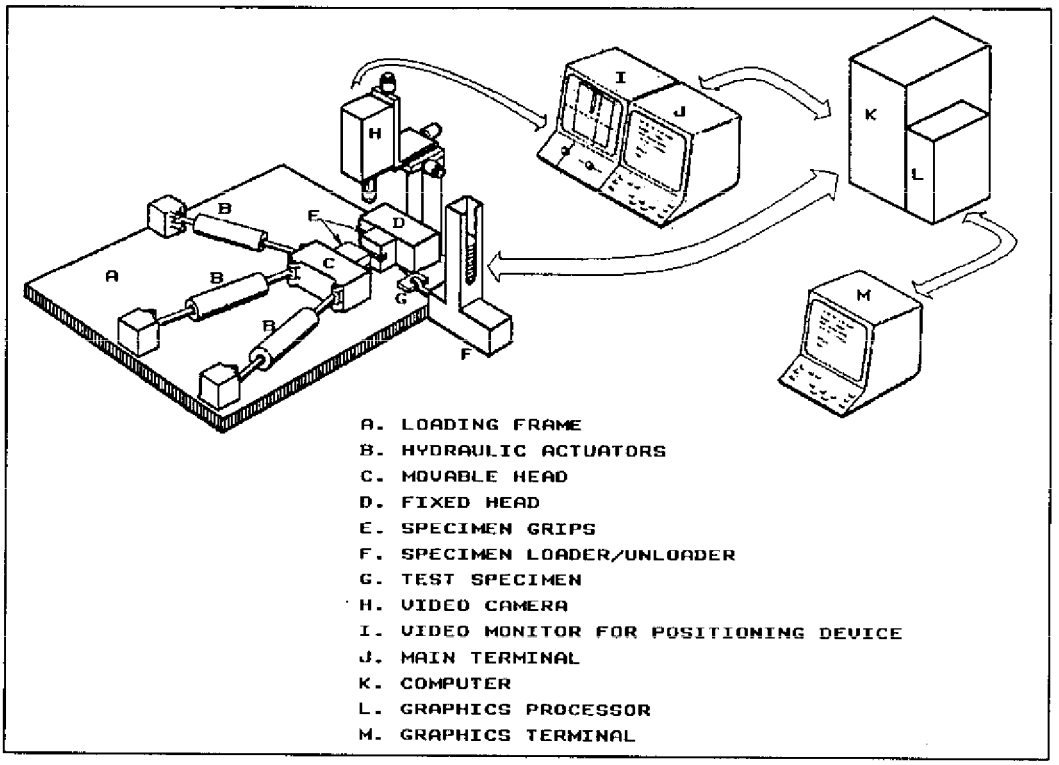

Fig. B1 — Schematic representation of the In-Plane Loader System

B.1 System Components

B.1.1 The In-Plane Loader

This is a sophisticated automated testing machine capable of subjecting test specimens to arbitrary displacement-controlled in-plane loading corresponding to combinations of pulling/pushing, sliding, and rotating boundary displacements.

B.1.2 The Computer System

The computer serves as a controller by sending commands to the hydraulic actuators of the IPL through digital-to-analog converters, and by receiving gauge measurements from the IPL via the analog-to-digital converters. It is also used for real-time data collection and reduction during the tests as well as for various post-testing analyses. Among the latter are the determination of the energy dissipation function and

consequent constitutive behavior for the material and finite element analysis of specific structural components.

B.1.3 The Graphics Processor

The graphics processor is used to facilitate the pre- and post-processing requirements of the finite element analyses. Specifically, it is used in conjunction with solid modeling and rendering software to produce finite element models of the specimen itself and specific structural components. It is also used to generate rendered images showing the spatial distribution of dissipated energy.

B.2 In-plane Loader Description

Although the IPL has been described previously (Mast *et al.* (1983)), its design has since evolved sufficiently to warrant an updated description. The in-plane loader in its current incarnation is shown in Fig. B1 with a more detailed portrayal in the vicinity of the specimen grips shown in Fig. B2. Basically, it con-

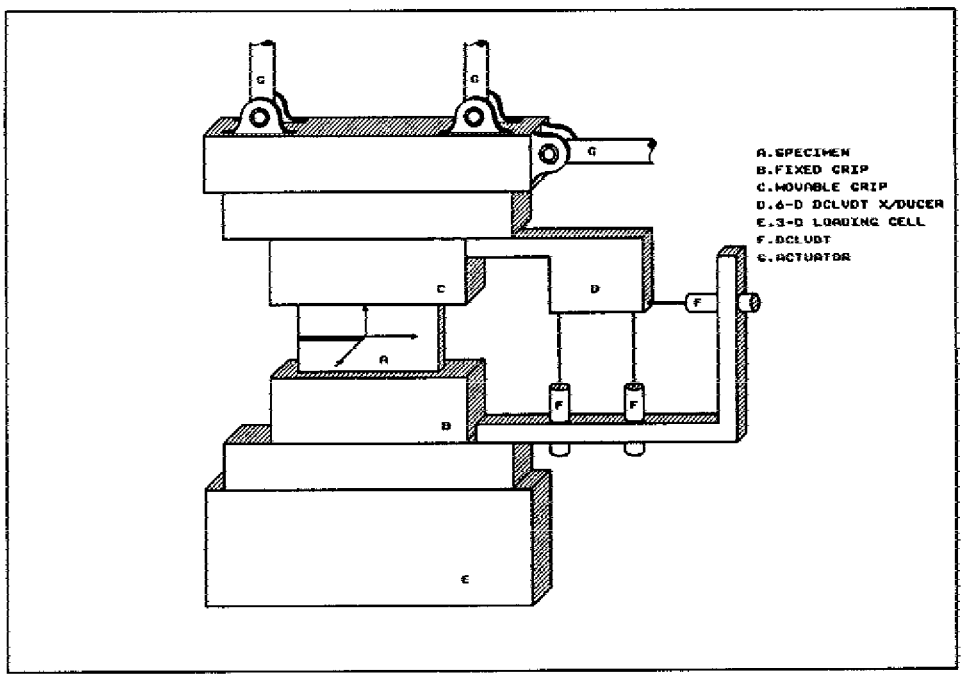

Fig. B2 — In-Plane Loader's closeup view of the grip area

sists of three independent computer controlled hydraulic actuators connected to a movable head. The loading path of each actuator can be independently prescribed, thereby producing arbitrary combinations of opening/closing, sliding, and in-plane rotating displacements.

Each actuator unit is composed of

- 2-Kip hydraulic linear actuator with a 6-in. stroke,
- DC powered linear displacement transducer (DCLVDT) which is mounted on the actuator and measures ram motion relative to the actuator cylinder,
- operational amplifier that computes the difference (the displacement error) between the actual ram displacement and the programmed one,

- electrically controlled hydraulic servo valve that receives the displacement error output of the operational amplifier and delivers controlled hydraulic power to the actuator, forcing the ram to displace the amount necessary to minimize the displacement error,
- 2-Kip strain gauge load cell mounted on the ram end, and
- instrument amplifier to amplify the millivolt output of the load cell.

Relative displacements between the two grips are monitored by a specially designed six-component DCLVDT mounted on the specimen side of the movable head. A three-component strain-gauged load cell is used to monitor the movable head reaction forces.

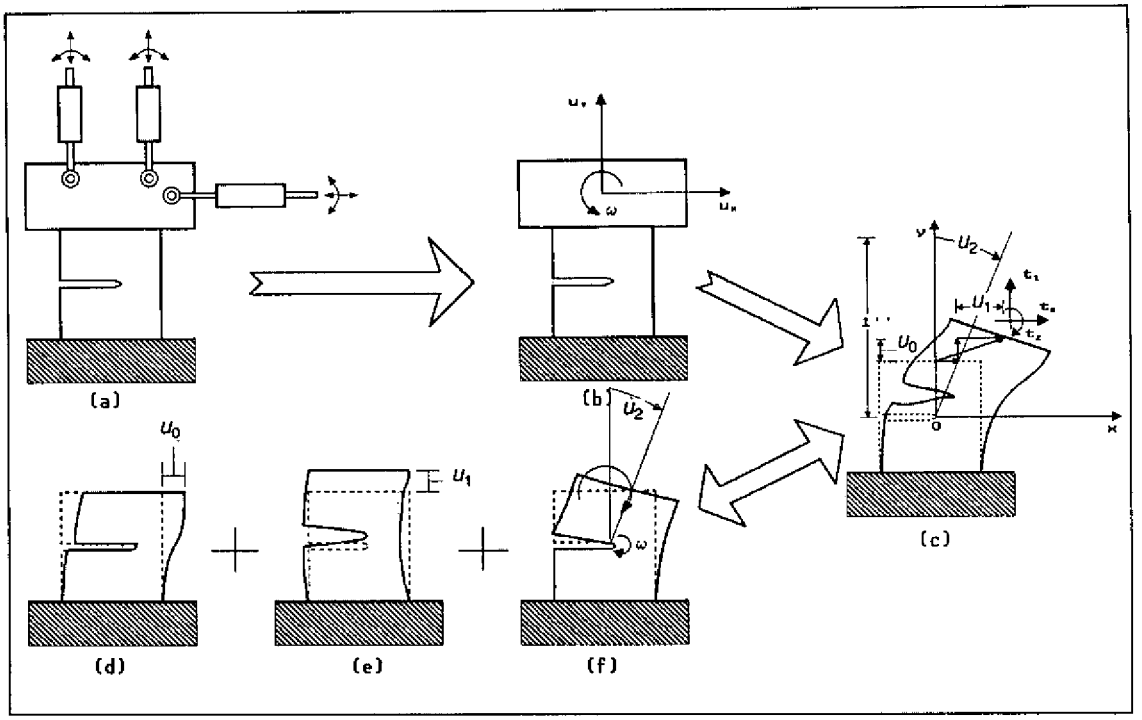

Fig. B3 — Schematic of the equivalence between the (a) actuator motions and (b) the three modes of motion , as well as (c) the process of composing an arbitrary loading combination, from linear combinations of the three basic motions: (d) shear, (e) opening/closing and (f) rotation

Two actuator configurations deserve special attention. The first is when any of the actuators is parallel with another, while the second occurs when the lines of action of the actuators intersect at a common point. Both of these configurations prevent the application of the full range of opening/closing, sliding, and rotation, and, consequently, were avoided in the design.

The hydraulic grips are computer controlled and operate like a pair of pliers whose handles are forced together by a compact servo-controlled jack built into the head. Specimens are inserted in the grips from a loading magazine via a mechanical feeding device. This ensures uniformity in the gripping conditions and allows for a rapid throughput (currently 340 specimens/hour). A hydraulic power control unit consisting of an operational amplifier, a pressure transducer, and an electrohydraulic valve, maintains a constant gripping pressure as the test proceeds. The magnitude of the gripping force is selected to be sufficient to prevent specimen slippage, and yet not so great as to cause failure at the grips.

The digital imaging system is provided to give the operator an efficient and accurate method of performing initial specimen geometry measurements and calibrations. A video camera with a long focal length,

positioned by a motor driven three-axis stage, is mounted over the specimen and provides a magnified (15x) view of the specimen on a TV monitor. Horizontal and vertical cursor lines are superimposed on the TV image and can be used to mark various features such as the initial position of the notch tip. The cursor digital output signals are continuously monitored and saved on command.

The block diagram of the entire system is shown in Fig. B4 together with a schematic representation of the information paths from and to the IPL relative to the computer controller. Twenty-one measuring

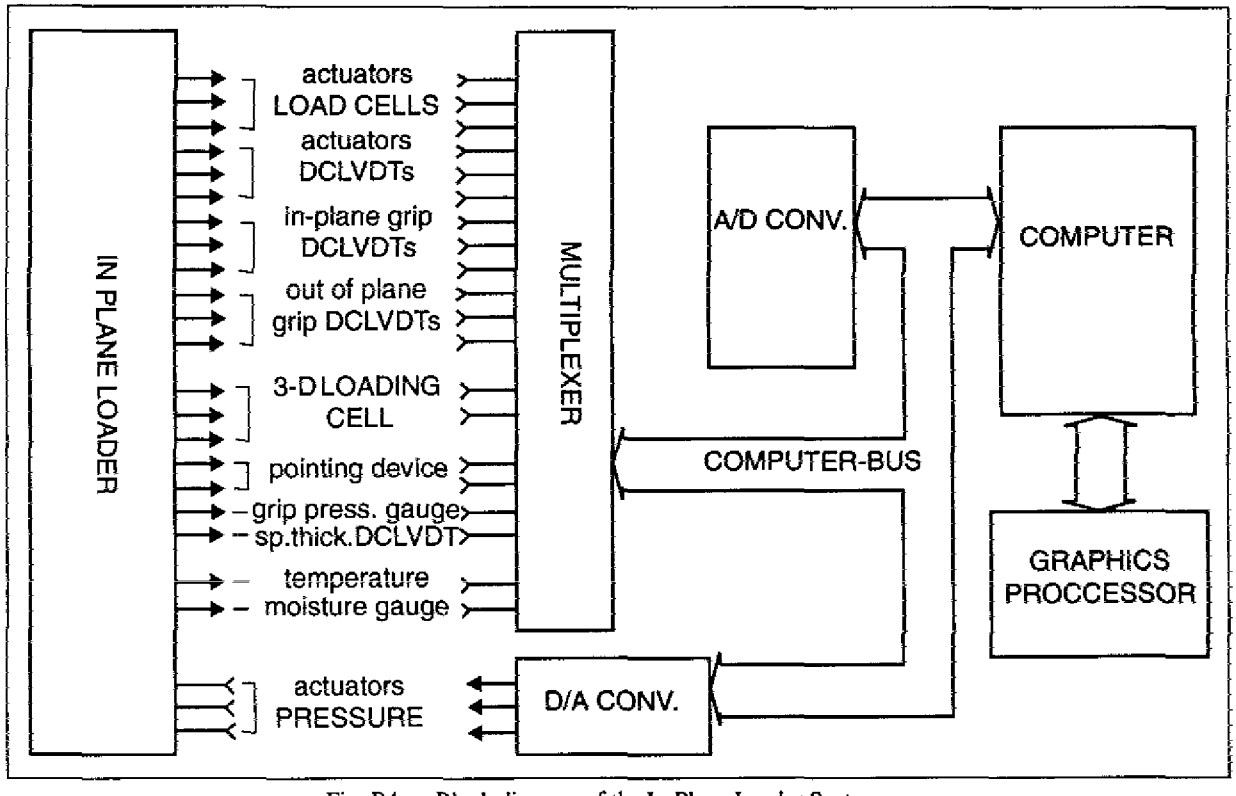

Fig. B4 — Block diagram of the In-Plane Loader System

channels are interfaced with a multiplexer connected to the analog-to-digital converter which is connected to the computer through DMA (direct memory access) via the computer bus. Similarly, the digital-to-analog converter has its output connected to the servo valves of the actuators and its input communicates with the computer via the bus in a DMA fashion.

Appendix C
A Vector Space Representation of the Optimization Scheme

A vector space geometrical representation of the optimization scheme provides for a simple explanation of the optimization procedure. Assume for the sake of simplicity (and because we can't represent entities having dimensions higher than three on paper) that the quantity $[X]\,\underset{\sim}{c}$ can be represented as a vector $\underset{\sim}{c}$ in a two-dimensional space X with $\underset{\sim}{X}_1$ and $\underset{\sim}{X}_2$ being the corresponding basis vectors as shown in Fig. C1. The columns of the array $[X]$ contain the components of the basis vectors $\underset{\sim}{X}_1$ and $\underset{\sim}{X}_2$ in terms of a higher dimensional space D, the higher dimensions of which are denoted by the axis N normal to the space X.

Assume now that another vector $\underset{\sim}{d}$ lies in the higher dimensional space D of which the space X is a subspace as shown in Fig. 15. The difference of these two vectors then lies in this higher dimensional space and is another vector denoted as $\underset{\sim}{e}$ which expresses the error between the two vectors, so that

$$\underset{\sim}{e} = \underset{\sim}{d} - \underset{\sim}{c}\,. \tag{C1}$$

This can be rewritten in the matrix form

$$[X]\,\underset{\sim}{c} + \underset{\sim}{e} = \underset{\sim}{d}\,. \tag{C2}$$

The objective of the process is to determine a vector $\underset{\sim}{c}_0$ such as the magnitude (or norm) of the vector $\underset{\sim}{e}$ takes its minimum value $\underset{\sim}{e}_0$ according to

$$\min \|\underset{\sim}{e}\| = \underset{\sim}{e}_0. \tag{C3}$$

In the case of the usual Euclidean norm, i.e., the square root of the sum of the squares of the components, $\underset{\sim}{c}_0$ turns out to be the projection of the vector $\underset{\sim}{d}$ of space D onto the space X, and therefore $\underset{\sim}{e}_0$ is normal to this space.

Fig. C1(b) deals with the effects of inequality constraints case. Suppose $\underset{\sim}{M}_1$, $\underset{\sim}{M}_2$ are the vectors corresponding to the matrices $\underset{\sim}{M}_1^T$ and $\underset{\sim}{M}_2^T$, which also lie in the space X. Then, the inequality constraint of the form

$$[M]\,\underset{\sim}{c} \geq 0 \tag{C4}$$

specifies that the only acceptable solutions for $\underset{\sim}{c}$ must lie in the region of X (shaded region) defined by the interior of the two lines which also lie in X and are normal to the vectors $\underset{\sim}{M}_1$, $\underset{\sim}{M}_2$ respectively.

However, as can be seen in Fig. C1(c), the vector $\underset{\sim}{c}_0$, which exactly satisfies Eq. (22) and minimizes $\underset{\sim}{e}$ to a value $\underset{\sim}{e}_0$, may lie outside the region specified by the constraints. In this case the quadratic programming methodology determines a vector $\underset{\sim}{c}'_0$, which satisfies the constraints by being the projection of $\underset{\sim}{c}_0$ onto the closest boundary of the shaded region. The magnitudes of the components of $\underset{\sim}{c}'_0$ in the space X will then be the desired coefficients c_i. Finally, this process is valid when the spaces X and D have arbitrary dimensions so long as $Dim\,(X) \leq Dim\,(D)$ and so obviously applies in our case.

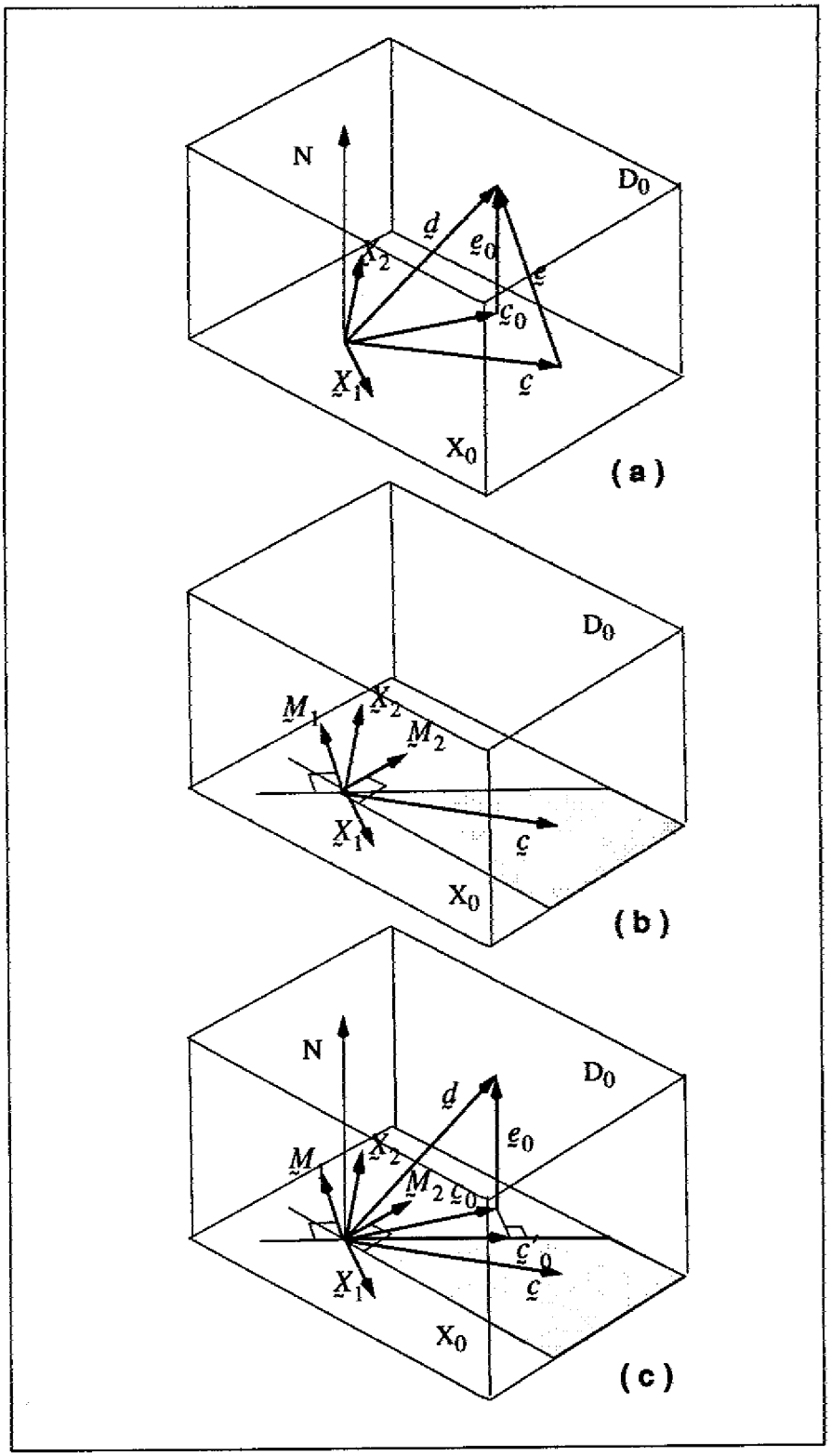

Fig. C1 — Geometrical representation of the optimization procedure describing (a) the solution for Eq. (C2), (b) for the constraints , and (c) for both equation and constraints